Objective Assessment of Image Quality: Extension of Numerical Observer Models to Multidimensional Medical Imaging Studies

Auranuch Lorsakul

Submitted in partial fulfillment of the
requirements for the degree of
Doctor of Philosophy
in the Graduate School of Arts and Sciences

COLUMBIA UNIVERSITY

2015

ABSTRACT

Objective Assessment of Image Quality: Extension of Numerical Observer Models to Multidimensional Medical Imaging Studies

Auranuch Lorsakul

Encompassing with fields on engineering and medical image quality, this dissertation proposes a novel framework for diagnostic performance evaluation based on objective image-quality assessment, an important step in the development of new imaging devices, acquisitions, or image-processing techniques being used for clinicians and researchers. The objective of this dissertation is to develop computational modeling tools that allow comprehensive evaluation of task-based assessment including clinical interpretation of images regardless of image dimensionality.

Because of advances in the development of medical imaging devices, several techniques have improved image quality where the format domain of the outcome images becomes multidimensional (e.g., 3D+time or 4D). To evaluate the performance of new imaging devices or to optimize various design parameters and algorithms, the quality measurement should be performed using an appropriate image-quality figure-of-merit (FOM). Classical FOM such as bias and variance, or mean-square error, have been broadly used in the past. Unfortunately, they

do not reflect the fact that the average performance of the principal agent in medical decision-making is frequently a human observer, nor are they aware of the specific diagnostic task.

The standard goal for image quality assessment is a task-based approach in which one evaluates human observer performance of a specified diagnostic task (e.g. detection of the presence of lesions). However, having a human observer performs the tasks is costly and time-consuming. To facilitate practical task-based assessment of image quality, a numerical observer is required as a surrogate for human observers. Previously, numerical observers for the detection task have been studied both in research and industry; however, little research effort has been devoted toward development of one utilized for multidimensional imaging studies (e.g., 4D). Limiting the numerical observer tools that accommodate all information embedded in a series of images, the performance assessment of a particular new technique that generates multidimensional data is complex and limited. Consequently, key questions remain unanswered about how much the image quality improved using these new multidimensional images on a specific clinical task.

To address this gap, this dissertation proposes a new numerical-observer methodology to assess the improvement achieved from newly developed imaging technologies. This numerical observer approach can be generalized to exploit pertinent statistical information in multidimensional images and accurately predict the performance of a human observer over the complexity of the image domains. Part I of this dissertation aims to develop a numerical observer that accommodates multidimensional images to process correlated signal components and

appropriately incorporate them into an absolute FOM. Part II of this dissertation aims to apply the model developed in Part I to selected clinical applications with multidimensional images including: 1) respiratory-gated positron emission tomography (PET) in lung cancer (3D+*t*), 2) kinetic parametric PET in head-and-neck cancer (3D+*k*), and 3) spectral computed tomography (CT) in atherosclerotic plaque (3D+*e*).

The author compares the task-based performance of the proposed approach to that of conventional methods, evaluated based on a broadly-used signal-known-exactly /background-known-exactly paradigm, which is in the context of the specified properties of a target object (e.g., a lesion) on highly realistic and clinical backgrounds. A realistic target object is generated with specific properties and applied to a set of images to create pathological scenarios for the performance evaluation, e.g., lesions in the lungs or plaques in the artery. The regions of interest (ROIs) of the target objects are formed over an ensemble of data measurements under identical conditions and evaluated for the inclusion of useful information from different complex domains (i.e., 3D+*t*, 3D+*k*, 3D+*e*). This work provides an image-quality assessment metric with no dimensional limitation that could help substantially improve assessment of performance achieved from new developments in imaging that make use of high dimensional data.

Table of Contents

List of Tables

List of Figures

Glossary

AUC	Area under the receiver operating characteristic curve
BKE	Background-known-exactly
CHO	Channelized Hotelling observer
CNR	Contrast-to-noise ratio
CT	Computed tomography
DECT	Dual-energy CT
DOG	Difference-of-Gaussian
EM	Expectation maximization
FBP	Filtered backprojection
^{18}F-FDG	^{18}F-fluorodeoxyglucose
^{18}F-FLT	3'-deoxy-3'-^{18}F-fluorothymidine
FOM	Figure-of-merit
FORE	Fourier rebinning
FOV	Field of view
FWHM	Full width at half maximum
GATE	Geant4 Application for Tomographic Emission

HO	Hotelling observer
HU	Hounsfield unit
LG	Laguerre Gaussian
MECT	Multi-energy CT
MR	Magnetic resonance
MRS	Magnetic resonance spectroscopy
MTF	Modulation transfer function
OSEM	Ordered subset expectation maximization
PET	Positron emission tomography
PDF	Probability density function
PSF	Point spread function
ROC	Receiver operating characteristic
ROI	Region-of-interest
SKE	Signal-known-exactly
SKS	Signal-known-statistically
SNR	Signal-to-noise ratio
SPECT	Single photon emission computerized tomography
SUV	Standardized uptake value
TAC	Time activity curve
XCAT	Extended cardiac torso

Acknowledgments

With full gratitude I would like to acknowledge the following individuals who supported, assisted, inspired, encouraged, and sacrificed themselves to help my pursuit of a Ph.D. degree. The work on this dissertation has given me great pleasure and considerable experience throughout these years.

I am greatly indebted to my academic advisor, Professor Andrew F. Laine for his extensive support and valuable guidance throughout my doctoral studies at Columbia University. He gave me the opportunity to pursue my doctoral studies in the Department of Biomedical Engineering. Dr. Laine encouraged me to explore different areas within the wide field of medical imaging. I have to deeply thank him for always being supportive and generous no matter what kind of problems I approached him with.

I would like to express my deepest gratitude to my thesis advisor, Professor Georges El Fakhri for his expert advice and encouragement throughout this dissertation. He gave me the opportunity to work with his group for conducting this dissertation at the Center for Advanced Medical Imaging Sciences, Massachusetts General Hospital, Harvard Medical School. Dr. El Fakhri introduced me the fascinating field of nuclear medicine imaging and thanks to his energy and enthusiasm, I gained tremendous knowledge while conducting excellent research. I am

extremely thankful and indebted to him for sharing expertise, providing constructive advice, giving valuable guidance, and for the encouragement that he extended to me.

My deeply sincere gratitude goes to my thesis co-advisor, Professor Quanzheng Li for his guidance and insightful advice on the projects. He encouraged me to explore different technical approaches. Dr. Li has been a source of great research ideas and encouragement that have contributed much in the course of my doctoral work. I am truly grateful and appreciative all of his kindness, patience, support, and understanding.

I would like to thank Professors Elizabeth M.C. Hillman, Helen H. Lu, and X. Edward Guo for serving on my proposal and defense committee. I am so delighted for their suggestions, constructive comments, and inspiring discussions. I especially wish to thank to Professor Van C. Mow, the founder and inaugural Chairman of the Department of Biomedical Engineering, Columbia University, for his support and encouragement.

Thanks to all current members and alumni of the Center for Advanced Medical Imaging Sciences at Massachusetts General Hospital and of the Heffner Biomedical Imaging Laboratory at Columbia University. Special thanks to Drs. Jinsong Ouyang, William Worstell, Arkadiusz Sitek, Nathaniel M. Alpert, Marc D. Normandin, Yothin Rakvongthai, Yoann Petibon, Ning Guo, Ruoh-Fan Yen, and Kira Grogg for their contributions, scientific discussions, and constructive comments.

My doctoral studies and this dissertation would not have been possible without funding from the Department of Biomedical Engineering, the Heffner Biomedical Imaging Laboratory at Columbia University, and the Center for Advanced Medical Imaging Sciences at Massachusetts General Hospital.

Last but not least, I would like to express great appreciation to my parents for their unconditional love, encouragement, and endless support, and to my sisters and brother for their steadfast understanding and encouragement. Without their support, I could not accomplish my Ph.D. journey in the best possible way.

To my family for their love and support.

Chapter 1

Introduction

1.1 Motivation

When a new image-acquisition or image-processing technique is being developed, a critical question is how well the technique improves image quality [2]. In a conventional meaning, image quality measures of how accurately an image of a subject represents that target subject. In the context of radiology, the image quality is the measure of the usefulness of an image in determining a meaningful and accurate diagnosis [3]. The purpose of an imaging system and of a radiologist is the detection and accurate depiction of subtle abnormalities that demonstrate pathology, even though the object can be seen on low-quality image. With these diagnostic challenges, maintaining the highest image fidelity is crucial to radiologists. Technologists and radiologists usually encounter tasks related to the diagnostic utility of an image in order to compare image quality obtained in different improved imaging systems or imaging methods. Therefore, understanding the features that comprise image quality is necessary to recognize problems and articulate their causes.

To evaluate the ability of an image to reveal a certain pathology, subjective measures of *diagnostic performance* are often used. This type of analysis requires a trained person to view an image and determine whether he or she actually observes an abnormality in the image, with a confidence level rating, for a large set of images. Radiologists often participate in studies involving radiologic diagnosis using receiver operating characteristic (ROC) studies. ROC studies provide a direct measure of the performance capabilities of the imaging system or technique being evaluated through the plot of false-positive rate vs. true-positive rate (or 1-specificity vs. sensitivity) [3]. In evaluating imaging studies, ROC analysis is particularly valuable for comparing different procedures, imaging methods, techniques, or imaging systems, etc.

To perform an ROC analysis of an imaging system, a set of images that demonstrates both normal and abnormal pathology must be acquired, where a test object (e.g., a lesion) should be selected for being marginally visualized. The fully obvious or gently dedicated test objects are not useful. A series of images is acquired, for example, with system A and system B. It is essential to specify whether the "pathology" was actually present in each image. Thus, the "truth" of the presence or absence of the test object in an image is known and recorded. Presented with each image sequentially, a participant in the study is requested to rank his or her confidence, within a certain range of scales, in whether the investigated objects were present. Each of these different levels of certainty depicts a different *decision threshold*, which can be used for determining the tradeoff between *sensitivity* and *specificity* of the testing system [3].

Decision thresholds are routinely used by the radiologist or nuclear medicine physician; however, they are often selected carelessly in the clinical interpretation of images. For instance, in lung cancer, over 50% of the radiographically indeterminate nodules resected at thoracoscopy

examined by a radiologist are benign [4], thus the radiologist may aim to adjust his or her decision threshold to reduce the number of biopsies. Nevertheless, one should not adjust the decision threshold too substantially in the other direction, because this would result in missing actual cancers (reducing in sensitivity), with potentially more serious consequences for the patient. Moreover, there may be other factors influencing the decision threshold, such as, the age of the patient (e.g., one third of lung nodules in patients more than 35 years old are found to be malignant [4]), familial history, and other symptoms.

Better understanding of the detection strategies used by human observers can determine favorable predictors of human detection performance; however, having a human observer perform the tasks for imaging system evaluation is costly and time-consuming. A human observer is the standard goal for image quality assessment as human observers are ultimate receivers of visual cognition and description. There is a fair amount of subjective human judgment involved in the performance evaluation of medically relevant tasks. Frequently, the human-performance task assessment of a particular scanner or scanning protocol requires tremendous amounts of data and the assistance of several radiologists. In particular, it is necessary to perform system optimization over numerous sets of parameters of interest. Thus, such an optimization process requires multiple lengthy and expensive human-observer performance studies [3, 5, 6].

Computer (numerical) observers can be surrogates for human observers used to assess the improvement obtained from newly developed techniques. Mathematical numerical observers that imitate the human visual system for clinically realistic tasks allow expediting such studies, reducing the time and cost of human-observer studies. A numerical observer is an algorithm based on statistical decision theory used to characterize the image quality. The algorithm accepts

a multivariate input (e.g., the image) and returns a scalar value (e.g., the test statistic). By largely determining the detection task difficulty for human observers, this algorithm is defined by the statistical properties of the image, characteristics of the target object (e.g., lesion), anatomical background, and system noise [7].

As predictors of human performance, current research on numerical observers involves linear observers, which incorporate linear functions of the image pixels. The observer that has full knowledge of the statistical information of the image data is known as the Bayesian ideal observer. Determined by statistical decision theory, the ideal observer was introduced as the optimal decision maker for classification tasks. However, it is often difficult and impractical to evaluate performance using the ideal observer. This is because of the extensive complexity of the image statistics that are typically unknown and poorly estimated for real clinical datasets [7-9].

The practical alternative to the ideal observer is known as the Hotelling observer. The Hotelling observer (HO) is a well-known numerical observer that uses estimation of image statistics to quantify the observer performance, thereby predicting human performance [10-13]. The HO constrained to a number of channels (linear filters) is called the channelized-Hotelling observer (CHO) [14]. The channels are a series of filters that properly extract efficient features and preserve maximal information in the data using spatial-frequency-selective or orientation-selective mechanisms [15]. HO and CHO are usually selected as a common metric for objective evaluation and comparison of medical imaging systems such as positron emission tomography (PET), single-photon emission computerized tomography (SPECT), computed tomography (CT), and PET/CT [7, 10, 13, 16-20]. HO and CHO serve a metric of image quality that has the same predictive capabilities of human ROC studies for fast, objective evaluation and optimization of image acquisition systems and image processing methods [2].

1.2 Challenges and Unmet Needs

Currently, the clinical practice is moving toward the use of spatiotemporal or multidimensional data. Several types of clinical modalities have been improved due to new imaging acquisitions or imaging methods. Nevertheless, numerical observers for task-based (objective) assessment are limited to only two or three-dimensional (2D or 3D) analysis. Hence, there is inadequate evaluation or underestimation of task-based performance for image assessment when executing on multidimensional clinical data, especially their dimensionality is greater than three.

There are three important clinical applications, outlined below, that are substantially improved by taking advantage of specific multidimensional techniques; however, there has been limited evaluation in the context of objective image assessment:

1. Respiratory-gated PET: This technique improves the image quality through the use of respiratory gating protocol. Respiratory gating is employed to reduce respiratory motion artifacts when acquiring data using an integrated system of PET/CT or PET/MR. Respiratory motion artifacts relate to that PET acquisitions are taken over several minutes (6-9 min) during tidal breathing and represent an average diaphragm position. In contrast, CT scans can be acquired within seconds (~15 sec) and MR imaging examination typically takes much longer than a CT exam. As a result, patient motion can cause severe artifacts in both PET/CT and PET/MR. Furthermore, the different time resolutions of the two modalities (e.g., PET and CT, or PET and MR) generate misregistration problems between the PET and CT or MR imaging.

With multiple shorter time-frame acquisitions (gates), the resultant images are formed in four dimensions (3D+*t*). Hence, the accuracy in the diagnosis of lesions in the thorax and the image quality have been improved, such as reducing the blurring of the lesion that causes

underestimation of the corresponding standardized uptake value (SUV) and overestimation of the lesion volume. However, there are limited studies quantifying gains in image quality and lesion detection performance with a numerical observer that takes into account all gated information in four dimensions. The performance of respiratory-gated PET is commonly assessed using 2D or 3D numerical observers applied on motion-corrected images formed by image-based [21] (post-reconstruction) or reconstruction-based motion correction techniques [22, 23]. Nevertheless, inaccurate motion correction may compromise the lesion detectability. Only limited success has been achieved for objectively evaluating the improvement expected in lesion detection performance when using respiratory-gated PET data compared with non-gated and motion-corrected data.

In this work, the author presents a new numerical observer (3D+*t*) and rigorous objective evaluation of the improvement obtained from respiratory-gated PET applied directly on all gated frames instead of conventional non-gated and motion-corrected images. In the other hand, the proposed framework can avoid the effect of additional inaccuracy introduced during the post processing to obtain motion-corrected results.

2. Kinetic Parametric PET: This analytical method improves the ability to quantify several biomedical functions, such as blood flow, glucose metabolic rate, cerebral oxygen utilization, and neuroreceptor ligand binding [24]. Specifically, it improves tumor detection in the early stage of cancer. With the principle of the kinetic model analysis, it is used to analyze dynamic PET images to accurately estimate changes of tumor metabolic rates. This quantitative measurement provides better tumor characterization, which is most useful for treatment response monitoring, as compared to conventional PET images.

Kinetic models for PET typically aim to isolate PET signals, which are commonly a composite of various superimposed signals. The output kinetic parameters from kinetic models (e.g., the parametric image volumes of K_1, k_2, and k_3) formed in 3D+k are reflective of inherent kinetic properties of the particular tracer molecule in the body system, e.g., binding, delivery, or any hypothesized processes [25].

In the field of parametric imaging, there are very few studies in objective image assessment with computer observers. One of the major reasons is the complexity of the parametric dimensional domain. In literature, little research effort has demonstrated the development of numerical observers for parametric images [26, 27]. Chen *et al*. [26] depicted a theoretical assessment approach of spatial-temporal parametric PET images based on detection tasks. They reported that the figure-of-merit (FOM) using computer observers on a single static image was theoretically inferior to that on parametric images obtained by Patlak (simplified kinetic parametric) analysis. Wang *et al*. [27] used numerical observers to investigate the performance of different approaches to the utilization of temporal information, including kinetic parameters and dynamic PET images. They simulated 1D Monte Carlo data and compared lesion detectability. The comparison results were questionable because the analysis was not based on full 4D PET datasets. Through these reports, it remained very limited studies to assess the superior performance of parametric imaging.

In this study, the author proposes a new 4D numerical observer (3D+k) and a framework for image quality assessment indicating improvement obtained from parametric imaging. The proposed approach could be performed to evaluate and compare the lesion detection performance of different approaches i.e., static, dynamic, graphical Patlak, and parametric imaging.

3. Spectral CT: This spectral CT approach improves material differentiation in tissues over conventional CT. Conventional CT often uses for anatomical imaging but limits for soft tissue differentiation. This is because conventional CT measures the cumulative attenuation over the entire energy range of energies within a voxel for all tissues, not the response at different, specific energy levels. The concept of energy selective data acquisition and analysis has been proposed as spectral CT. There are different technical approaches developed for spectral CT, such as dual-energy CT (DECT) and multi-energy CT (MECT), which are progressing to provide the functional information beyond CT imaging of morphology. Currently, several clinical applications have been explored for dual-energy CT imaging, whereas multi-energy CT presently broadens at preclinical phases on spectral imaging.

Objective image assessment of the performance improvement obtained using spectral CT is mainly limited to investigation of particular clinical tasks. Several studies have shown that material decomposition with spectral CT imaging provides better differentiation of materials for atherosclerotic plaque features [28-33]. Nonetheless, there are limited studies using quantitative metrics for evaluating performance in terms of objective image assessment exploiting a numerical observer in spectral CT imaging [34].

The major problems may be because it is difficult to correlate the data from different energy windows of spectral CT images, especially given the complexity of the spectral CT data, since spectral CT imaging can be considered a four-dimensional (3D+*e*) technique to form images from measurements in three spatial dimensions and a unique energy dimension [35]. Occasionally, evaluation of DECT is performed on energy-subtracted images (i.e., the difference between low- and high-energy images). However, in the available scientific literature, the subtracted images resulted in inferior image quality owing to signal loss (reduced photon counts)

and increased image noise (variance) [36-38]. In diagnostic evaluation, subtraction causes difficulty in the quantitative and qualitative analyses of plaque images. This is because the possible erroneous subtraction of small, focal calcifications may partly affect diagnostic accuracy. For these reasons, it is suboptimal to evaluate the observer performance based on subtracted images of DECT. Since the inclusion of useful information from all energy bins of spectral CT is crucial in characterizing the plaque components, a numerical observer that incorporates contributions from all this information is essential for fully objective assessment of spectral CT images, and it is investigated in this work.

1.3 Contributions of the Thesis

The goal of this research is to develop a rigorous evaluation methodology of an objective image assessment for multidimensional imaging to assess the improvement of image quality with more advanced imaging techniques in significant clinical applications. The novel contributions of this dissertation are:

1. **Development of a novel numerical observer that accommodates multidimensional imaging;** several key improvements differentiated this model from other previous work are:
    a. Development of channel functions of a novel numerical observer (3D+*t* or 3D+*k* or 3D+*e*) that extracts features pertinent to detection/classification and reduces computational cost.
    b. Development of a novel numerical observer constructed with the channels mentioned above to estimate signal-to-noise ratio (SNR) for detection or classification tasks in multidimensional data.

2. **Validation of the novel numerical observer (3D+*t*) in assessing image quality of the improvement of respiratory-gated PET imaging on lesion detection tasks;** several key features differentiated from existing methods are:
    a. Validation of the novel observer framework on preclinical simulated data with various conditions of the observer parameters, target lesions, and image noise.
    b. Validation of a lesion-detection framework with realistic artificial lesions added into a set of clinical data in a certain population of patients.
    c. Performance comparison in lesion detection using respiratory-gated, motion-corrected, and conventional non-gated methods.

    The work in Aim 1 and 2 resulted in the following publications:

    Lorsakul A, **Li Q, Trott CM, Hoog C, Petibon Y, Ouyang J, Laine AF, El Fakhri G**. 4D Numerical Observers for Lesion Detection in Respiratory-Gated PET. Med Phys. 2014 Oct;41(10):102504.

    Lorsakul A, Li Q, Mawlawi OR, Lopez BP, Laine AF, El Fakhri G. The Assessment of Lesion Detection on Respiratory-Gated Clinical PET/CT using 4D Numerical Observer. J Nucl Med. 2015; (Supplement 1):371.

    Lorsakul A, **Li Q, Hoog C, Petibon Y, El Fakhri G.** 4D Mathematical model observer for lesion detection on respiratory-gated PET imaging. J Nucl Med. 2013; 54 (Supplement 2):538.

    Dutta J, El Fakhri G, Shao X, Lorsakul A, Guo N, Li Q. Feasibility of respiratory motion compensated reconstruction using 4D PET-derived deformation fields. J Nucl Med. 2014; 55 (Supplement 1):2106.

Dutta J, Chelala M, Shao X, Lorsakul A, Li Q, El Fakhri G. Accuracy of Respiratory Motion Compensated Image Reconstruction Using 4DPET-Derived Deformation Fields. Conf Proc IEEE Med Imag. 2014 Nov 8; 2014.

3. **Validation of the novel numerical observer (3D+*k*) in assessing image quality of the improvement of kinetic parametric clinical PET imaging on lesion detection tasks;** several key features differentiated from existing methods are:
    a. Validation of the novel numerical observer and a lesion-detection framework to assess lesion detection performance on kinetic parametric clinical PET images instead of conventional activity images.
    b. Performance comparison in lesion detection using kinetic parametric images, Patlak graphical analysis (simplified kinetic parametric), dynamic, and conventional static images.

    The work in Aim 1 and 3 resulted in the following publications:

    Lorsakul A, El Fakhri G, Guo N, Yen R, Normandin MD, Alpert NM, Laine AF, Li Q. A Numerical Observer for Task-Based Assessment on Kinetic Parametric Imaging. J Nucl Med. 2014; (Supplement 2):48. *Young Investigator Award*, Honorable mention in the Computer and Instrumentation Council Symposium, Annual meeting of the Society of Nuclear Medicine and Molecular Imaging Annual Meeting, St. Louis, MO, USA.

4. **Validation of the novel numerical observer (3D+*e*) in assessing material discrimination of the improvement of spectral CT imaging in the atherosclerotic plaque application;** several key features differentiate from existing methods are:
    a. Validation of the novel numerical observer and a material classification framework to assess plaque discrimination performance on spectral CT images.

b. Performance comparison in plaque classification based on multi-energy CT, dual-energy CT, and conventional CT images.

The work in Aim 1 and 4 resulted in the following publications:

Lorsakul A, El Fakhri G, Ouyang J, Worstell W, Rakvongthai Y, Laine AF, Li Q. Novel Numerical Observer for Atherosclerotic Plaque Classification in Spectral CT. Med Phys. 2015 (under review).

Lorsakul A, El Fakhri G, Ouyang J, Worstell W, Rakvongthai Y, Laine AF, Li Q. Numerical Observer for Objective Assessment on Carotid Plaque Using Spectral CT. Conf Proc IEEE Med Imag. 2014 Nov 8; 2014.

Rakvongthai Y, Worstell W, El Fakhri G, Bian J, Lorsakul A, Ouyang J. Spectral CT Using Multiple Balanced K-Edge Filters. IEEE Trans Med Imaging. 2015;34(3):740-747.

Hadjipanteli A, Worstell W, Rakvongthai Y, Ouyang J, Bian J, Lorsakul A, El Fakhri G. Contrast-to-noise Estimation and Optimization of a Novel Multi-Energy CT System for a Clinical Dual-Energy Imaging Task. Conf Proc IEEE Med Imag. 2014 Nov 8; 2014.

1.4 Thesis Organization

The structure of this thesis is as follows:

Chapter 1 introduces to the motivation, challenges and unmet needs, contributions, and the scope of the thesis.

Chapter 2 provides reviews of objective image assessment including human observer, existing numerical observer models, assessment of a binary task. Consequently, it describes the clinical applications involved in the research studies. Methods used to improve the image quality of these clinical applications, resulting multidimensional images, is further explained.

Chapter 3 describes the design and development of the novel numerical-observer framework for assessing image quality in multidimensional imaging.

Chapter 4 describes the application of the proposed numerical observer to respiratory-gated PET imaging. The aim of this study was to present a novel numerical observer framework and to carefully validate it on simulated data where the ground truth is known and where the parameters (e.g., lesion uptake, lesion sizes, lesion contrasts, lesion positions, amplitude of respiratory motion) can be easily changed to study the impacts of their variation on the detection performance.

Chapter 5 describes the application of the proposed numerical observer to clinical data acquired with the respiratory-gated PET/CT method. The validation was performed on the disease-patient data with realistic inserted specified lesions. The lesion-detection assessment was compared among the improved and standard methods (i.e., gated, motion-corrected, and non-gated methods).

Chapter 6 describes the application of the proposed numerical observer to kinetic parametric PET imaging. This work demonstrates the benefit of the proposed observer, which is not limited only to spatio-temporal (3D+*time*) images, but it can be extended to different imaging domains (i.e., 3D+*k*). The validation of lesion-detection performance is demonstrated and compared among different analysis methods (i.e., kinetic parametric, Patlak, dynamic, and static imaging).

Chapter 7 describes the application of the proposed numerical observer to spectral CT imaging. Spectral CT is being developed for several clinical applications, especially atherosclerotic plaque differentiation. This work demonstrated the benefit of the proposed observer in the complex imaging domain in different energy levels (3D+*e*). The validation is demonstrated in the application of carotid-plaque classification using realistic simulated data. The comparison of

discrimination performance of different plaque types is shown among different CT methods (i.e., conventional CT, dual-energy CT, and multi-energy CT imaging).

Chapter 8 concludes the research studies and the future research directions manifested in this dissertation.

Figure 1 illustrates the summary of the dissertation organization. The dissertation focuses on objective assessment of multidimensional imaging methods. The improved imaging methods focused on are respiratory-gated PET, kinetic parametric PET, and spectral CT, which rely on oncologic (i.e., lung cancer, head-and-neck cancer) and atherosclerotic plaque applications.

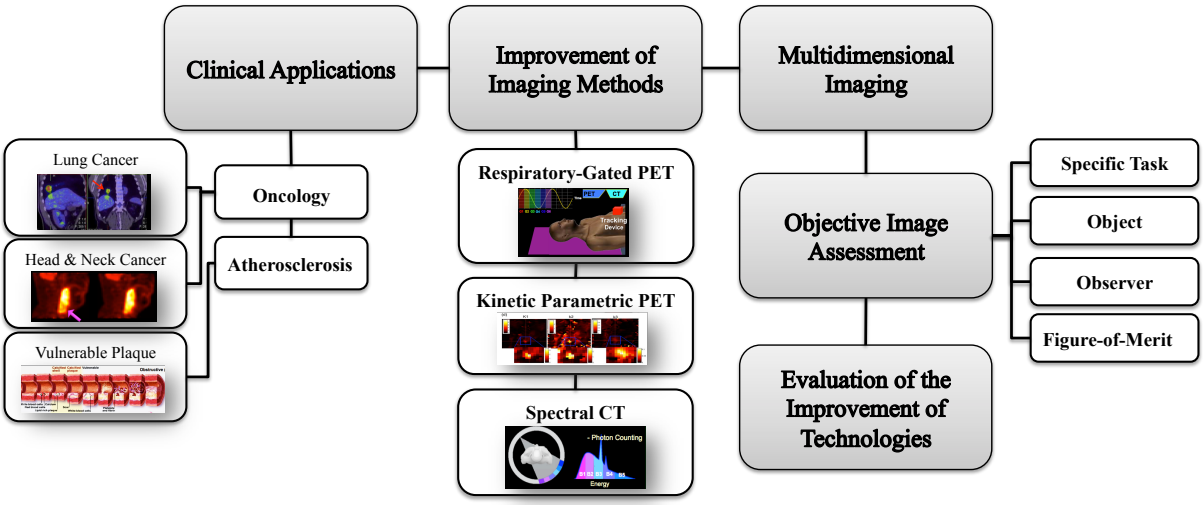

Figure 1 The diagram of the summary of the dissertation.

Chapter 2

Objective Image Assessment and Clinical Significance to Improved Multidimensional Imaging Methods

This chapter describes background, rationale, and significance for the research studies. The first section explains the concept of objective image assessment. Next, it depicts the clinical applications studied for multidimensional images. Then, the description of the improvement technology to current imaging methods will follow.

2.1 Overview

Currently, objective image assessment is acceptable to quantify the usefulness of the images and compare image quality obtained using different imaging systems or methods. Objective image assessment can be performed based on human observer or alternative mathematical numerical observers, surrogate of human observer. The well-known statistical models (i.e., Hotelling and Channelized Hotelling Observers) are presently used to assess the improvement obtained from

new developed techniques. Particularly, several assessment studies are conducted based on binary detection/classification tasks, including the paradigm of signal–known–exactly/ background–known-exactly and the signal-known-statically/background-known-exactly basis.

In this dissertation, the clinical applications studied for multidimensional images involve the assessment of detection performance in oncologic PET and the assessment of plaque classification in spectral CT. The essential background, significance, and clinical challenges are illustrated (i.e., basic principle of PET, benefits of PET in oncology, improvement of oncologic PET, basic principle of spectral CT, atherosclerotic plaque, shortcomings of CT in plaque imaging).

In addition, the overview of the improvement of selected imaging methods i.e., respiratory-gated PET in lesion detection, kinetic parametric PET in lesion detection, and spectral CT in plaque classification is describes in terms of essential problems, improved techniques, and clinical challenges associated to the investigated diseases (i.e., lung cancer, head-and-neck cancer, and carotid plaque).

2.2 Section I: Objective Image Assessment

To evaluate the performance of imaging systems, it is important that image quality should be assessed in the framework of average performance of inference tasks by observers or decision-makers [8]. Such an approach has become known as *objective image assessment*. Objective image assessment is acceptable to quantify the usefulness of the images for performing a given task. Task-based measures of image quality have been accomplished to optimize imaging system and assess observer performance for decades.

Four essential elements demonstrated in the objective assessment of image quality are:

1) **Specification of a task**; the task can be considered two kinds. The first type of the task is the *detection* of an object in the presence of a background, a related task is the classification of an image into one or more alternative classes. The second type is the *estimation* of parameters describing the object or background or both.

2) **Description of the data** (e.g., object classes and imaging process); the physical and statistical properties of the set of objects to be imaged should be taken into account in the evaluation of an imaging system. For example, in a classification task, the evaluation of PET imaging systems for the task of lesion detection requires the characterization of normal tissues and lesions of the disease under each class. The object might have one or random parameters, where the background may or may not be random.

3) **Depiction of the observer**; an observer or strategy in performing the task. The observer might be a human or model (numerical) observer, which is described more details in the next section.

4) **Assessment of a figure of merit (FOM)**; FOM refers to an indicator in the context of how well the observer performs. Possible useful FOM for classification tasks are the classification signal-to-noise ratio or SNR, the area under the receiver operating characteristic (ROC) curve (AUC), partial ROC areas, sensitivity/specificity pairs, and the percent of correct decisions (PC). For estimation tasks, possible FOM include bias, variance mean-square error (MSE), and ensemble mean square error (EMSE) [8].

2.2.1 Objective Image Assessment using Human Observer

The best way to assess the image quality is potentially to directly visualize it because human eyes are the ultimate receivers in most environments [39]. Human observer (e.g., a radiologist or an experienced nuclear medicine physician) is thus the ultimate goal for image quality

assessment. Human observer performance studies usually perform on images obtained with different imaging systems or under different imaging conditions. For example, clinical lesion detection is commonly analyzed by trained radiologists with the assistance of computer-aided diagnosis (CAD). The trained radiologists usually use the ROC metric, relying on physician's measurement ratings and subjective confidence of the signal presence, to form a performance measure known as the area under the ROC curve (AUC).

To assess image quality by means of an ROC study, a set of images must be given from the different imaging systems or techniques to be tested. An image that contains either one or no lesions can be an example of the simplest approach. The former are called *positive* images and the latter are called *negative* images. The images are then indicated by an observer whether a lesion is present or absent in each image, with his or her confidence that it is actually present. The indicated indexes are calculated for each confidence level as:

True-positive fraction (TPF) = fraction of positive images that correctly identified as positive by the observer

False-positive fraction (FPF) = fraction of negative images that incorrectly identified as positive by the observer

In addition, two other necessary parameters are the *true-negative fraction* (TNF) = (1-FPF), and the *false-negative fraction* (FNF) = (1-TPF). The TPF represents the *sensitivity* and TNF the *specificity* of the investigated test or the observer.

By plotting TPF versus FPF, the ROC curve is obtained to indicate for progressively relaxed degrees of confidence. An example of the plot of ROC curve is shown in Figure 2. The ascending 45-degree diagonal dashed line represents "guessing" and the ROC curve should lie above this line to indicate the better performance of the imaging system and observer.

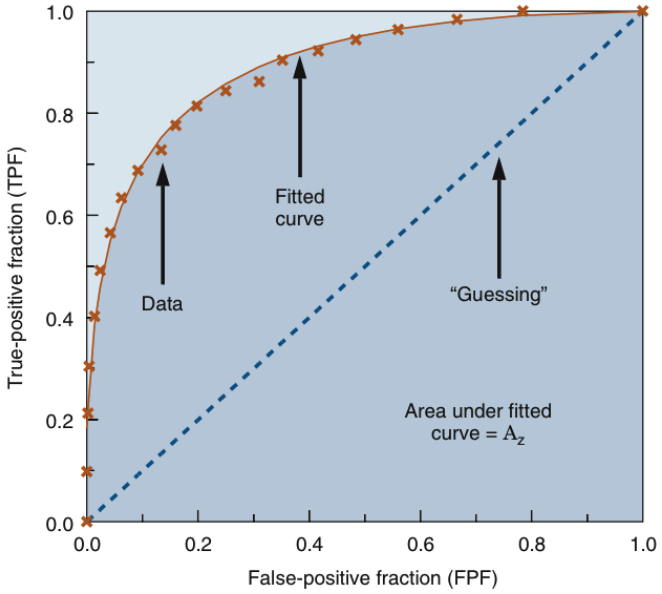

Figure 2 Example of the receiver operating characteristic (ROC) curve plot. The cross symbol (x) refers to data points; the solid line refers the fitted curve, the dash line refers to the 45-degree line, which is equivalent to "guessing." The shaded in darker blue refers to area under the ROC curve (AUC), which is one measure of detection accuracy (Cherry *et al*., 2012 [1]).

More commonly, the area under the ROC curve, usually denoted by AUC, is the parameter used to simplifying the interpretation of an ROC study. Occasionally, the interpretation of ROC results can be challenging. For example, the ROC curves for two different imaging systems can "cross," leading to ambiguity in the results. Thus, AUC can be an alternative indicator, which the number ranging from zero (all readings wrong) to 1 (all reading correct), with a value of 0.5 indicating an overall accuracy of 50% or equivalent to "pure guessing."

Although observer performance can be characterized objectively, the relationships are not well established because: 1) the observer rating takes account of the visualization of clinically relevant structures relying on the complexity of the human visual system and observer experience; and 2) frequently, the human detection performance of a particular scanner or

scanning protocol requires tremendous data and several radiologists; consequently, ROC studies are costly and time consuming. Because human observer studies require large numbers of images and complicating factors, which are very time consuming and too inconvenient, computer observer often are more practical [1].

2.2.2 Numerical Observer - Alternative to Observer Performance Studies

Modeling of human observers can be employed to predict human performance. Numerical observers are possibly used to optimize imaging system without the need for lengthy human-observer studies at every design stage. Numerical observers can mimic human observers in the clinically realistic tasks and can be processed thousands of tasks to expedite such studies. Numerical observer performance studies are alternative to use a mathematical model that under appropriate conditions for predicting the performance of a human observer and can be used as a surrogate for human observer studies. Numerical observers use the information available in images to measure the visual detection performance, attempting to predict human performance.

The ideal observer is defined as the observer that optimally utilizes all available information in an image, which requires the complete probability density function (PDF) of the data under each hypothesis. For classification tasks, the ideal observer is appropriate for the evaluation of the quality of the raw data, and can be an observer choice for the assessment of imaging hardware. Alternatively, in cases that this PDF information is infeasible to achieve or unavailable, the Hotelling observer (HO) can be substituted, which requires only the first- and second-order statistics of the data [8].

In present, numerical observers are valuable tools in objective assessment of image quality and have become common metrics of task-based evaluation in medical imaging, such as positron emission tomography (PET) [17, 18], single-photon emission computerized tomography (SPECT) [7, 40, 41], and computed tomography (CT) [42-44]. It is desirable to develop numerical observers to yield a metric of image quality that has the same predictive capabilities of ROC studies for fast objective evaluation and optimization of image acquisition systems and image processing methods [2]. One of the aims of this dissertation was to develop a numerical observer that would allow all information present in a series of images to be used for assessing image quality and detection accuracy using an objective task-based methodology. This assessment method would quantify image quality in terms of measurement on signal levels regardless human subjective.

2.2.3 Hotelling and Channelized Hotelling Observers

One of optimal-linear numerical observers is the well-known HO proposed by Barrett and colleagues [10-13]. HO requires only the first- and second-order statistics of the data to maximize the SNR, which is a common figure-of-merit measure of observer performance. Typically, HO uses a template to prewhiten (decorrelate) the noise prior to applying the matched filter in the correlated noise. For example, in PET imaging, image noise is usually correlated, thus HO is beneficial for measuring lesion detectability or SNR by compensating for all contributions to the correlations in the data [2].

The observer template sensitively associates with both the mean signal (i.e., the first-order statistics) and the image covariance (i.e., the second-order statistics). If either of these components changes, the task performance strategy can be alternated. Thus, the Hotelling

observer depends on the variation of both the signal profile and the image covariance. This is a crucial aspect because understanding the degree to which human observers are able to adapt to the statistical properties of images must be carefully considered. The Hotelling observer associates with optimal adaptation to the capability to invert the image covariance matrix, which is implied to decorrelating, or prewhitening, the noise [5].

However, one potential problem in determination of HO's SNR is the inversion of the large dimensional covariance matrix used for estimating the image statistics. The inverse covariance computation by numerical inversion can be highly time consuming. This is because of the large size of the matrix together with the possible severe numerical error if the covariance matrix is ill conditioned. The ill-conditioning problem is also caused computing inverse-covariance products slow convergence in the iterative methods [5].

To solve this problem and to mimic the human visual system, Myers and Barrett [14] proposed the inclusion of 'channels' (linear filters) to capture the efficient features of the HO template and built the CHO. Particularly, CHO uses spatial-frequency-selective and orientation-selective mechanisms to properly extract the efficient features that preserve maximal information in the data. As a result, it allows estimating the HO's SNR in a lower-dimension space. There is a substantial body of work [7, 10, 12, 13, 16] confirming that CHO correlates well with human performance in the presence of anatomical backgrounds [45] in medical imaging applications.

The channel profiles must be appropriately designed to give minimal loss of detectability and provide an estimate of the separability inherent in the data. Several different channels are designed to estimate the separability of the data including square channels [46, 47], difference-of-Gaussians (DOG) [5, 48], difference of Mesa filter [16, 49], Gabor channels [50,

51], and Laguerre-Gauss (LG) functions [6, 52]. The channel filters provide a mechanism for partial adaption to the signal profile and the noise structure. Because of the advantages of channels to capture the main features and derive the response properties of molecular physiology, the CHO is used for objective evaluation of lesion detection in clinical data.

2.2.4 Assessment of Binary Detection/Classification Tasks

This dissertation focused on a binary detection task, which was determined by two hypotheses based on signal contrasts (i.e., H_1 and H_2). Similar to the signal-detection approach, the material classification (or discrimination) task falls within the same category of a "decision task" in imaging literature, as the observer decides based on the given signal contrast, which of two materials was present [8]. An observer decided which of the two hypotheses (e.g., Lesion-Present/Lesion-Absent or the signal composed of Material 1/Material 2) was true from an image. Let us denote $\mathbf{s}_i$ as the signal $i = \{1,2\}$ to be detected, $\mathbf{b}$ as the noiseless image background, and $\mathbf{n}$ as the measured noise in the image. Then the image, $\mathbf{g}$, under the two hypotheses can be expressed by:

$$H_1: \mathbf{g} = \mathbf{b} + \mathbf{n} + \mathbf{s}_1, \tag{1}$$

$$H_2: \mathbf{g} = \mathbf{b} + \mathbf{n} + \mathbf{s}_2. \tag{2}$$

An observer detected or classified the image, $\mathbf{g}$, to each of the two hypotheses by comparing a test statistic (t) to a certain threshold (t_c). Figure 3 shows an example of probability distribution for each of the two hypotheses. When t is less than t_c, H_1 holds and the image is classified as Hypothesis 1 (e.g., Lesion-Present or Material 1). Otherwise, H_2 is satisfied and the image is classified as Hypothesis 2. The performance of separating the two hypotheses could be expressed in terms of the observer's SNR and AUC.

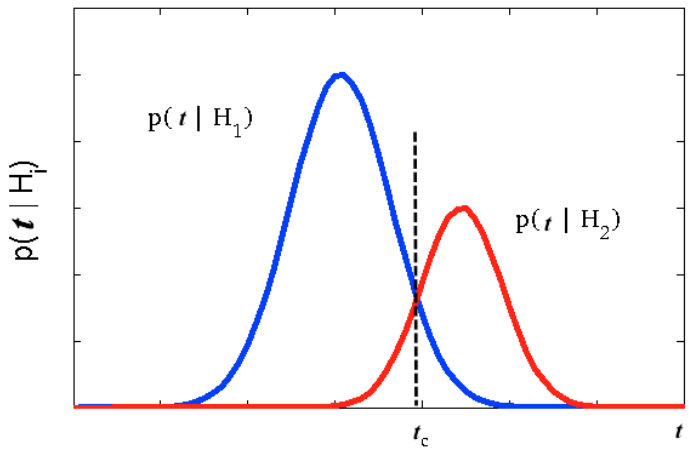

Figure 3 An example of conditional probability distributions $p(t \mid H_1)$, $p(t \mid H_2)$, and decision threshold t_c, given the signal contrast composed of Hypothesis 1, H_1, or Hypothesis 2, H_2.

2.2.4.1. Signal-Known-Exactly and Background-Known-Exactly (SKE/BKE) Task

The signal detection/classification task was performed to discriminate between two hypotheses based on the standard detection of Signal-Known-Exactly/Background-Known-Exactly (SKE/BKE). For a quantitative system evaluation, SKE/BKE provides a useful model of an interesting object as a known deterministic contribution of signal (i.e., based on size, shape, contrast, and location) together with statistically known background given to the observer [53]. The determination task was to classify which of the two hypotheses in the image was comprised based on the observed signal contrast, and this then resulted in the FOM of the detection/discrimination performance. In SKE/BKE problems, the only source of randomness was the measurement noise. The SKE detection tasks served as a good starting point for investigating the signal discrimination task; however, this simplified task was not clinically realistic, since the observed material density or concentration might not be constant in the human body.

2.2.4.2. Signal-Known-Statistically and Background-Known-Exactly (SKS/BKE) Task

To mimic a scenario in clinical practice, a more clinically relevant framework of task-based assessment to compare the performance on medical imaging was used. In the straightforward SKE/BKE paradigm, the FOM is higher if higher signal-to-noise is simply satisfied. In addition to SKE/BKE, the Signal Known Statistically / Background Known Exactly **(**SKS/BKE) task was used, which allowed variability in the signal [34, 53]. In contrast to SKE/BKE, the additional signal uncertainty specified by a statistically defined distribution was incorporated to investigate a more complex detection/discrimination task. A property of the signal to be investigated was varied according to specified statistical distribution. The shape of the signal was known but its properties (e.g., density or concentration) was not precisely known.

2.3 Section II: Clinical Applications Studied for Multidimensional Images

2.3.1 Assessment of Detection Performance in Oncologic PET

2.3.1.1. Basic Principle of PET

Positron Emission Tomography (PET) generates functional images depicting the distribution of positron-emitting nuclides in patients. PET scanners comprise of several rings of detectors surround the patient and detect annihilation coincidence detection (ACD) to obtain projections of the activity distribution in the subject. The PET system then performs a reconstruction of this data to create functional images [3].

Neutron-deficient isotopes undergo nuclear decay by the emission of a positron, or positive electron, and a neutrino. A positron has the same mass, but opposite charge to that of the electron.

Positrons are initially emitted with a small amount of energy and rapidly lose by collisions with the atoms in the surrounding tissue. Once the positron energy becomes relatively small, the positron interacts with a free electron in the tissue resulting in a matter-antimatter annihilation from which two photons emerge almost 180° opposed. When a positron annihilates, two 511 keV photons are emitted and interacted with detectors. The annihilation occurred approximately to the line connecting the two interactions. Within the scanner, the coincidence circuitry detects interactions undergoing nearly simultaneously, a process called annihilation coincidence detection (ACD) [3, 54].

A major importance of PET accounts on the physiological nature of elements such as carbon, nitrogen, and oxygen. Radionuclides can be used to label natural substrates that participate in human metabolism and these radio-labeled nuclides are indistinguishable from their unlabeled counterpart. To avoid perturbation of the metabolic process, only necessary trace amounts of the substrates are administered to the subject. The positron-emitting isotope of ^{18}F is widely used to label and becomes the glucose analog forming ^{18}F-fluorodeoxyglucose (FDG), a tracer of glucose metabolism. With a 110 min half-life, ^{18}F is a convenient nuclide that can be produced off-site at a remote cyclotron and transported to the PET facility, unlike the short half-lives of the isotopes such as ^{15}O (2 min), ^{13}N (10 min), ^{11}C (20 min) [54].

2.3.1.2. Benefits of PET in Oncology

Cancer is one of the leading causes of mortality in both men and women worldwide, accounting for approximately 1 of every 4 deaths. In 2013, only in the US, more than 1,660,000 new cancer cases are expected to be diagnosed and more than 580,000 Americans (almost 1,600 people a day) are projected to die of cancer [55]. The major challenge in detecting and treating cancer is

that diagnosis is usually made after the disease has already been in advanced stages, as patients often show no symptoms.

Positron emission tomography (PET) imaging provides significant diagnosis, staging, and restaging with sensitivity of 90% - 100% and specificity of 80% - 95% for most cancers, including lung cancer, colorectal cancer, lymphoma, melanoma [4, 56]. PET is primarily used to examine for early detection of cancers and the response to chemo- and radio-therapy, outcomes not achievable with magnetic resonance (MR) imaging or computer tomography (CT) alone. Because PET imaging lacks details of the underlying organ structure, integrated multimodalities of PET-CT or PET-MR have emerged and offer the combination of the high sensitivity of PET as well as structural information of CT or MR. This integration allows clinicians to determine whether tissues are cancerous and also permits precise anatomical localization of the lesions. The increased accuracy of quantification in oncology achieved are: 1) detection tumor initially not seen on CT, MR, or PET; 2) more precise location of tumor and a better delineation of the surrounding structures; and 3) better characterization of the tumor as benign or malignant [57]. The improvement of multimodality PET has tremendously increased to exam in oncologic patients.

2.3.1.3. Improvement of Oncologic PET

In clinical oncology, accurate determination of tumor location, dimension, and volume for diagnosis and staging is crucial for optimum management of a patient with cancer [58]. Clinical information combined with imaging findings is often used to calculate a likelihood ratio for malignant disease. If the malignant likelihood ratio is relative low (e.g., < 5% for lung cancer), the patient can be monitored without biopsy. However, approximate 50% of the patients undergoing surgical biopsy of an indeterminate tumor (e.g., malignant likelihood ratio between

5% and 60% for lung cancer) have benign disease [4]. As a result, it causes inappropriate invasive procedure and increases patient's cost.

Because multimodality PET (PET-CT or PET-MR) has taken the evaluation of tumor beyond morphology and is a better predictor to determine whether lesions are benign or malignant, multimodality PET scans are potentially proposed to eliminate the unnecessary surgical biopsy. Nevertheless, problems and pitfalls, such as patient movement, respiratory misregistration, and attenuation correction, remain major issues in the interpretation of the multimodalities of PET. Continuing improvement of multimodality PET instrumentation, acquisition, and quantitative methods has dramatically increased to overcome these issues.

2.3.2 Assessment of Plaque Classification in Spectral CT

2.3.2.1. Basic Principle of Spectral CT

Spectral CT utilizes spectral information to identify different materials beyond conventional CT. It facilitates better discrimination of tissue to differentiate materials, such as tissues containing calcium and iodine, which can appear similar on traditional CT techniques. Spectral CT takes advantage of the energy-dependent property of attenuation of X-ray photons after passage through a target tissue. Tissue attenuation characteristics of each substance can be measure or differentiated by this X-ray photon attenuation information. In clinical practice, spectral CT is employed in the approach of dual-energy CT that uses two X-ray spectra to enable material differentiation by analyzing material-dependent photoelectric and Compton effects. Recently, energy-sensitive photon-counting detectors are developed to extract the material-specific attenuation characteristics curves at multiple energy levels and within narrow energy bands [59, 60].

In conventional CT studies, the differentiation and morphology of tissues is based on voxel-specific CT numbers. Conventional CT measures the cumulative attenuation over the entire energy range of energies within a voxel for all tissues, not the response at different, specific energy levels. The CT number is commonly displayed in different greyscales, quantified in Hounsfield units (HU). Despite different materials such as calcium and iodine may have similar CT numbers at certain concentrations, they will not be differentiated in a conventional CT acquisition [59].

In principle, the attenuation of any material represented by its CT number is originated by a combination of photoelectric and Compton effects. These two main mechanisms are both energy- and material-dependent contributing to CT attenuation. Compton scattering independently occurs in the form of inelastic scattering of photons at energies exceeding ~30 keV. The photoelectric effect is the phenomenon in which electrically charged particles are released from or within a material when it absorbs electromagnetic radiation. It is essentially energy-dependent and predominates at lower photon energies. The photoelectric effect is influenced by high atomic numbers, whereas the Compton effect is predominately associated to material densities. Hence, these two mechanisms vary at different energy levels [3].

Because the attenuation coefficients are very dependent on the spectrum of energies in the X-ray beam used to produce the image, distinct energy characteristics of X-ray quanta can differentiated by technical approaches of developed detectors or both detectors and sources. There has been attempts to utilize spectral information for tissue characterization in particular techniques of dual-energy CT and multi-energy CT, such as dual-source CT, rapid voltage switching, layer detectors, photon-counting detectors. The major aim of the technical development is to provide information related to the varying response of tissues to X-rays of

different energies. Material differentiation and elemental decomposition thus become possible [59, 61].

2.3.2.2. Atherosclerotic Plaque

Atherosclerosis-related cerebrovascular (CV) and cardiovascular events, such as ischemic stroke and myocardial infarction, are the major leading causes of morbidity and mortality worldwide [62, 63]. The presence of atherosclerotic plaque is an independent predictor of risk for these events. For example, plaques with certain morphologies have prognostic value independent of and incremental to the presence or absence of luminal obstruction (stenosis) associated with the plaque [64]. It is also known that the prevalence of severe carotid artery stenosis is a predictor of poorer CV outcome, and that it increases progressively concurrent with coronary artery stenosis [62]. Therefore, the detection of plaque and assessment of its vulnerability are crucial for calculating the risk for stroke and sudden cardiac death.

In particular, plaque vulnerability can be assessed by resolving several features including: thin cap fibroatheroma, large lipid core, intimal spotty calcification, positive remodeling, and intraplaque neovascularization [33]. Low-grade stenosis may also be associated with increased risk of the future acute events involving carotid and coronary arteries, so determination of plaque features beyond the degree of stenosis is important [65]. Thus, for each imaging examination, it is not only necessary to identify plaques that create luminal obstructions, but also necessary to interpret and characterize plaques that typically form within the arterial vascular system.

2.3.2.3. Shortcomings of CT in Plaque Imaging

Conventional computed tomography (CT) and CT angiography (CTA) are well-established techniques that are frequently used for the detection and characterization of calcifications within

vessel walls [66]. CT provides an absolute quantitative measure of tissue composition, and enables grading of the severity of stenosis when evaluating stroke patients [67]. Although the detection and quantification of calcium can be performed with high accuracy using CT, this method is still deficient in its ability to characterize different constituents of mixed or purely noncalcified plaques, particularly in smaller plaques and vessels [61].

Typically, CT may be limited in its ability to clearly distinguish plaques from surrounding soft tissues or from contrast agents, since each may yield the same X-ray attenuation coefficient and thus the same grayscale value of CT number or Hounsfield unit (HU). For example, calcified plaques and iodine in a contrast-filled vessel are chemically distinct, but they can have similar X-ray attenuation integrals, which can render them difficult to distinguish in a CT image. Consequently, the major limitations of CT are: 1) an insufficient contrast between different soft tissues for some clinical tasks, in particular relative to MRI; 2) a lack of specificity when distinguishing different tissues which may present with similar pixel intensities; 3) the relatively high-dose nature of CT scanning as compared to other image modalities (e.g., MRI); and 4) frequently provided qualitative grayscale pixel values of CT images, rather than quantitative linear attenuation coefficients [68]. These shortcomings of CT may consequently hinder the proper assessment, differentiation, and characterization of the various structures and features important to plaque imaging.

2.4 Section III: Improvement to Current Imaging Methods

2.4.1 Improvement of Respiratory-Gated PET in Lesion Detection

2.4.1.1. Respiratory Motion Problems

One confounding factor that reduces sensitivity of lung cancer diagnosis with duality PET imaging is related to differences in breathing patterns between the CT or MR and the PET acquisitions [69]. Respiratory motion has an impact on the accuracy of lesion detection due to the fact that thorax PET scans acquired over several minutes (6-9 minutes) [70]. CT scans can be acquired within seconds (~15 seconds) [70] or during a breath hold. In contrast, PET acquisitions are taken during tidal breathing and represent an average diaphragm position [71]. A MR imaging examination typically takes much longer than a CT exam, patient motion is likely to cause even more severe artifacts in PET-MR than in the PET-CT [72]. The mismatched temporal resolution leads the significant misregistration of pulmonary nodules between the two modalities, especially at the lung bases where differences in position may approach 15 mm [71]. As a result, the lesion appears blurred and deformed in the PET image causing clinicians to overestimate both lesion sizes and shapes, finally deliver overdose radioactive drugs to patients.

2.4.1.2. Respiratory Gating Acquisition

Respiratory gating is a technique that allows clinicians to more precisely detect and treat lung cancer with multimodality PET imaging. By tracking the breathing pattern of the patients, the respiratory gating mechanism correlates lesion positions in relation to the patients' respiratory

cycle to remove the breathing motion from PET images. The respiratory gating takes account of a triggered procedure (e.g., amplitude (displacement), fixed time, or phase gating) and the original data are consequently binned into multiple intervals according to the trigger signal in the respiratory cycles. Each binned dataset is then reconstructed to obtain the image corresponding to its time interval [70]. This technique reduces motion artifacts (e.g., lesion smearing effect) and thus improves lesion quantitative assessment, which is severely compromised by respiratory motion in the thorax without gating [73-75].

2.4.1.3. Assessment of Detection in Non-Small Cell Lung Cancer (NSCLC)

Detection and estimation of uptake in lung lesions is of critical importance to early detection and accurate staging of non-small cell lung cancer (NSCLC) [76]. NSCLC, adenocarcinoma or large cell carcinoma of the lung, accounts for 75-80% of lung cancer and the frequency of occult metastasis may be high as 30%, which may cause for approximately 1.37 million deaths each year [4, 56]. ^{18}F-fluorodeoxyglucose (^{18}F-FDG) PET is sensitive for detection of metastases and provides optimal staging to determine the best possible therapeutic option and predict the outcome of the patient. During a PET scan, a lung lesion may move and deform due to respiratory motion, leading to a blurred final static image for the physician to interpret. Gating the PET data according to patient respiration produces multiple datasets that contain lower overall signal, but more defined lesion location, size, shape, and radiotracer uptake [77]. Nehmeh *et al*. [78] demonstrated an improvement in delineating tumor boundaries and estimating tumor standardized uptake value (SUV) when using respiratory-gated ^{18}F-FDG PET than using statically acquired data. Respiratory gating is therefore of importance for accurate lesion detection and quantification.

Respiratory gating is not yet standard practice in current PET thoracic imaging. There is, however, a large body of evidence that respiratory gating provides potential improvements in detection and quantification of thoracic malignancies. Boucher *et al*. [79] demonstrated feasibility of obtaining respiratory-gated data using a temperature-sensitive device to trigger the gating cycle. Klein *et al*. [80] have created a 4D affine registration model for gated PET data and built a working system [81]. Lalush *et al*. [82] undertook a human observer study of cardiac-gated SPECT data to study the importance of the number of gated frames on detection performance.

The major disadvantage of respiratory gating technique is the reduced statistics of data because each gate contains only a proportion of the acquisition. As a result, the reconstructed images usually have lower SNR than that of the non-gated data [83]. Respiratory-gated PET is commonly corrected motion of all gated frames and summed together to allow all count statistics available throughout a respiratory cycle [84].

2.4.2 Improvement of Kinetic Parametric PET in Lesion Detection

2.4.2.1. Variability of Tumor Uptake

Accurate detection and characterization of the tumor uptake are difficult because of the variability caused by biological and non-biological effects manifested in PET images. The accurate detection and quantification of tumoral ^{18}F-FDG uptake are essentially crucial in the evaluation of tumor response in therapeutics. Detection of changes in tumor glucose metabolism demonstrates the evaluation of therapy response, especially early decreases after cycles of therapy. Typically, the spatial distribution of a radiotracer in the body is time varying and depends on a number of biologic factors that can add variably and unpredictably impact PET

activity. The changes in PET caused by patient biology can be interstitial dose infiltration, presence of diabetes, other blood glucose changes, or changes in perfusion. In addition, the variation in PET measurement caused by the injected dose, alterations in blood pool activity, the time of imaging, the user analyzing the study, and mathematical factors (e.g., ROI, volume averaging) can also alter the accuracy of PET. An alternative method that overcomes the PET limitations is required to better estimate the biologic process for tumor uptake.

2.4.2.2. Kinetic Analysis in Dynamic PET

Analysis of time-course (dynamic) PET can provide more accurate assessment of tumor metabolic rate changes beyond other post-hoc analysis methods of static images for tumor characterization and treatment response monitoring. The dynamic or temporal component of a radiotracer is crucial in nuclear medicine studies because measuring PET imaging as a function of time relative to the administration of the radiopharmaceutical reflects more precise the biologic process of interest. Using dynamic imaging, we can derive the rate of change of radiotracer concentration, in which often provides direct information on the rate of a specific biologic process. Zhuang *et al*. [85] reported that malignant lesions showed a significant increase in signal over time while benign lesions showed a decrease over time. Thus, constructing mathematical kinetic models with a set of one or more parameters known as ‘tracer kinetic models’ can be used to understand the biologic mechanism of the radiotracer in tumor metabolism based on dynamic PET imaging [1].

According to PET images are composite of various superimposed signals, a mathematical kinetic model is used to isolate the desired component of the signal related the dynamics of the tracer molecule through modeling of ‘compartments.’ Each compartment is characterized by the concentration of the tracer where it is present as a function of time. Kinetic parameters can be

then estimated through sets of ordinary differential equations, which express the balance between the mass entering exiting (flux constants) each compartment, thereby extracting precise information of glucose metabolism [25]. Currently, there are several kinetic modeling techniques used to quantify the kinetic parameters of dynamic PET such as simplified graphical approach (Patlak) [86, 87] and compartmental model analysis (CMA). Parametric imaging derived from dynamic PET allows the estimation of kinetic parameters that intrinsically characterize tumor metabolism or perfusion in a more accurate manner than SUV. It should overcome potentially misleading static SUV, a simple semiquantitative analysis commonly used to quantify metabolic function with FDG-PET.

2.4.2.3. Assessment of Kinetic Parametric PET Imaging in Oncology

More recently, parametric PET imaging has become a more accurate modality in oncology; however, objective image assessment is very limited. Krak *et al*. [88] found that SUV well correlated with compartmental modeling and Patlak analysis, but SUV was less accurate in detecting changes in ^{18}F-FDG kinetics during therapy in 20 breast cancer patients. Messa *et al*. [89] reported that the estimated parametric images using the Patlak graphical analysis increased the contrast between tumor and normal liver, thereby facilitating both tumor detection and quantification. Necib *et al*. [90] utilized the parametric imaging approach to characterize early metabolic tumor changes in 78 lesions from FDG PET-CT scans of patients with metastatic colorectal cancer during chemotherapy. They showed that this approach correlated well with the standard response assessment, possibly highlighted heterogeneous tumor response, and provided quantitative parameters characterizing tumor changes. Karakatsanis *et al*. [91] extracted parametric images from whole-body PET using Patlak through their proposed clinically imaging framework. They showed that parametric images potentially achieved tumor contrast-to-noise

ratio (CNR) enhancement over SUV. Veldt *et al*. [92] used radioactive water ($H_2{}^{15}O$) to validate the quantitative accuracy of parametric perfusion images in NSCLC patients. They reported that the parametric perfusion images had improved delineation accuracy as well as excellent image quality and quantitative accuracy. Muzi *et al*. [93] assessed *in vivo* lung tumor proliferation using 3'-deoxy-3'-^{18}F-fluorothymidine (^{18}F-FLT) and two-compartment model analysis. The comparison results showed correlated well with *in vitro* assay of proliferation measured in tissue derived from surgical resection. Moreover, they reported that the compartmental analysis with the 3-parameter model and graphical approaches significantly underestimated by 25% - 30% as compared with the 4-parameter compartmental model.

2.4.3 Improvement of Spectral CT in Plaque Classification

2.4.3.1. Dual-Energy CT

Spectral CT, which generates additional material-different information by collecting data using more than one single-source energy spectrum, shows promise for mitigating several limitations of conventional CT. Spectral CT improves material differentiation by combining CT techniques with measurement of the energy-dependent (i.e., spectral) attenuation properties of the examined tissues [94]. Dual-energy CT (DECT) is the simplest and currently most broadly-used implementation of spectral CT. Several types of DECT systems have been designed that make use of different technical approaches, which can be mainly classified to two major approaches: the source-driven approach and the detector-driven approach [61, 95]. In the source-driven approach, it relies on the X-ray source to provide different ranges of X-ray energy photons at either different times or different orientations. Dual-source CT has two X-ray sources running at different voltages with two corresponding detectors at angular offset of 90° mounted onto the

rotating gantry, e.g., Somatom Definition and Somatom Definition Flash (both by Siemens Healthcare; Forchheim, Germany). Fast kVp-swiching CT includes a single-source ultra-fast kV-switching system where two consecutive datasets at two different kVps, typically, 80 and 140 kVp, are acquired, e.g., GE Discovery CT750HD (GE Healthcare; Milwaukee, WI). For the detector-driven approach, it is characterized by energy discriminating detectors having an upper and a bottom scintillator, which stops and detects the lower-energy and higher-energy X-ray photons, respectively. Dual-layer CT acquires single X-ray source CT data using two scintillation layers on top of each other, e.g., consisting of CsI or ZnSe in the top and Gd_2O_2S in the bottom layer, which two energy datasets are acquired simultaneously, e.g., Brilliance 64-channel CT (Philips Research; Hamburg, Germany).

Although it makes use of the additional spectral information obtained through use of these several designs, current DECT technology still achieves only limited performance in plaque imaging. Specifically, DECT can offer high spatial resolution for plaque morphology measurement, but current limitations arise in the differentiation of materials with dual-energy CT when the two energy spectra used have a significant overlap [68]. In addition, DECT, such as dual-source CT, sometimes requires relatively high dose levels as compared to conventional CT [96] and is not safe for sequential studies [32]. As a result, these limitations currently exclude DECT from widespread use in several clinical applications and from serial studies in plaque imaging.

2.4.3.2. Multi-Energy CT

In contrast to DECT, multi-energy CT (MECT) with well-defined multiple spectral windows potentially offers a higher degree of material specificity when distinguishing components of vulnerable atherosclerotic plaque through their energy responses. MECT has potential to better

characterize and quantify the concentration of the plaque components (e.g., water, lipid, and calcium) as well as various contrast agents (e.g., iodine, gadolinium, and gold) relative to DECT [32, 33]. The photon-counting detector approach is one technical approach to implementing MECT, since it can allow more than the two-energy windows available in DECT. CT based on photon-counting detectors measures each incident X-ray photon as it interacts with the detector and generates an electronic signal, with the measured event then accumulated into different bins based on the measured photon energy. Through the rapid progress of detector technologies in the last decade, several vendors have offered CT systems with both clinical and preclinical geometries, e.g., LightSpeed VCT (GE Healthcare; Waukesha, WI), Somatom Definition AS (Siemens Healthcare; Forchheim, Germany), the preclinical PCD-CT (Philips Research; Hamburg, Germany). Alternative designs for MECT systems may employ K-edge filters, and in one instance used multiple balanced K-edge filters [97].

By means of energy-resolved devices which can provide more accurate tissue characterization and quantification, MECT has satisfied several clinical demands in atherosclerotic plaque characterization including: 1) improving the contrast-to-noise ratio and contrast of CT images; 2) reducing the dose of X-ray radiation and contrast agents due to the ability to achieve a comparable contrast-to-noise ratio at lower dose efficiency when compared to DECT and conventional CT [98, 99]; 3) improving the spatial resolution of CT images; 4) providing better quantitative using well-defined energies; 5) allowing accurate K-edge imaging; 6) allowing simultaneous multiagent imaging; 7) enabling molecular CT with nanoparticle contrast agents and personalized medicine [68]. With these capabilities, MECT images are being investigated and evaluated to be ready for clinical use.

2.5 Chapter Summary

This chapter has described the understanding of the objective image assessment compositions that are essential to employ task-based assessment in medical imaging applications. The Hotelling and Channelized Hotelling observers are the essential basic elements making use to extend for higher dimensional data with no dimensional limitation in this dissertation. Several clinical applications have been improved by various techniques and the data become higher dimensions, which have more information domains as well as target signal information, e.g., respiratory-gated PET, kinetic parametric PET, spectral CT. The essential objective assessment metric in terms of diagnostic interpretation is required to evaluate the usefulness and improved image quality for multidimensional data of new development of image-acquisition or image-processing.

Part I

Modeling Framework for

Multidimensional Imaging Assessment

Chapter 3

A Novel Numerical Observer for Multidimensional Imaging

The purpose of this chapter is to explain the development of a novel numerical observer for multidimensional imaging. The first section describes the motivation and current status of the numerical observer used in medical imaging. Then, the development and design of the novel numerical observer for preprocessing and integration stages will be described.

3.1 Introduction

Image quality assessment studies are mainly limited only 2D and 3D analysis; however, there is substantial body of work showed that the use of additional signal information in numerical observers could lead to more accurate image assessment. Gifford *et al*. [100] studied multislice numerical observers incorporating the signal information in adjacent slices in an image stack, and found that the new observer could achieve better performance than the planar 2D observer. Kim *et al*. [101] compared the mathematical observers between 2D and volumetric 3D in whole-body PET oncological images. They demonstrated a significant increase in detectability

SNR of volumetric numerical observers when compared to the planar observer results. Recently, Platisa *et al*. [9] compared multiple designs of planar 2D CHO, multislice 3D-CHO (stack of planar 2D CHO), and volumetric 3D CHO for detecting 3D signals in volumetric images. They reported that the image quality assessment using fully 3D CHO had greater efficiency than using a conventional 2D CHO or a multislice 3D-CHO in different random backgrounds.

There are currently limited studies that accommodate 4D data in a numerical observer for assessing the observer performance in the signal detection task. Lee *et al*., [102, 103] developed a numerical 4D CHO and applied it to the task-based evaluation of gated-myocardial perfusion SPECT images. They reorganized the 4D images into a set of 2D cine images, treating a 4D image as a set of moving 2D images. Their numerical observer was constructed using a single large template defined as "space-time CHO template" used to compute the correlation of the spatial and temporal domains, simultaneously. Lee *et al*. used analytical inverse Fourier Transform of the product of disk and rect functions to form the channels. These channels were equivalent to using a cylindrical channel in the frequency domain (x, y) with the addition of time direction (t). The space-time template for spatial and temporal domain was then generated by a set of 2D difference of the space-time channels. Their validation was based on simulated images using the filtered-back projection (FBP) reconstruction, the 4D XCAT phantom, and an analytical projector. They reported that the AUC values of the developed 4D CHO (AUC = 0.69) showed improvement compared to 2D CHO and good agreement to a human observer study (AUC = 0.68). However, the observer proposed by Lee *et al*. is not fully 4D (3D+time) as it omits the correlation among adjacent slices within an image volume in the spatial domain. As reported by Platisa *et al*., [9] the multislice processing (stack of 2D slices) was suboptimal as compared to the fully 3D processing. Moreover, a clearly defined validation with a sufficient

number of datasets of this study is not yet reported. Despite the 4D analysis reported, there is insufficient validation of the 4D numerical observer development that fully incorporates the multidimensional information of data into the observer analysis.

The author developed a novel 4D numerical observer that incorporated both spatial and the fourth-dimensional information, e.g., temporal, parametric, spectral, for the quantitative figure-of-merit metrics in detection and classification tasks in multidimensional imaging. The design was motivated by Chen *et al.* [40] and Platisa *et al.*, [9] who proposed and applied a sophisticated two-layered numerical observer to volumetric images. Our design not only performs a series of spatial matched-filtering operations for each spatial image frame, but also introduces an additional processing directly on the fourth-dimension data to perform integral matched-filtering for the embedded spatiotemporal noise. The numerical observer was designed for detection or classification tasks based on a SKE/BKE task, in which the observer had full knowledge of target locations and noise properties. The fourth-dimension information was incorporated into the SNR by forming a 4D region around a target location. The first and second-order image statistics of the null hypothesis (e.g., lesion-absent) and alternative hypothesis (e.g., lesion-present) images were used to describe a decision variable, upon which the target present/absent decision was calculated throughout the cine volumes. The strategy of this numerical observer was to use all information about the signal's spatial and additional profiles to exploit the correlation of the signal components among different image frame. Our method could be used to evaluate the maximal performance that was obtained using the improved technology, whose additional information enhanced the system performance.

3.2 Development of Novel Numerical Observer

A computer-numerical observer accommodating all available information in noisy images was developed. This work was based on the detection of an exactly known signal superimposed on an exactly known background (SKE/BKE) with the signal locations known to the observer. Our numerical observer [104] consisted of two stages in which the first stage was preprocessing using a CHO for the spatial domain, followed by the second stage of a HO for the additional domain. Figure 4 illustrates the diagram and design of the proposed novel numerical observer and Figure 5 illustrates the design details of the novel numerical observer used for multidimensional images.

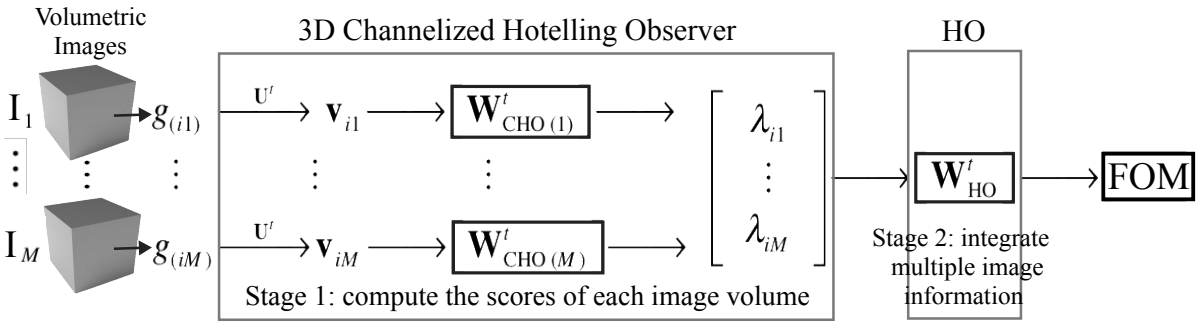

Figure 4 The schematic diagram of the proposed novel numerical observer.

3.2.1 CHO for Preprocessing Stage

The first step of the model computed the test statistics (decision variable) of signal-present and -absent in each individual image volume to independently indicate particular signals. A CHO model was applied to each volumetric image for measuring spatial information in each image volume. Let a considered image be in a $\Re^3$ domain. Elements of the $N\times N\times N$ volumetric window centered on a target were formulated into a $N^3\times 1$ column vector, $\mathbf{g_1}$, forming the

signal-present vector. The corresponding background vector, $\mathbf{g_2}$, was obtained using the same procedure to form the signal-absent vector, for all M image volume and N_R noise realizations.

The column vector, $\mathbf{g}$, was first processed by a set of channel functions, e.g., Laguerre-Gaussian (LG), Different-of-Gaussian (DOG) channels, [6, 14] to extract major features from the images [14, 105, 106]. For LG channels, they were used to introduce the smoothness assumption to the estimation of the Hotelling template. The aim of these channels was to reduce the dimensionality problem for increasing computation feasibility [2]. The LG channels were formed by a product of Laguerre polynomials and Gaussian functions, yielding symmetrically rotational functions with no preferred orientation in the correlation structure of the signal. With these properties, LG channels are suitable for spherical and non orientation-dependent targets. In this study, we used a 3D form of the LG functions, which can be defined in $\Re^3$ as:

$$u_{p,LG}(r) = \frac{\sqrt{2}}{a_u}\exp\left(\frac{-\pi r^2}{a_u^2}\right)L_p\left(\frac{2\pi r^2}{a_u^2}\right) \tag{3}$$

where p = 1, 2, … P is the channel number, r is the radial distance $\left(r \in \Re^3\right)$, a_u is the spread parameter or scaling factor of the LG channel, and L_p denotes Laguerre polynomials defined by:

$$L_p(x) = \sum_{k=0}^{p}(-1)^p\begin{pmatrix} p \\ k \end{pmatrix}\frac{x^k}{k!}, \tag{4}$$

where p = 1, 2,… P.

Alternative to the LG channels, DOG channels were used to extract the main features inherited in the images. DOG functions have long been used to model spatial-frequency selectivity in the human visual system [5]. These channels are defined as several bandpass profiles using the incorporation of the overlapping DOG functions to form the channel sensitivity.

The p^{th} channel profile is defined in the coordinate system of the displayed image and a channel profile $u_{p,DOG}(\rho)$ as a function of the 3D spatial-frequency variable ρ can be computed as:

$$u_{p,DOG}(\rho) = \exp\left[-\frac{1}{2}\left(\frac{\rho}{Q\sigma_p}\right)^2\right] - \exp\left[-\frac{1}{2}\left(\frac{\rho}{\sigma_p}\right)^2\right], \quad (5)$$

where σ_p is the selected standard deviation of each channel and the multiplicative factor $Q > 1$ defines the bandwidth of the channel. From an initial σ_0, each of the σ_p values in Eq. (5) is defined by $\sigma_p = \sigma_0 \alpha^p$. In this study, we used a dense set of DOG channels (denoted by D-DOG) utilizing ten channels with channel parameters of $\sigma_0 = 0.005$, $\alpha = 1.4$, and $Q = 1.67$. [5]

The channels were then formed into a matrix of visual channel functions, $\mathbf{U}=[\mathbf{u_1},\mathbf{u_2},\ldots,\mathbf{u_P}]$, where $\mathbf{u_i}$ is a $N^3 \times 1$ column vector of the channel and P is the number of the channels. The column vector of channel output, $\mathbf{v}$, was computed by a matrix-vector multiplication of the channel matrix $\mathbf{U}$ and the image column vector, $\mathbf{g}$, as:

$$\mathbf{v} = \mathbf{U}^T \mathbf{g}, \quad (6)$$

where T denotes the matrix transpose operator. Processing the images through the channels reduced the dimensionality of the dataset from N^3 to P. This procedure was applied to M image volume, N_R noise realizations, for both signal-present and signal-absent datasets.

Next, the variance of channel responses and the corresponding covariance between the different channel responses were calculated. The covariance matrix, $\mathbf{K_v}$, describing variance and covariance of channel responses was computed to determine the correlation of the signal within each image volume as:

$$\mathbf{K_v} = \mathbf{U}^T \mathbf{K_g} \mathbf{U}, \quad (7)$$

where $\mathbf{K}_{\mathbf{g}} = \frac{1}{2}\left(\mathbf{K}_{\mathbf{g},1} + \mathbf{K}_{\mathbf{g},2}\right)$ is the average covariance matrix with $\mathbf{K}_{\mathbf{g},i} = \left\langle \left(\mathbf{g} - \bar{\mathbf{g}}_i\right)\left(\mathbf{g} - \bar{\mathbf{g}}_i\right)^T \middle| H_i \right\rangle$, $i = \{1,2\}$, and $\bar{\mathbf{g}}_i = \left\langle \mathbf{g} \middle| H_i \right\rangle$. The operator $\langle \cdot \rangle$ denotes the ensemble average over all N_R noise realizations and $i = \{1,2\}$ refers to signal-absent and signal-present data, respectively. The covariance matrix $\mathbf{K}_{\mathbf{g}}$ describes the randomness in the data due to background variability and measurement noise.

In the spatial domain, the channelized Hotelling template, $\mathbf{W}_{\text{CHO}}$, was derived from the inverse of the covariance matrix of the channel responses and the mean difference of signal-present and signal-absent channel response vectors, $\Delta\bar{\mathbf{v}}$, from each image volume [8]. The template pre-whitens the correlated noise prior to the matched filtering operation. The CHO template is defined as:

$$\mathbf{W}_{\text{CHO}} = \mathbf{K}_{\mathbf{v}}^{-1}\Delta\bar{\mathbf{v}}, \tag{8}$$

where $\Delta\bar{\mathbf{v}} = \mathbf{U}^T\Delta\bar{\mathbf{g}}$ and $\Delta\bar{\mathbf{g}} = \left\langle \mathbf{g} \middle| H_2 \right\rangle - \left\langle \mathbf{g} \middle| H_1 \right\rangle$ is the mean difference of signal-present and signal-absent vectors.

Two sets of test statistics for all M image frames $\mathbf{t}\middle|H_1 = \left[\lambda_{11}, \lambda_{12}, .., \lambda_{1M}\right]^T$ for signal-absent and $\mathbf{t}\middle|H_2 = \left[\lambda_{21}, \lambda_{22}, .., \lambda_{2M}\right]^T$ for signal-present were computed by:

$$\lambda_{ij} = \mathbf{W}_{\text{CHO},j}^T\mathbf{v}_{ij}, \tag{9}$$

where $i = \{1,2\}$ and $j = \{1,2,...,M\}$.

3.2.2 Hotelling Observer for Integration Stage

The second step was a HO numerical that integrated the fourth-dimension information among multiple image frames. The column vectors of intermediate scores assigned to the M volumes for

signal-absent and signal-present were input to the HO numerical. The noise correlation within the fourth-dimension information was determined through an additional covariance matrix and an additional matched filter of the multi-image volumes. The 4D signal-to-noise ratio (4D SNR) was computed as the final outcome of this stage.

The statistic scores of the $M\times1$ column vectors, $\mathbf{t}|H_1$ for signal-absent and $\mathbf{t}|H_2$ for signal-present datasets, were pre-whitened to decorrelate over noise realizations. The additional covariance matrix, $\mathbf{K}_\mathbf{t}$, was computed by:

$$\mathbf{K}_\mathbf{t} = \frac{1}{2}\left(\mathbf{K}_{\mathbf{t},1} + \mathbf{K}_{\mathbf{t},2}\right), \tag{10}$$

where $\mathbf{K}_{\mathbf{t},i} = \left\langle \left(\mathbf{t} - \overline{\mathbf{t}}_i\right)\left(\mathbf{t} - \overline{\mathbf{t}}_i\right)^T \middle| H_i \right\rangle$, $i = \{1,2\}$, and $\overline{\mathbf{t}}_i = \left\langle \mathbf{t} \middle| H_i \right\rangle$.

The additional HO template, $\mathbf{W}_{\mathrm{HO}}$, was determined by multiplying the inverse matrix of the additional covariance matrix with the mean difference of the additional signal-present and signal-absent vectors as following:

$$\mathbf{W}_{\mathrm{HO}} = \mathbf{K}_\mathbf{t}^{-1}\Delta\overline{\mathbf{t}}, \tag{11}$$

where $\Delta\overline{\mathbf{t}} = \left\langle \mathbf{t} \middle| H_2 \right\rangle - \left\langle \mathbf{t} \middle| H_1 \right\rangle$.

Finally, the 4D SNR that completely integrated all the information throughout the entire data was determined:

$$\mathrm{SNR}_{4\mathrm{D}} = \left(\Delta\overline{\mathbf{t}}^T \mathbf{K}_\mathbf{t}^{-1} \Delta\overline{\mathbf{t}}\right)^{1/2}. \tag{12}$$

Alternatively, when the test statistic was normally distributed under both hypotheses, the final 4D SNR was able to be calculated using the final test statistics of the HO numerical through the mean signal minus the mean to non-signal data divided by the standard deviation of the entire signal, given the same output 4D SNR results as:

$$\mathrm{SNR}_{4\mathrm{D}} = \frac{\left\langle \tilde{\mathbf{t}} \middle| H_2 \right\rangle - \left\langle \tilde{\mathbf{t}} \middle| H_1 \right\rangle}{\left[\frac{1}{2}\mathrm{var}\left(\tilde{\mathbf{t}} \middle| H_2 \right) + \frac{1}{2}\mathrm{var}\left(\tilde{\mathbf{t}} \middle| H_1 \right) \right]^{1/2}}, \tag{13}$$

where $\tilde{\mathbf{t}} = \mathbf{W}_{\mathrm{HO}}^{T}\mathbf{t}$ is the test statistic computed in the fourth-dimensional domain. Note that if the test statistic is not normally distributed under both hypotheses causing a highly skewed probability density function (PDF), the variance is not a good measure of the spread of the decision variable, and the figure of merit in the expression of Eq. (13) is not useful. However, Eq. (12) was preferred because there was no required condition of the test statistics.

Furthermore, AUC is an alternative of the SNR figure of merit and is often used to quantify the performance of the numerical observer in the objective image quality assessment. SNR can be used to calculate AUC by using the relationship expressed in Barret *et al*. [106] when the test statistic is normally distributed under both hypotheses as:

$$\mathrm{AUC} = \frac{1}{2} + \frac{1}{2} erf\left(\frac{\mathrm{SNR}}{2} \right). \tag{14}$$

3.3 Discussion

Our 4D numerical observer design could improve performance because it appropriately integrated both the spatial information of each image volume and the fourth-dimension information. In the first stage, the CHO from each individual volumetric image was computed to take account of the measurement noise distributed within the image independently. Subsequently, the statistical image information for all adjacent image volumes was integrated through the additional processing step using the HO model. This numerical observer computed the information of a spatiotemporal correlation among the consecutive volumes, thereby increasing the detectability performance.

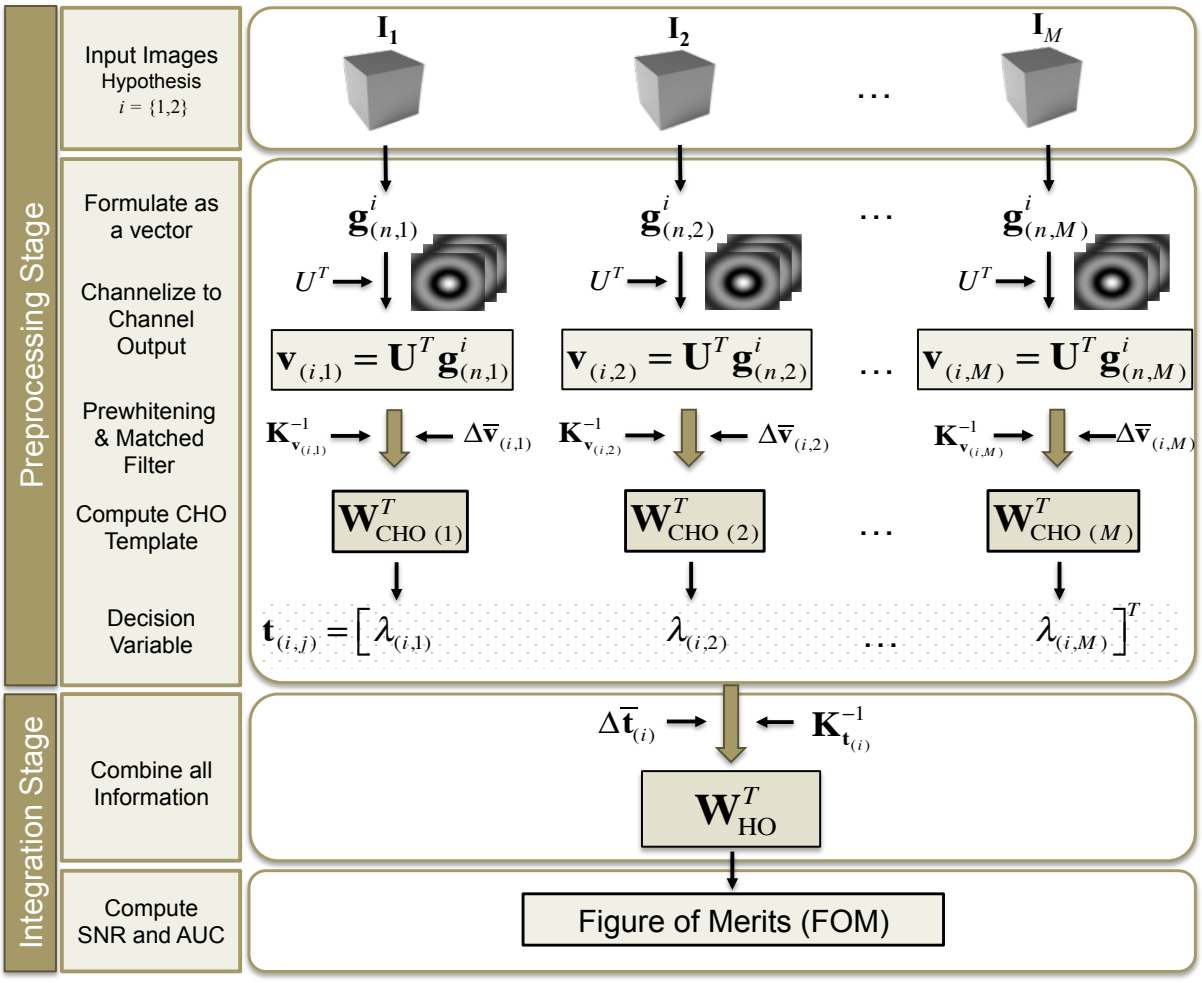

Figure 5 The design of the proposed numerical observer for multidimensional images. In the figure, $\mathbf{g}_{(n,j)}$ is the vector representing the image within ROI, $n=N^3$ is the number of voxels in the ROI, i is the hypothesis index. Top row, two material images for each energy bin are input and U^T is the channel matrix, where the operator T is the matrix transpose.

The localized processing of the complex CHO/HO models had an impact on the detectability performance. The two-layered numerical observer locally processed data using a localized covariance matrix and a localized matched filter that were close to the data both in the spatial and fourth directions. In each image volume of the first stage, a localized covariance matrix decorrelated the data yielding a spatial correlation matrix that had a flat or white,

eigen-spectrum [8]. Whereas in the second HO layer, the array of the test statistics obtained from the spatial processing was locally prewhitened within the additional domain. Likewise, a spatial- and an additional matched-filter were locally processed to particularly correlate signal within the series of the volumetric data. This localized processing assessed the statistics of data intimately in the signal detection computation.

The localized processing not only enhanced the prewhitening and matched-filter calculation, but also provided an appropriate approximation of the data statistical information used for the CHO/HO computation. The HO and CHO models support both Gaussian and non-Gaussian distributed data. If the data are Gaussian distributed, HO is identical to the ideal observer (IO), providing the maximum SNR values or an absolute upper bound on signal detectability [43]. If the data are non-Gaussian, HO requires knowledge of only the first- and second-order statistics of the data (mean and variance) to model the data as Gaussian PDF, regardless of the data's true statistics [8]. In our study, the final reconstructed images were non-Gaussian distributed. Thus, the CHO and HO models use the mean and covariance of the data to approximate the PDF in the computation both in spatial and temporal processing. This approximation of the Gaussian PDF estimated from the mean and covariance 'locally' within each image volume was appropriate, thereby providing decent data approximation for the CHO/HO computation.

3.4 Chapter Summary

This chapter has shown the effective design and the development of the novel numerical observer that accommodates multidimensional information of the images. The proposed numerical observer constructs with a 3D Channelized Hotelling Observer (3D CHO) for the spatial domain in the preprocessing stage, and then follows by a Hotelling Observer (HO) for the

additional domain in the integration stage. This design is universal with no limitation of the image dimension. The next chapters demonstrate the essential applications benefiting from this observer development.

Part II

Translational Applications to

Multidimensional Imaging Methods

Chapter 4

Lesion Detection in Respiratory–Gated PET

The purpose of this chapter is to describe the application of the proposed numerical observer to respiratory-gated PET imaging. This chapter focuses on the validation of the proposed framework using simulated data. The first section describes on the overview of the current status of the research study. Next, the methodology of the generation of simulated images using digital phantoms with GATE simulations will be described. Then, the performance comparison of 4D numerical observers with 2D and 3D channels, different noise levels, motion, lesion contrast, lesion size, the number of iterations and subsets in image reconstruction will be illustrated.

4.1 Introduction

Respiratory-gated PET/CT protocols reduce lesion smearing and improve lesion detection through a synchronized acquisition of emission data. However, an objective assessment of image quality of the improvement gained from respiratory-gated PET is mainly limited to a three-dimensional (3D) approach.

In this chapter, the author applied the proposed 4D numerical observer that incorporated both spatial and temporal information for detection tasks based on respiratory gating in pulmonary oncology. The image quality assessment of this imaging protocol is mainly limited to 3D analysis and it does not accommodate the cine volumes (3D+*t* or 4D) of respiratory-gated PET. The proposed 4D (3D+*t*) numerical observers utilized the knowledge of temporal information in the series of signal (e.g., 3D+time or 4D imaging).

It is known that human observers have the ability to use the temporal profile of a temporally modulated signal in information processing [107]. More specifically, the human visual signal detection uses both spatially (e.g., spatial frequency, phase, and locations) and temporally varying dynamic (spatiotemporal) noise to reach a decision on signal presence/absence. To mimic a human observer's performance on tasks involving spatiotemporal data, numerical observers should support temporal noise. There is a substantial body of work studying the effect of temporal signal changes, including signal phase and contrast changes, on detectability [108]. Xue and Wilson [109] extended work to measure the detectability of a moving cylinder in pulsed-*x*-ray fluoroscopy, allowing temporal correlations between frames to model the observed human ability to use some temporal filters. However, studies involving integration of temporal signal in the numerical observers remain limited. The author aimed to extend these studies to respiratory-gated PET data using model observers to obtain an objective assessment of the expected improvement.

Typically, gated-PET data are viewed for diagnosis in two ways: 1) the individual gated images can be registered back to a reference gate to create a single image with respiratory motion removed, or 2) the physician can view the gated images as a cine movie and look for the motion of a lesion. The latter is used extensively for reading respiratory-gated CT data. According to

intuition of the latter viewing, our numerical observer functions in the way that the PET images are displayed in animated 3D images in which an observer can view the moving 3D images. It is similar to the practical manner that the clinician usually investigates a tumor on a 2D display in coronal, transverse, and sagittal planes with moving pictures simultaneously. A fully spatio-temporal (4D) numerical observer may provide a superior image quality assessment for the improvement obtained from respiratory-gated PET. This is similar to how the human visual system uses motion in visual cine for noise reduction, because the human eyes tend to temporally average the noise [107]. Therefore, the author applied the proposed numerical observer for detection of spatiotemporal signal in cine volumetric images with spatiotemporal noise.

The proposed novel 4D numerical observer incorporated both spatial and temporal information for the lesion detection task in respiratory gated-PET imaging [104]. The proposed design not only performs a series of spatial matched-filtering operations for each gated frame, but also introduces an additional processing directly on the gated (i.e., temporal) data to perform temporal matched-filtering for the embedded spatiotemporal noise. The numerical observer was designed for lesion detection based on a SKE/BKE task, in which the observer had full knowledge of lesion locations and noise properties. The temporal information was incorporated into the SNR detection by forming a 4D region around a lesion location, where the fourth dimension was the number of gates. The first and second-order image statistics of the null hypothesis (lesion-absent) and alternative hypothesis (lesion-present) images were used to describe a decision variable, upon which the lesion present/absent decision was calculated throughout the cine volumes. The strategy of this numerical observer was to use all information about the signal's spatial and temporal profiles to exploit the correlation of the signal components among different gates. Lesion detectability assessed by our numerical observer is

more accurate to perform the objective assessment of the expected improvement gained compared with the respiratory-gated study.

Realistic ^{18}F-FDG activity distributions were simulated using a 4D eXtended Cardiac Torso (XCAT) anthropomorphic phantom including 12 spherical lesions at different anatomical locations (lower, upper, anterior, and posterior) within the lungs. Simulated data based on Monte-Carlo simulation were obtained using Geant4 Application for Tomographic Emission (GATE). Fifty noise realizations of six respiratory-gated PET frames were simulated by GATE using a model of the Siemens Biograph mMR scanner geometry. PET sinograms of the thorax background and pulmonary lesions that were simulated separately were merged to generate different conditions of the lesions to the background (e.g., lesion contrast, motion). A conventional ordered subset expectation maximization (OSEM) reconstruction (5 iterations, 6 subsets) was used to obtain: 1) gated, 2) non-gated, and 3) motion-corrected image volumes (a total of 3,200 sub-image volumes: 2,400 gated, 400 non-gated, and 400 motion-corrected). Lesion detection SNR were measured in different lesion-to-background contrast levels (3.5, 8.0, 9.0, 20.0), lesion diameters (10.0, 13.0, 16.0 mm), and respiratory motion displacements (17.6 - 31.3 mm). The proposed 4D numerical observer applied on multiple-gated images was compared to the conventional 3D approach applied on the non-gated and motion-corrected images.

4.2 Overview of Methodology

To validate our numerical observer, we simulated respiratory-gated PET using Monte Carlo simulations and a 4D XCAT phantom with inserted pulmonary lesions. The data simulation was performed using the GATE Monte Carlo simulation, which is widely used in such highly clinical-oriented studies (e.g., SPECT, PET, CT, and dosimetry applications). The assumptions

applied to this study were that there was no preferred orientation in the correlation structure of the background and the signal was spherically symmetric in a known location. The lesions were simulated with different contrast levels and sizes at different locations within the lungs. Lesion detectability was assessed using three methods: 1) the volumetric 3D CHO on the non-gated reconstructed images (3D-CH-NG), 2) the volumetric 3D CHO on the motion corrected images (3D-CH-MC), and 3) the 4D numerical observer on multiple-gated images (4D-N-G). The results showed that 4D-N-G yielded better lesion detectability than both 3D-CH-NG and 3D-CH-MC. This study shows that additional temporal information can be used to improve lesion detectability for respiratory-gated PET imaging.

4.3 Generation of Simulated Images

The lesion detection performance of the 4D numerical observer was evaluated using computer-simulated data. A digital anthropomorphic XCAT phantom with a set of spherical lesions within the lungs was used to generate realistic ^{18}F-FDG gated activity distributions. This simulation mimics the acquisition obtained from a conventional PET/CT scanner with a respiratory-gated protocol, triggered using a commercially available respiratory gating device. The 3D acquisition of a single-bed gated PET scan of the thorax was simulated frame-by-frame within a respiratory cycle. The 4D XCAT was used to generate the voxelized activity distributions together with the corresponding attenuation maps. The motion fields were also generated for 6 equal-time bins of a respiratory cycle. The GATE Monte-Carlo simulation software [110] was used to model a clinical PET scanner geometry and to generate PET coincidence events based on the XCAT activity/attenuation distributions. Poisson-thinning process was applied to generate multiple noise realizations on the PET sinograms. The major

steps of the data generation are: 1) to simulate noise-free data, 2) to apply the Poisson-thinning process to the sinogram space for obtaining multiple noise realizations, and 3) to fuse the sinograms and reconstruct images.

4.3.1 Digital Phantoms

The thorax images were obtained using the 4D XCAT phantoms, which modeled high-resolution human anatomic images with realistic patient motion. The 4D XCAT was originally developed for multimodality imaging research. It was designed with highly detailed anatomies using nonuniform rational B-spline (NURBS) and the Visible Male/Female anatomical datasets provided by the National Library of Medicine. Additionally, the 4D XCAT phantom also incorporates realistic parameterized models of human cardiac and respiratory motions [111]. Starting at the full exhalation, the voxelized phantoms were generated for 6 gated-respiratory histogram bins in a normal 5-sec respiratory cycle (0.83 sec per frame). The simulated phantom matrix size was 512×512×231 with a voxel size of 1.03×1.03×0.69 mm^3. Spherical lesions undergoing respiratory motion were inserted at selected locations within the phantom lungs. The lesion locations were carefully selected and placed within the left and right lungs by sparing enough space to avoid streak artifacts from the reconstruction as well as the smearing effect from the nearby lesions in the non-gated study (see Figure 6). The corresponding attenuation-coefficient maps were generated, equivalent to the values obtained from a 4D high-resolution respiratory-gated CT scan. Figure 6(a) shows slices of the XCAT phantom simulated activity distributions with lesions, and Figure 6(b) and 6(c) show examples of simulated ^{18}F-FDG PET images reconstructed without and with gating, respectively. Lesion

smearing effect due to the respiratory motion is particularly visible in the non-gated images and low-count noise effect is shown in the gated images.

4.3.2 Monte Carlo Simulation

Monte Carlo simulations were used to generate the annihilation photons emitted from ^{18}F-FDG within the phantoms. The Monte Carlo simulation allows a validation of the proposed 4D approach in realistic conditions prior to the clinical validation. An advanced well-validated opensource software dedicated to numerical simulations in medical imaging GATE [110] was selected to model a commercially available Siemens Biograph mMR PET imaging system, consisting of 64 rings of 56 8×8 LSO crystal blocks with each crystal element of size 4×4×20 mm^3. For modeling emission-tomography detector geometries and physics phenomena, GATE basically inherited the Geant4 libraries and the layered architecture capability in defining complex scanner geometries and phantom descriptions through a macro mechanism configuration. In the GATE simulation, the phantom description was defined by taking account of the following files: 1) the 4D-XCAT phantom converted to 16-bit unsigned integer index images, 2) an activity range file assigning a specific ^{18}F-FDG activity level to each index in the voxelized phantoms, 3) an attenuation range file assigning a material (e.g., water, muscle) to each index, and 4) an internal header file describing the dimensions of the phantom. The simulations of the annihilation photons for anatomical background and for the lesions were separately processed through the modeling of the PET detectors. The simulated anatomical background without lesions were fused to the separately simulated lesions to form the lesion-present dataset, as illustrated in more detail in *Section 4.3.4* (Fused Sinograms). The simulated coincidences were stored in listmode files and then binned to michelograms with a

maximum ring difference of 60, azimuthal angle interleaving and span of 11 as used in the real scanner.

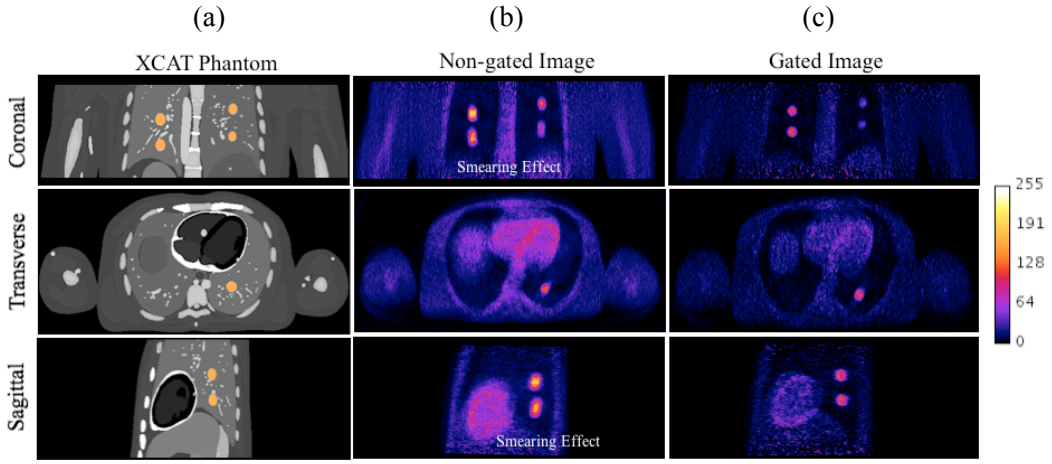

Figure 6 Examples of the phantom and simulated ^{18}F-FDG PET reconstructed images with lesions: (a) the XCAT phantom, (b) the non-gated image volumes, and (c) the respiratory-gated image volumes at the first gated frame (one gated frame) with the OSEM reconstruction in the coronal, transverse, and sagittal planes.

4.3.3 Noise Realizations

Due to the computational expense of Monte Carlo simulations in generating a large population of noise realizations, we used independent (Bernoulli) Thinning Poisson Point Process (TPPP) to generate the random Poisson distribution of the simulated sinograms for different noise realizations. Noise-free background sinograms were simulated using GATE. TPPP was then applied for randomly thinning certain classes of spatial point processes [112]. Let $\Im$ be the simulated counts generated. For every $x \in \Im$, let $1-\alpha(x)$, $0 \le \alpha(x) \le 1$ be the probability that a point located at x is removed, or culled, from any realization that contains it. For the realization $\xi = \left(n, \{x_1, \ldots, x_n\}\right)$, the point x_j is retained with probability $\alpha(x_j)$ and culled with probability 1-

$\alpha(x_j)$. The thinned realization is $\xi_\alpha = \left(m, \{x'_1, \ldots, x'_m\}\right)$, where $m \leq n$ is the number of points $\{x'_1, \ldots, x'_m\} \subset \{x_1, \ldots, x_n\}$ that pass the Bernoulli test. The probability that ξ_α has m points after thinning ξ is [113]

$$\Pr[m|n] = \binom{n}{m} \beta^m (1-\beta)^{n-m}, m \leq n. \quad (15)$$

The Bernoulli probability was selected to resample the noise-free sinograms to be an appropriate measured statistics for the realizations. The crucial statistical properties (i.e., mean and variance) of the thinned realizations remained those of the Poisson distribution. The Bernoulli probability can be altered to generate different statistical counts on sinograms for varying noise levels on the gated sinograms.

4.3.4 Fused Sinograms

Anatomical background and lesion sinograms were fused to integrate the background activities and the desired locations of the lesion activities. Fusion of the synthetic lesions and the anatomical background yielded realistic studies and was practically performed for the image quality assessment study, as shown in previous studies from our group [17, 18]. The separately simulated sinograms of N spherical lesions were added to the simulated clinical background sinograms yielding the lesion-present dataset. The lesion sinograms attenuated within the patient were scaled by a constant factor before forming the fused sinograms for obtaining the desired lesion-to-background contrasts. Noting that the lesion scatters were negligible when compared to the scatters in the anatomical background, Eq. (16) shows the fused sinogram, S_{fused}, combined from the anatomical background sinogram, S_B, and the lesion sinograms, S_i, with a scaling factor, k:

$$S_{fused} = \left(S_B + k\sum_{i=1}^{N} S_i \right) \cdot \exp\left(-\left(\Omega_B + \sum_{i=1}^{N} \Omega_i \right) \right), \quad (16)$$

where $S_x = \int_{-\infty}^{\infty} I_0(x,y)dL$ is the line integral of the emission source $I_0(x,y)$ and $\Omega_j = \int_{-\infty}^{\infty} \mu(x,y,511\ keV)dL$ is the line integral of the attenuation coefficients $\mu(x,y)$.

The S_{fused} sinogram was attenuated by the exponential of the line integrals of the attenuation coefficients among the background and the spheres, where the minus sign indicated the attenuation of the emission data. These fused data were equivalent to obtaining the realistic annihilation photons of the background and the tumors attenuated in the lungs and the surrounding tissues.

4.3.5 Image Reconstruction and Post filtering with 3D Gaussians

The simulated sinograms were reconstructed using a conventional ordered subset expectation maximization (OSEM) reconstruction. The 290×290×80 image volumes with an isotropic voxel size of 2 mm were obtained using OSEM with 6 subsets and 5 iterations. Attenuation correction and detector normalization sinograms were included in the reconstruction algorithm. Because only true coincidences were selected after the GATE simulation (randoms and scatters were included in the simulation), the corrections for randoms and scattered coincidences were not required in the reconstruction process.

4.3.6 Investigated Datasets

A total of 3,200 sub-image volumes over 50 noise realizations (2,400 gated, 400 non-gated, and 400 motion-corrected) in several conditions were used for the validation. The following three

datasets were examined: 1) the non-gated (3D-CH-NG), 2) the post-reconstruction motion-corrected (3D-CH-MC), and 3) the gated (4D-N-G) image volumes. Figure 7 shows examples of the simulated PET images with the corresponding respiratory motion and the experimental framework. The non-gated sub-window was centered at the non-gated centroid of each lesion, which was computed by averaging the center positions of each lesion over all the 6-gated positions. The motion-corrected sub-image was centered at each lesion back to the first gated frame. The motion-corrected images had less noise than the gated images due to the summed counts from the 6-gated images, and the gated images were much noisier. This motion correction method was equivalent to the outcome of image-based correction, which applied to the entire sequence images with perfect transformation back to a reference gate. The conventional 3D-CHO analysis was applied to the non-gated and motion-corrected sub-images to measure 3D SNR. In a similar fashion, the proposed 4D approach was applied to the dynamic gated sub-images for measuring 4D SNR. In our study, we used the training-testing option in which the observer was trained and tested on the same sets of images. Given the investigation by Wagner *et al.*, [114] they reported that using the single set of images to estimate the observer's template followed by an estimation procedure provided optimistic SNR results (re-substitution

(a)

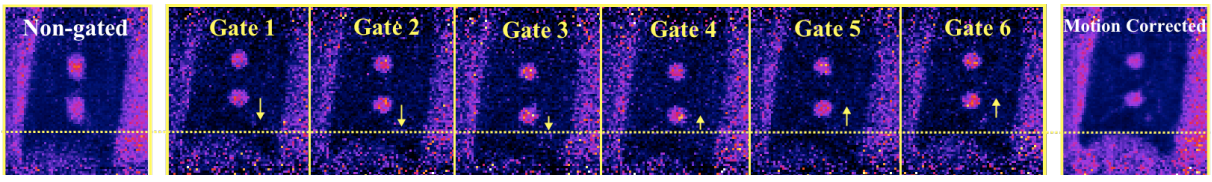

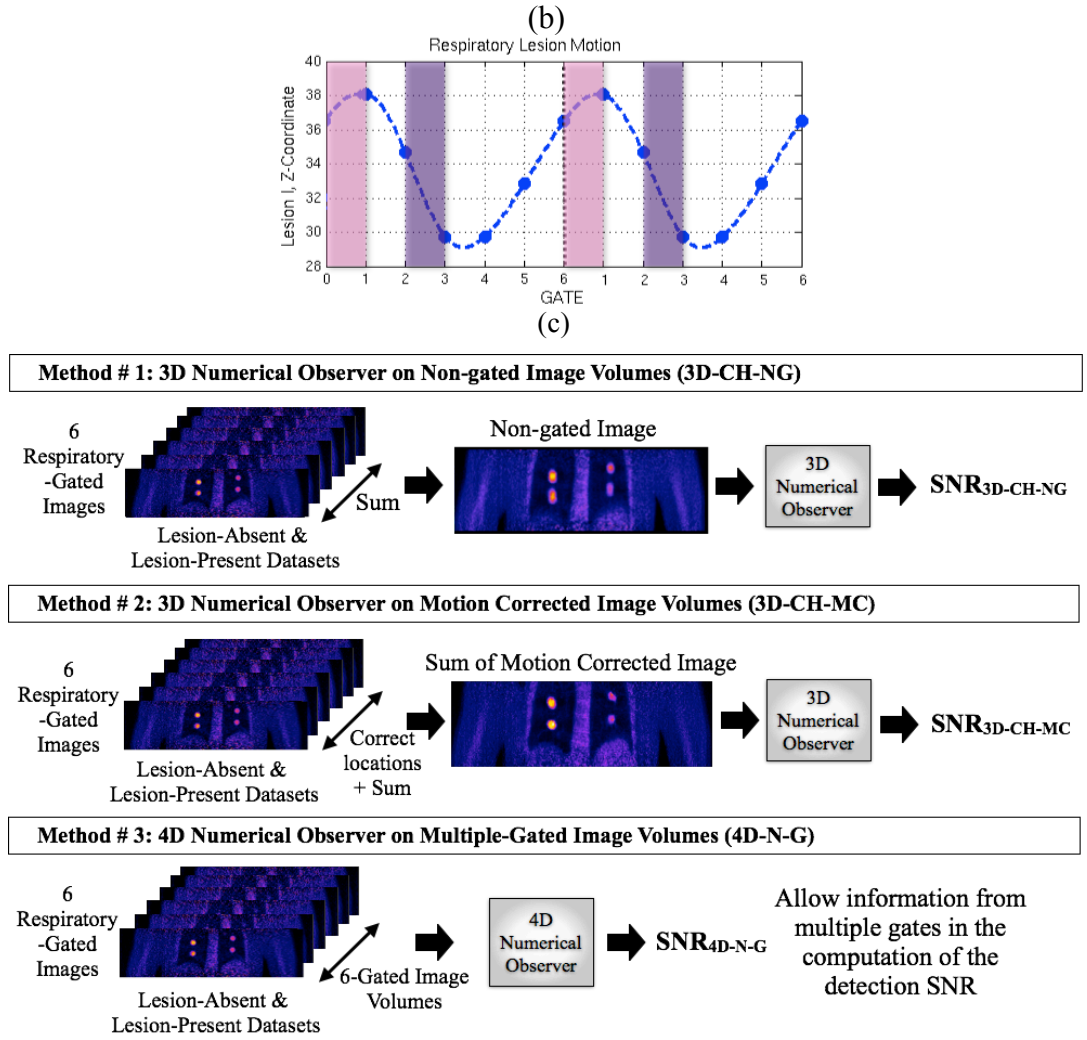

Figure 7 (a) Examples of non-gated, gated, and motion-corrected images without post-filtering, (b) an example of respiratory motion plot of a lesion, and (c) the experimental framework to examine the improvement of image quality in respiratory-gated PET images compared with three methods: 1) the non-gated (3D-CH-NG), 2) the post-reconstruction motion-corrected (3D-CH-MC), and 3) the multiple-gated (4D-N-G) images.

bias). The lesion contrast levels in the simulation (e.g., 3.5, 8.0, and 9.0) were selected to ensure that the lesion intensity is substantially higher than the background fluctuation.

A 5-channel 4D observer was applied to the multiple gated PET images whereas a 5-channel 3D-numerical observer (3D CHO) was applied to both the non-gated and motion-corrected PET images. A 9×9×9 sub-image volume centered at a given lesion location

was formulated to a column vector and was then input to the numerical observer as the lesion-present dataset. Likewise, the same size of the sub-image of the background region was used as the lesion-absent dataset. The 9×9×9 size of the sub-image volume was selected so that it was large enough to include the entire region of each lesion for all diameters, whereas the computational cost for the inversion of the covariance-matrix is still low. The larger sizes (e.g., 15×15×15) of the sub-image window provided the same SNR results.

4.4 Experimental Setup

The lesion detection validation was performed for the investigation of: 4.4.1) the performance comparison of 4D numerical observers, (*i.e., 4.4.1.1 Comparison between 4D and 3D Numerical Observers, 4.4.1.2. 4D Numerical Observer Constructed with Multi-Slice 2D Channels, 4.4.1.3. 4D Numerical Observer Constructed with Different 3D Channels, and 4.4.1.4. 4D Numerical Observer with Different Noise Levels*), 4.4.2) the impact of motion, 4.4.3) the impact of contrast levels, 4.4.4) the impact of lesion sizes, and 4.4.5) the impact of iteration and subset numbers. In all experiments, the channels of all observer models were constructed with 3D LG channels.

4.4.1 Performance Comparison of 4D Numerical Observers

4.4.1.1. Performance Comparison between 4D and 3D Numerical Observers

The author investigated the lesion detection performance of 4D-N-G in several lesion conditions and compared with the 3D-CH-NG and 3D-CH-MC methods. Eight lesions illustrated in Table 1 were inserted into the simulated anatomical sinograms with different simulated contrasts (C_s), lesion diameters (D), and amplitudes of lesion motion ($\left|\Delta\vec{r}\right|$).

Table 1 Characteristics of the eight inserted lung lesions

*Lesion	Diameter (D) (mm)	Simulated Contrast (C_s)	**Net Displacement ($\left\|\Delta\vec{r}\right\|$) (mm)
LLP-S1	16.0	8.0	30.5
ULP-S1	16.0	8.0	22.4
LRP-S1	16.0	3.5	29.3
URP-S1	16.0	3.5	17.6
LLA-S1	10.0	8.0	23.8
ULA-S1	10.0	8.0	23.3
LRA-S1	10.0	3.5	27.5
URA-S1	10.0	3.5	19.4

*LLP = lower left posterior, ULP = upper left posterior, LRP = lower right posterior, URP = upper right posterior, LLA = lower left anterior, ULA = upper left anterior, LRA = lower right anterior, and URA = upper right anterior.

**The net displacement was computed by summing the deformation from Gate 1 to Gate 6 to become a cumulative displacement of each lesion in a respiratory cycle.

The target-to-background contrast ratio of each lesion in the reconstructed images (C_r) was computed by determining the maximum reconstructed counts in the region of interest (ROI) centered in each lesion (R_{LP}) and the mean reconstructed counts in the corresponding ROI in the background images (R_{LA}). Then, C_r was computed[17] as: $(R_{LP}\text{-}R_{LA})/R_{LA}$ for each noise realization and each lesion. The reconstructed contrasts of the six-gated ($C_{r\text{-}G}$) and motion-corrected images ($C_{r\text{-}MC}$) over 50 noise realizations are shown in Table 2.

Table 2 Reconstructed contrasts of the six-gated and motion-corrected images.

Lesion	*$C_{r\text{-}G1}$	$C_{r\text{-}G2}$	$C_{r\text{-}G3}$	$C_{r\text{-}G4}$	$C_{r\text{-}G5}$	$C_{r\text{-}G6}$	**$C_{r\text{-}MC}$
LLP-S1	2.8 ± 0.2	3.0 ± 0.2	3.1 ± 0.2	2.7 ± 0.2	2.8 ± 0.2	2.8 ± 0.2	2.7 ± 0.1
ULP-S1	3.4 ± 0.3	3.9 ± 0.4	3.5 ± 0.2	3.9 ± 0.3	3.7 ± 0.2	3.8 ± 0.3	3.5 ± 0.1
LRP-S1	1.7 ± 0.1	1.7 ± 0.1	1.7 ± 0.1	1.7 ± 0.1	1.8 ± 1.0	1.6 ± 0.2	1.6 ± 0.1
URP-S1	1.9 ± 0.2	1.9 ± 0.2	2.2 ± 0.2	1.7 ± 0.1	1.9 ± 0.3	2.2 ± 0.3	1.8 ± 0.1
LLA-S1	2.8 ± 0.2	2.5 ± 0.2	2.6 ± 0.2	2.6 ± 0.2	2.8 ± 0.4	2.6 ± 0.3	2.5 ± 0.1
ULA-S1	2.6 ± 0.3	2.5 ± 0.3	2.2 ± 0.2	2.4 ± 0.3	2.4 ± 0.3	2.3 ± 0.2	2.2 ± 0.1
LRA-S1	1.2 ± 0.1	1.2 ± 0.1	1.1 ± 0.1	1.1 ± 0.1	1.1 ± 0.2	1.1 ± 0.2	1.0 ± 0.1
URA-S1	1.2 ± 0.2	1.2 ± 0.1	1.1 ± 0.1	1.1 ± 0.1	1.3 ± 0.2	1.3 ± 0.2	1.1 ± 0.1

*$C_{r\text{-}G}$ from Gate 1 to Gate 6 were computed over 50 noise realizations of each gate. **$C_{r\text{-}MC}$ was the reconstructed contrast of the motion corrected dataset over 50 noise realizations.

4.4.1.2. Performance of 4D Numerical Observer Constructed with Multi-Slice 2D Channels

The 'channelized structure' of the Channelized Hotelling observer in 2D and 3D was compared to assess the maximal performance of the observer. Besides the lesion conditions, the channel structure of the Channelized Hotelling observer tends to have an impact on lesion detectability of our two-layered numerical observer. Several studies [9, 100, 101] reported that using volumetric 3D channels in CHO yielded better performance than that using 2D-planar channels or 2D-stack channels (multi-slice 2D channels) in the image volume studies. To further investigate our 4D numerical observer, the two different channelized structures of 'multi-slice 2D-LG-channel' (MSL) and 'volumetric 3D-LG-channel' (VOL), constructed in the first layer of the 4D numerical observer, were demonstrated. Noting for the HO layer, the extended 'channelized processing' is not necessary due to the fact that the data dimensionality input to this processing step is quite small. For the multi-slice 2D-LG channels, Eq. (3) was transformed from the three-dimensional domain in $\Re^3$ to the two-dimensional domain in $\Re^2$. Then *x*-*y* planes of the 2D-LG functions were stacked to process on image slices in *z*-planes as a multi-slice model [9]. The eight lesions shown in Table 1 were used in this experiment.

4.4.1.3. Performance of 4D Numerical Observer Constructed with Different 3D Channels

The investigation of the proposed observer performance constructed with the channels that have ability to mimic human visual system was performed. The detection performance was compared using 4D-N-G constructed with 3D LG channels in Eq. (3) as '4D-N-G-LG' and one using

4D-N-G constructed with 3D D-DOG channels in Eq. (5) as '4D-N-G-DOG.' The eight lesions illustrated in Table 1 were used in this experiment.

4.4.1.4. Performance of 4D Numerical Observer with Different Noise Levels

The author observed the detection performance of the proposed 4D observer at different noise levels. To alter different noise levels embedded in sinograms, a new dataset with different levels of statistical counts on sinograms was simulated. We took advantage of Thinning Poisson Point Process by reducing the Bernoulli probability in Eq. (15) twice to diminish the statistical counts on sinograms approximately by half before resampling the noise-free sinograms. The new dataset was reconstructed to obtain lesions LLP-S1-H, ULP-S1-H, LRP-S1-H, URP-S1-H, LLA-S1-H, and ULA-S1-H. These lesion characteristics remained the same as illustrated in Table 1, but yielding higher noise levels. On the other hand, this experiment setup was equivalent to increasing the number of gated frames from 6 to 12 in the data acquisition. The reconstructed contrasts ($C_{r\text{-}G}$) of the noisy dataset of the six gates over 50 noise realizations are shown in Table 3, and they are similar to the contrasts in the previous dataset (*4.4.1.1*). Lesions LRA-S1 and URA-S1 were excluded from this high noise experiment because they are either too small size or too low contrast at this noise level.

Table 3 Reconstructed contrasts from Gate 1 to Gate 6 of the noisy lesions, simulated by reducing statistical counts on sinograms by half.

Lesion	$^{*}C_{r\text{-}G1}$	$C_{r\text{-}G2}$	$C_{r\text{-}G3}$	$C_{r\text{-}G4}$	$C_{r\text{-}G5}$	$C_{r\text{-}G6}$
LLP-S1-H	2.8 ± 0.3	3.0 ± 0.3	3.1 ± 0.3	2.8 ± 0.2	2.9 ± 0.3	2.9 ± 0.3
ULP-S1-H	3.4 ± 0.5	4.0 ± 0.6	3.6 ± 0.4	4.0 ± 0.4	3.8 ± 0.5	3.9 ± 0.4
LRP-S1-H	1.7 ± 0.2	1.8 ± 0.2	1.8 ± 0.2	1.7 ± 0.2	1.7 ± 0.2	1.6 ± 0.2
URP-S1-H	2.1 ± 0.3	1.9 ± 0.2	2.2 ± 0.4	1.8 ± 0.3	1.9 ± 0.3	2.2 ± 0.4
LLA-S1-H	2.8 ± 0.4	2.6 ± 0.2	2.6 ± 0.2	2.7 ± 0.3	2.9 ± 0.3	2.7 ± 0.3
ULA-S1-H	2.5 ± 0.3	2.5 ± 0.3	2.3 ± 0.4	2.3 ± 0.3	2.3 ± 0.3	2.4 ± 0.4

$^{*}C_{r\text{-}G}$ from Gate 1 to Gate 6 were computed over 50 noise realizations of each gate.

4.4.2 Impact of Motion on Lesion Detection

Because the non-gated signal at higher motion has more smearing effect than that at lower motion, when the motion has been removed, we should obtain more Gain ($SNR_{Observed}$ / $SNR_{3D\text{-}CH\text{-}NG}$) at higher motion than that at lower motion. In this experiment, we compared the performance of the detection task for lesions with different motion amplitudes. The motion variation was set by placing the lesions at different locations in the lung lobes, where the base (near the live dome) had higher motion and the apex of the lung had lower motion. The lesion diameter and the simulated contrast level were fixed. The lesion diameter was 13.0 mm and the simulated contrast applied to all lesions was consistently set to 9.0 in the activity simulation. A dedicated filter smoothed the reconstructed images prior to the image quality measurement in order to smooth the lesion profiles on the reconstructed images. The 3D Gaussian filter with full width at half maximum (FWHM) of 1.77 was applied equally to all tested reconstructed image volumes. Four lesions at the different $|\Delta\vec{r}|$ and C_r are described in Table 4. In this experiment and herein, all numerical observers were constructed with volumetric 3D-LG channels.

Table 4 Contrasts and displacements in millimeter of the four 13-mm lesions from Gate 1 to Gate 6 in a respiratory cycle.

Data	Lesion	D (mm)	C_s	C_r	Gate 1-2 (mm)	Gate 2-3 (mm)	Gate 3-4 (mm)	Gate 4-5 (mm)	Gate 5-6 (mm)	$\lvert\Delta\vec{r}\rvert$ (mm)
Set #1	LLP-S2	13.0	9.0	2.2 ± 0.0	7.0	10.2	0.1	6.5	7.5	31.3
	LRP-S2	13.0	9.0	2.2 ± 0.0	6.6	9.1	0.4	6.1	6.6	27.0
Set #2	LLA-S2	13.0	9.0	2.3 ± 0.0	5.8	8.9	0.3	5.6	6.4	28.5
	LRA-S2	13.0	9.0	2.3 ± 0.0	6.1	9.0	0.7	5.6	6.8	27.9

*C_r was computed on the motion corrected dataset.

4.4.3 Impact of Contrast on Lesion Detection

This experiment was performed to confirm whether our 4D numerical observer computed detection SNRs relied on a linearity property of an optimal-linear observer for changes of lesion contrast while the motion was present. In this study, we expected that detection SNRs of the 4D method increased linearly with the increased lesion contrast. The author simulated four 13-mm lesions in two lesion-contrast levels: low (C_s = 9.0) and high (C_s = 20.0) with the different $|\Delta\vec{r}|$ of motion that described in Table 4. The detection SNRs and gains of low and high contrasts of 3D-CH-NG and 4D-CH-G were measured and analyzed.

4.4.4 Impact of Lesion Size on Lesion Detection

Similarly, a linearity property of lesion sizes when the motion was present was examined. We used four lesions of two diameters (10.0 mm and 13.0 mm) with different motion $|\Delta\vec{r}|$ that described in Table 4. All of these four lesions were consistently simulated with a contrast level (C_s) of 9.0.

4.4.5 Impact of the Number of Iterations and Subsets in Image Reconstruction

The investigation of the detection performance as a function of iteration and subset numbers in the iterative reconstruction was performed. Four lesions with the characteristics illustrated in Table 4 were reconstructed from 1 to 20 iterations for 6 and 12 subsets. The cost function of Log-likelihood and the root-mean-square-error (RMSE) of the difference between the reference XCAT phantom and simulated PET image were computed.

4.5 Results

4.5.1 Performance Comparison of 4D Numerical Observers

4.5.1.1. Performance of 4D Numerical Observer Constructed with Volumetric 3D Channels

Figure 8 shows lesion detection SNRs of 3D-CH-NG, 3D-CH-MC, and 4D-N-G for the eight lesions described in Table 1. On average, 4D-N-G improves detection SNR by 48.6% ($p < 0.005$), whereas 3D-CH-MC improves by 31.0% ($p < 0.005$) as compared to 3D-CH-NG, respectively. The relative SNR measurement (Gain = $SNR_{Observed}$ / $SNR_{3D\text{-}CH\text{-}NG}$) of lesion detection obtained from 4D-N-G was significantly higher than from 3D-CH-MC by 13.8% ($p < 0.02$), where $Gain_{4D\text{-}N\text{-}G}$ was 1.49 ± 0.21 and $Gain_{3D\text{-}CH\text{-}MC}$ was 1.31 ± 0.15. Of the eight lesions, lesion LLP-S1 (lower left posterior) with the highest motion provided the highest improvement (176.0%) using the 4D-N-G method. More interestingly, as shown in Figure 8(b), at lesion URP-S1, the greater $Gain_{4D\text{-}N\text{-}G}$ (1.21) in lesion detectability was achieved for the lesion with the smallest lesion motion ($|\Delta\vec{r}|$ = 17.6 mm), whereas it did not obtain the same benefit from the 3D numerical observer ($Gain_{3D\text{-}CH\text{-}MC}$ = 1.10). This observation indicates that at fairly low-level motion, the 4D numerical observer provided higher performance in lesion detectability than did the 3D numerical observer.

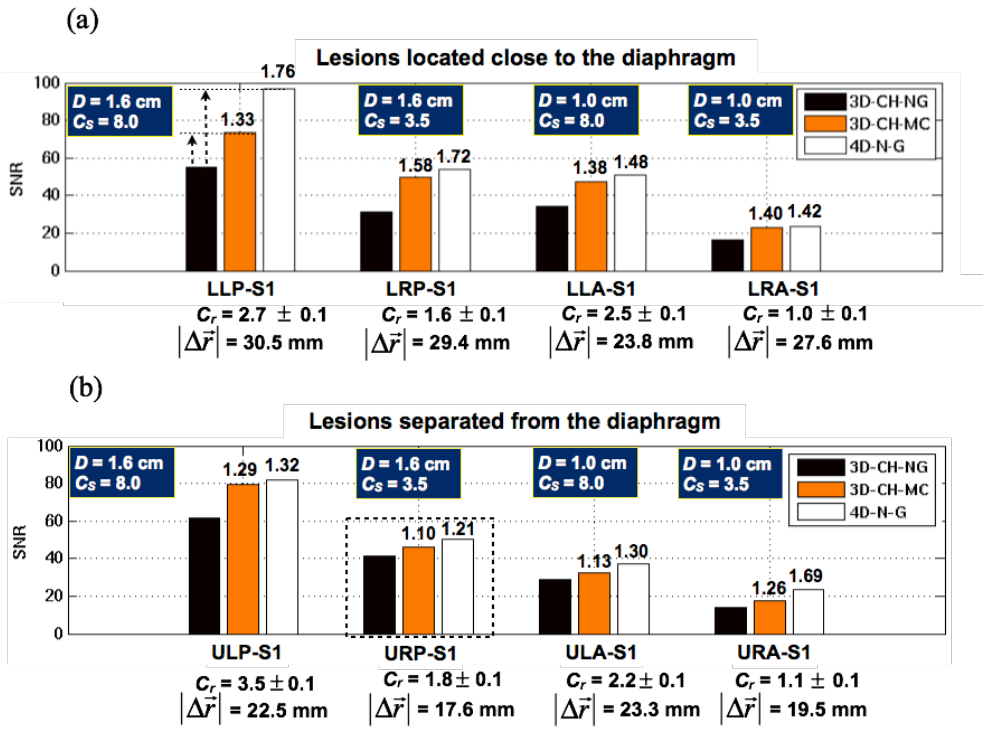

Figure 8 Detection SNRs for 3D-CH-NG, 3D-CH-MC, and 4D-N-G: (a) the lesions (LLP-S1, LRP-S1, LLA-S1, and LRA-S1) located close to the diaphragm and (b) the lesions (ULP-S1, URP-S1, ULA-S1, and URA-S1) separated from the diaphragm, where the dotted box shows the greater $\text{Gain}_{\text{4D-N-G}}$ achieved for the lesion with the smallest motion whereas it does not obtain the same benefit from 3D-CH-MC. C_r was computed on the motion corrected dataset. The arrows for the LLP-S1 lesion show the gains obtained relative to the non-gated SNR.

As shown in Figure 8, the comparison of the four lesions located close to the diaphragm (LLP-S1, LRP-S1, LLA-S1, and LRA-S1) and four lesions separated from the diaphragm (ULP-S1, URP-S1, ULA-S1, and URA-S1) shows that lesion detection SNRs are sensitive to the contrast levels, lesion sizes, and the amplitudes of motion. One important observation was that the slight changes of each condition influenced the lesion detectability of the numerical observer measurement. The lesions with higher motions (LLP-S1, LRP-S1, LLA-S1) had higher gains than that with lower motions (ULP-S1, URP-S1, ULA-S1) for both 3D-CH-MC and 4D-N-G,

except lesions LRA-S1 and URA-S1. Lesion URA-S1 with less motion ($|\Delta\vec{r}|$ = 19.5 mm) achieved higher gain from the 4D lesion detection task ($Gain_{4D\text{-}N\text{-}G}$ = 1.69) than did lesion LRA-S1 ($Gain_{4D\text{-}N\text{-}G}$ = 1.42) with higher motion ($|\Delta\vec{r}|$ = 27.6 mm). This was because lesions URA-S1 and LRA-S1 were both small and had low reconstructed target-to-background contrast ratios (C_r was 1.0 ± 0.1 and 1.1 ± 0.1, respectively). This illustrated that the variation of the conditions of lesions (i.e., motion, contrast level, diameter) affected the numerical observer detectability.

4.5.1.2. Performance of 4D Numerical Observer Constructed with Multi-Slice 2D Channels

Figure 9 shows 4D-N-G using volumetric 3D-LG-channel (4D-N-G-VOL) yields 15.2% (p < 0.01) higher detection SNR than 4D-N-G using multi-slice 2D-LG-channel (4D-N-G-MSL) for all lesions described in Table 1. The relative SNR measurement of lesion detection using 4D-N-G-VOL was significantly higher than that using 4D-N-G-MSL (p < 0.01), where $Gain_{4D\text{-}N\text{-}G\text{-}VOL}$ was 1.50 ± 0.21 and $Gain_{4D\text{-}N\text{-}G\text{-}MSL}$ was 1.30 ± 0.18.

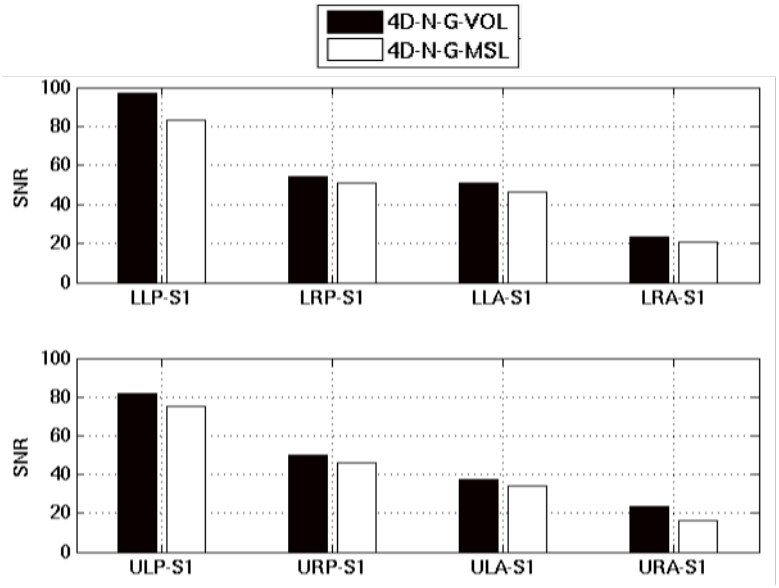

Figure 9 The comparison of SNRs evaluated between 4D-N-G with volumetric 3D-LG-channel (4D-N-G-VOL) and 4D-N-G with multi-slice 2D-LG-channel (4D-N-G-MSL).

4.5.1.3. Performance of 4D Numerical Observer Constructed with Different 3D Channels

Table 5 shows the detection SNR and the relative SNR measurement using 4D-N-G-LG and 4D-N-G-DOG. Comparing the detection SNR and $Gain_{4D\text{-}N\text{-}G}$, there is no significant difference ($p < 0.01$) between 4D-N-G-LG and 4D-N-G-DOG in detecting uniform and spherical lesions.

Table 5 The detection SNRs obtained using 4D-N-G-LG and 4D-N-G-DOG

Method	LLP-S1	LRP-S1	LLA-S1	LRA-S1	ULP-S1	URP-S1	ULA-S1	URA-S1
4D-N-G-LG	97.84	54.60	51.32	23.73	82.53	50.60	37.84	24.03
$Gain_{4D\text{-}N\text{-}G\text{-}LG}$	1.76	1.72	1.48	1.42	1.32	1.21	1.30	1.69
4D-N-G-DOG	94.04	55.87	52.45	24.14	76.68	50.59	37.81	19.79
$Gain_{4D\text{-}N\text{-}G\text{-}DOG}$	1.59	1.69	1.45	1.38	1.23	1.21	1.16	1.55

4.5.1.4. Performance of 4D Numerical Observer with Different Noise Levels

Table 6 shows the detection SNRs of the normal noise level (*Section 4.4.1.1*) and high noise level datasets for the lesions located close to the diaphragm (LLP-S1, LRP-S1, and LLA-S1) and the lesions separated from the diaphragm (ULP-S1, URP-S1, and ULA-S1). When compared to the dataset in *4.4.1.1* with the normal noise level, we found that the detection SNRs computed from the noisy datasets reduced by 27.6% and 41.5% for 3D-CH-NG and 4D-N-G, respectively. As shown in Table 6, the relative SNRs maintain the similar characteristic to the results in *4.4.1.1*, as $Gain_{4D\text{-}N\text{-}G}$, for the lesions with higher motion (LLP-S1, LRP-S1, and LLA-S1) are more than that the lesions with lower motion (ULP-S1, URP-S1, and ULA-S1), respectively.

Table 6 The detection SNRs using 3D-CH-NG, 4D-N-G, and the relative SNR ($Gain_{4D\text{-}N\text{-}G}$) compared between the normal noise level (*Section 4.4.1.1*) and noisy level datasets.

Noise Level*	Method	Higher Motion			Lower Motion		
		LLP-S1	LRP-S1	LLA-S1	ULP-S1	URP-S1	ULA-S1
Normal	3D-CH-NG	55.03	31.44	34.43	61.69	41.48	28.80
	4D-N-G	96.86	54.05	50.81	81.70	50.09	37.46
	$Gain_{4D\text{-}N\text{-}G}$	**1.76**	**1.72**	**1.48**	**1.32**	**1.21**	**1.30**
Noisy	3D-CH-NG	35.96	23.33	18.57	42.03	18.35	22.18
	4D-N-G	50.20	32.82	26.00	52.14	24.57	29.16
	$Gain_{4D\text{-}N\text{-}G}$	**1.40**	**1.41**	**1.40**	**1.24**	**1.34**	**1.31**

*The 'normal noise' level referred to the normal dataset with a certain statistical counts used in this project and the 'noisy' level referred the noisy dataset generated using half statistical counts of the normal dataset.

4.5.2 Impact of Motion on Lesion Detection

Lesions LLP-S2 and LLA-S2 are two 13-mm lesions with higher motions at two different locations and different contrasts in datasets #1 and #2, respectively. Figure 10 shows that LLP-S2 and LLA-S2 with larger motions ($|\Delta\vec{r}|$ = 31.3 mm and 28.5 mm) have higher gains of

4D-N-G (1.71 and 1.39) than that of LRP-S2 and LRA-S2 with smaller motion (1.65 and 1.30). On the contrary, it did not confirm this benefit using 3D-CH-MC, as shown for lesions LLP-S2 ($Gain_{3D\text{-}CH\text{-}MC}$ = 1.56) and LRP-S2 ($Gain_{3D\text{-}CH\text{-}MC}$ = 1.62). As can be seen in Table 7, when comparing the higher-motion to the lower-motion lesions, we obtained greater $Gain_{4D\text{-}N\text{-}G}$ than did $Gain_{3D\text{-}CH\text{-}MC}$ ($p < 0.03$).

4.5.3 Impact of Contrast on Lesion Detection

As illustrated in the regression plot in Figure 11(a), SNR-Change-Rate (SNR-CR = $(SNR_{high}\text{-}SNR_{low})/SNR_{low}$) between 4D-N-G and 3D-CH-NG shows a linear relationship when the lesion contrast levels increased. Figure 11(b) shows that the $Gain_{4D\text{-}N\text{-}G}$ between the low and high contrasts has a linear relationship. There is no significant difference ($p < 0.07$) of $Gain_{4D\text{-}N\text{-}G}$ between the low and high contrast levels. This finding indicated that when the lesion contrast level changed, the lesion detectability estimated by the proposed 4D numerical observer linearly changed while the motion was present.

4.5.4 Impact of Lesion Size on Lesion Detection

As illustrated in Figure 12(a), SNR-CR between 4D-N-G and 3D-CH-NG linearly increased with the increased lesion diameters. Figure 12(b) shows that $Gain_{4D\text{-}N\text{-}G}$ measured at two different lesion diameters have a linear relationship and have no significantly difference (r = 0.99). This finding reported that the lesion detection computed by the proposed 4D numerical observer varied linearly with changes of the lesion diameters while the motion was present. More interestingly, in Figure 11(a) and Figure 12(a), it can be seen that SNR-CR of the lesion-diameter variation (slope = 0.73) is slower than SNR-CR of the lesion-contrast variation (slope = 1.10) by

50.7%. This finding indicated that the changing of the lesion contrast altered SNR faster than the changing of the lesion diameter.

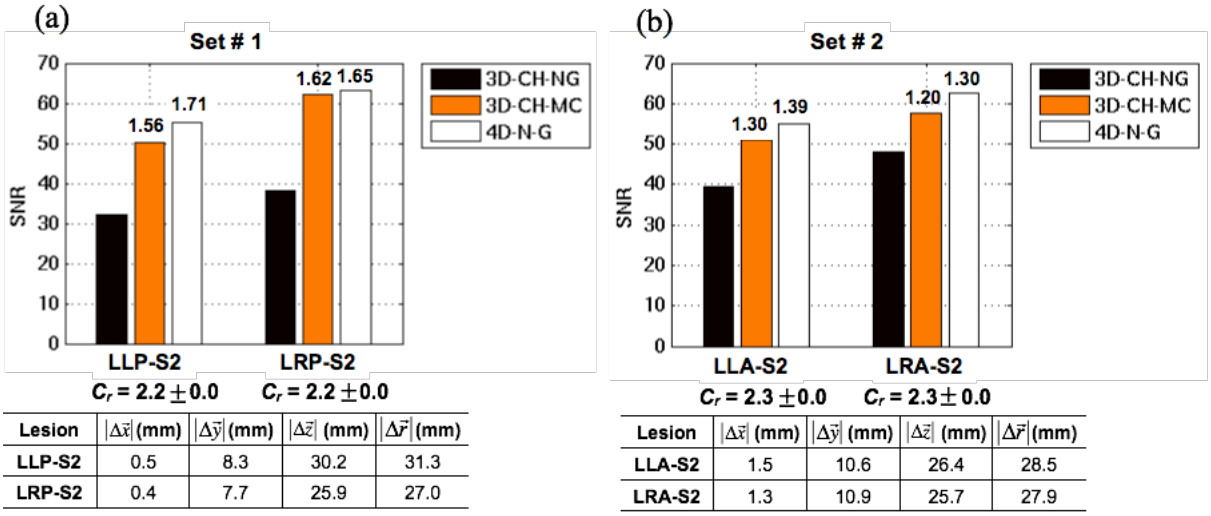

Lesion	$\lvert\Delta\vec{x}\rvert$ (mm)	$\lvert\Delta\vec{y}\rvert$ (mm)	$\lvert\Delta\vec{z}\rvert$ (mm)	$\lvert\Delta\vec{r}\rvert$ (mm)
LLP-S2	0.5	8.3	30.2	31.3
LRP-S2	0.4	7.7	25.9	27.0

Lesion	$\lvert\Delta\vec{x}\rvert$ (mm)	$\lvert\Delta\vec{y}\rvert$ (mm)	$\lvert\Delta\vec{z}\rvert$ (mm)	$\lvert\Delta\vec{r}\rvert$ (mm)
LLA-S2	1.5	10.6	26.4	28.5
LRA-S2	1.3	10.9	25.7	27.9

Figure 10 The SNR comparison of 3D-CH-NG, 3D-CH-MC, and 4D-N-G with varying motion displacements at the same contrasts for (a) LLP-S2 and LRP-S2 with $\lvert\Delta\vec{r}\rvert$ of 31.3 mm and 27.0 mm, respectively and (b) LLA-S2 and LRA-S2 with $\lvert\Delta\vec{r}\rvert$ of 28.5 mm and 27.9 mm, respectively. The detail of the net displacements ($\lvert\Delta\vec{x}\rvert$, $\lvert\Delta\vec{y}\rvert$, and $\lvert\Delta\vec{z}\rvert$) in the *x*, *y*, and *z* directions are shown the tables below (a) and (b). C_r was computed on the motion corrected dataset.

Table 7 Summary of the SNR gains computed using 4D-N-G and 3D-CH-MC.

*Motion	$Gain_{4D\text{-}N\text{-}G}$		$Gain_{3D\text{-}CH\text{-}MC}$	
	Set #1	Set #2	Set #1	Set #2
Higher	1.71	1.39	1.56	1.30
Lower	1.65	1.30	1.62	1.20

*The lesions were placed at different locations for varying different motions described in Table 2.

(a) (b)

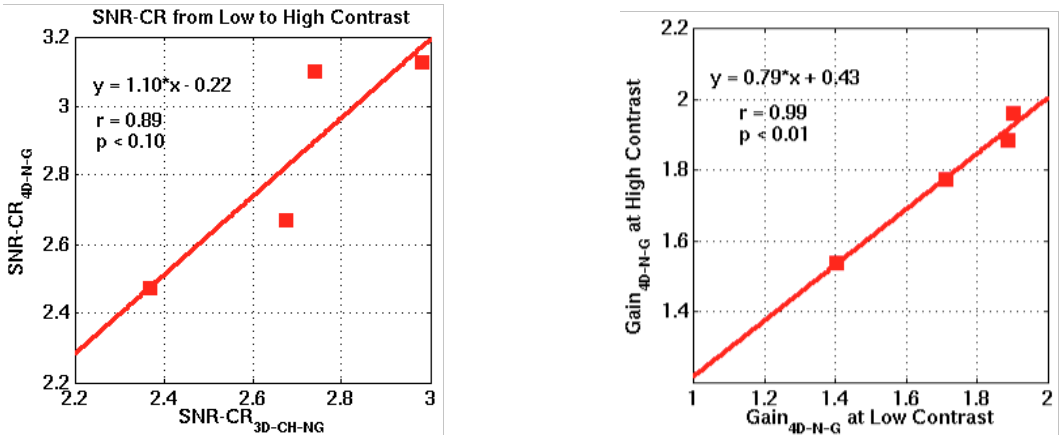

Figure 11 (a) The regression plot of SNR-Change-Rate (SNR-CR) from low (9.0) to high (20.0) contrast levels for 3D-CH-NG and 4D-N-G and (b) the regression plot of the $Gain_{4D\text{-}N\text{-}G}$ between high contrast and low contrast datasets.

(a) (b)

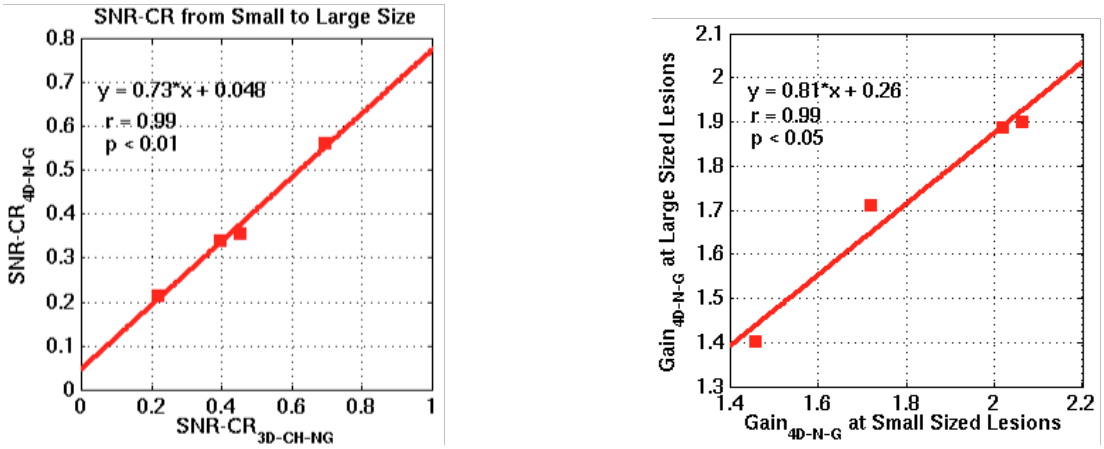

Figure 12 (a) The regression plot of the SNR-CR from small (D = 10.0 mm) to large (D = 13.0 mm) lesion diameter for 3D-CH-NG and 4D-N-G and (b) the regression plot of $Gain_{4D\text{-}N\text{-}G}$ between the large and small lesions.

4.5.5 Impact of the Number of Iterations and Subsets in Image Reconstruction

Using the OSEM algorithm, the Log-Likelihood continuously decreases with the increasing iteration number, while the reconstructed images after certain iterations become much noisier. Consequently, the RMSE of the image difference becomes larger. Figure 13(a) shows the Log-Likelihood plots as a function of iteration numbers for 6 and 12 subsets. As shown, the PET reconstruction with 6 subsets yields higher Log-Likelihood than that with 12 subsets. Figure 13(b) shows the RMSE plots of the difference between the reference phantom and PET image versus iteration numbers for 6 and 12 subsets. For all the iteration numbers, the PET reconstruction with 6 subsets yields better RMSE than of 12 subsets. With 6 subsets, it provides the minimal RMSE at iteration #3, whereas the reconstruction with 12 subsets achieves the minimal RMSE at the end of iteration #1. As illustrated in Table 8, the detection SNRs of 4D-N-G (i.e., lesions LLP-S2, LLA-S2, LRP-S2, and LRA-S2) were computed using the selected iteration number corresponding to the minimal RMSE for each subset number. For all the lesions, the lesion-detection performance of 6 subsets is slightly higher than that of 12 subsets by 4.9%, similar to the findings reported by Morey *et al*., 2013 [115]. Table 9 shows the detection SNRs of 4D-N-G of the reconstructed images using 30, 40, and 50 iterations with 12 subsets followed by 3D-Gaussian post filtering (FWHM = 5.9 mm). These findings indicated that the iteration and subset numbers had impact on the lesion detectability and the selection of the optimal parameters could provide the maximum lesion-detection performance.

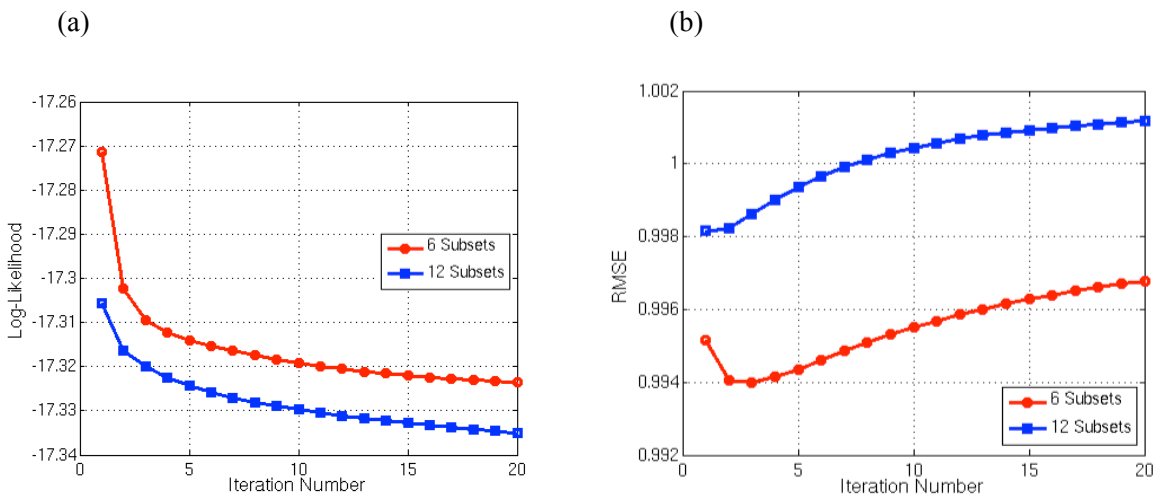

Figure 13 (a) The Log-Likelihood plots as a function of iteration numbers for 6 and 12 subsets and (2) the root-mean-square-error (RMSE) plots as a function of iteration numbers for 6 and 12 subsets.

Table 8 The detection SNRs of 4D-N-G computed using the iteration numbers which yielded the minimal RMSEs for 6 and 12 subsets.

Lesion	Subset Number	
	6	12
LLP-S2	82.42	81.80
LRP-S2	107.28	100.52
LLA-S2	105.52	97.22
LRA-S2	119.00	113.22

Table 9 The detection SNRs of 4D-N-G of the reconstructed images with 3D-Gaussian post filtering (FWHM = 5.9 mm) for 12 subsets.

Iteration No.	LLP-S2	LRP-S2	LLA-S2	LRA-S2
30	61.25	79.23	73.98	85.70
40	61.07	78.37	73.44	78.53
50	60.98	77.93	73.14	78.31

4.6 Discussion

Our proposed 4D approach yields higher detection SNRs than that from the 3D method on motion-corrected images because the 4D method avoids potential errors occurring in the motion correction method. The major factors that may contribute to the errors on motion-corrected images are registration and interpolation inaccuracies [21, 83]. These effects lead to lower contrast recovery as well as spatial-resolution degradation on the motion-corrected images. In this study, we used the same motion fields both to create the simulations and to correct for motion, thus registration errors may only have a limited impact. Therefore, the interpolation inaccuracy introducing during the transformation procedure mainly contributes to the errors in the motion-corrected images.

As illustrated in Table 2, the motion-corrected images have lower contrast recovery ($C_{r\text{-}MC}$) as compared to the gated images ($C_{r\text{-}G1}$ to $C_{r\text{-}G6}$). This was also observed in the study performed by Detorie and colleagues [21] which was shown that post-reconstruction motion-corrected images had diminishing signal contrast recovery and degrading spatial resolution as compared to gated images. Similarly, several studies [83, 116-118] reported that the image-based correction (post-reconstruction motion correction) method has higher bias than does the gated method. Polycarpou *et al.* [83] mention that the non-linearity characteristics of OSEM is one major cause of the bias occurring in post-reconstruction motion-corrected images.

Barrett *et al.* [119] and Wilson *et al.* [120] suggest that the non-linear EM algorithm influences the noise properties and the behavior of the variance/covariance of the noise, in which it may have an impact on the figures of merit for image quality assessment. In the 3D approach, the nearly motion-free independently reconstructed gated images are summed to account for all

measured data in order to improve the SNR [83], [121]. Nevertheless, the summation of multiple non-linear reconstructed images of the motion correction method does not satisfy the superposition principle. As a result, the noise properties in post-reconstruction motion-corrected images may not preserve, which it does not guarantee superior lesion detectability.

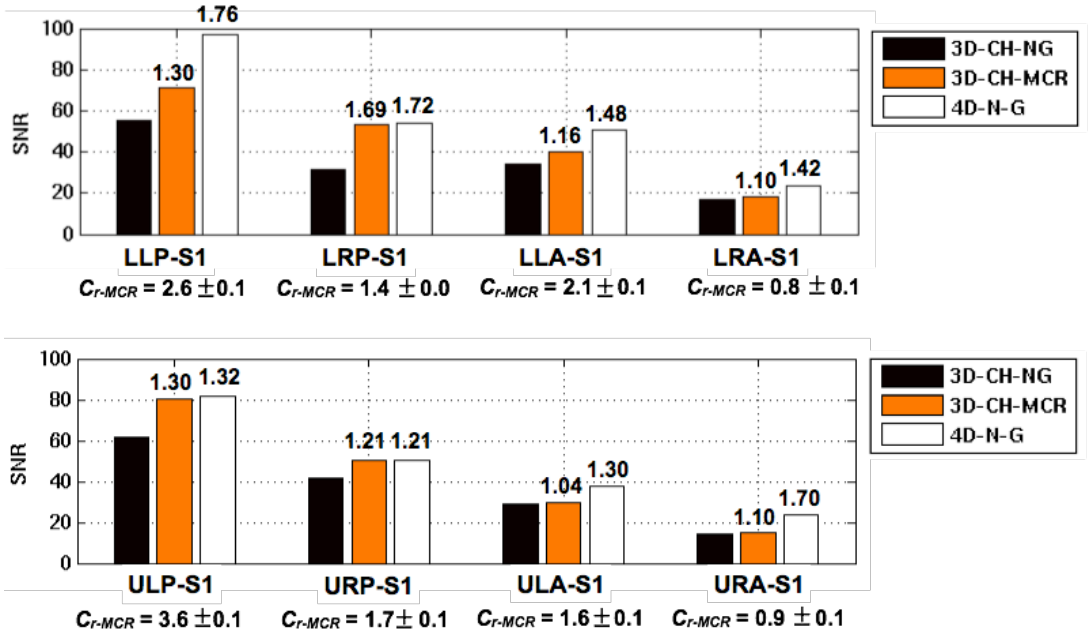

Figure 14 The SNR comparison of 4D-N-G applied to multiple gated-image volumes and 3D-CH-MCR measured on the image volumes obtained using the reconstruction-based correction or the motion-compensation iterative reconstruction. The motion-compensation reconstruction was processed using 6 subsets and 5 iterations and was applied to the same dataset in *Section 4.1.1*. $C_{r\text{-}MCR}$ was the reconstructed contrast on the motion-compensation-reconstructed images over 50 noise realizations.

Although the different motion correction method using the reconstruction-based correction [23, 118, 122, 123] provides higher overall performance compared to the aforementioned image-based correction method [83], the lesion detectability using 3D CHO on the resulting images remains inferior to the 4D approach. We preliminarily compared 4D-N-G to the 3D-CHO

analysis applied to the motion-corrected images using a motion-compensated iterative OSEM reconstruction [23] (3D-CH-MCR). As can be seen in Figure 14, the lesion detection performance of 4D-N-G is significantly higher than that of 3D-CH-MCR by 22.0% ($p < 0.04$). Even though 3D-CH-MCR incorporates motion fields during the iterative reconstruction process for reducing the noise characteristics error, limited signal contrast recovery remains the issue. The interpolation error during the motion-compensated iterative reconstruction remains the cause contributing to the motion corrected images obtained by using MCR [118]. These observations provide evidence for the need for using 4D analysis in image quality assessment in respiratory-gated PET. On the other hand, the 4D numerical-observer approach may be used as an upper bound to investigate the performance of the motion correction method. As a result, using the 4D observer approach that appropriately integrates information from multiple gates maximizes the performance of the observer.

Because of the smearing effect, we expect higher $\text{Gain}_{\text{4D-N-G}}$ for the lesion with higher motion when comparing to one with lower motion. As shown in Figure 8, the $\text{Gains}_{\text{4D-N-G}}$ of all lesions undergo this characteristic, except lesions LRA-S1 and URA-S1. This inconsistency is related to the improper contrast level and lesion diameter in the experiment setup. It is not related to the unreliability of the observer detection. As illustrated in Table 2, $C_{r\text{-}G1}$ to $C_{r\text{-}G6}$ for lesion URA-S1 depict greater contrast recovery than those of lesion LRA-S1, whereas the motion-corrected images for lesions LRA-S1 and URA-S1 have almost similar reconstructed contrasts values ($C_{r\text{-}MC}$). Hence, the 4D-SNR value of lesion URA-S1 is dominated by higher reconstructed contrast values. As a result, $\text{Gain}_{\text{4D-N-G}}$ of URA-S1 with smaller motion was higher than of LRA-S1 with larger amplitude motion. Due to the fact that lesions LRA-S1 and URA-S1 were simulated with a relatively small size (D = 10.0 mm) and low contrast (C_s = 3.5), these

lesion diameter and contrast might be too low to tolerate against the random fluctuations of statistical noise in the anatomical background. This affects the signal applied to the SNR computation. On the other hand, the reconstructed contrasts of the two lesions should have been the same if we would focus only on the influence of motion. Therefore, the proper contrast (C_s = 9.0) and lesion diameter (13.0 mm) in the experiment in *Section 4.4.2* were performed to investigate the impact of motion amplitudes. The gains of the detection SNRs obtained from the 4D method were promising corresponding to the motion influence as shown in the results of *Section 4.4.2*.

The advantage of the proposed method is that it takes into account the shape deformation of the target signals. The non-rigid registration applied to a target with shape deformation may contribute errors for motion correction. These errors may cause inferior to lesion detection when analyzing with 3D-CH-MC, especially in PET images. In contrast, 4D-N-G incorporates the possible deformation of the lesions along the temporal gated volumes. Within each gated volume, the 3D CHO in the spatial processing step provides the degree to which the lesion signal is present in each gate separately. The HO in the temporal processing step integrates the consecutive lesion signal information and includes the lesion deformation that may occur among the gated frames.

For application to other asymmetric organs, Platisa *et al*., [9] suggested that the channels of the numerical observer can be altered for more appropriate analysis of asymmetric targets. The LG channels are adequate for a spherically symmetric signal and for comparing performance among the observer models. A difference-of-Gaussians configuration might be used to model channel profiles close to the human visual system. Nevertheless, we focus on a new method for

an image quality assessment of 4D data (3D+time) and the target shape deformation is not yet reported in this study.

It is indeed possible that there might be residual intra-gate motion blurring if respiratory gating is performed using a small number of gates [74, 75]. This effect can cause blurring/smearing and cause the shape of reconstructed signals to be more elliptical than spherical. With this lesion deformation, one can use an asymmetric channel model of oriented channels, such as rotationally oriented (RO) channels (LaCroix *et al*., 2000 [124] and Wollenweber *et al*., 1999 [125]) or steerable channels (Goossens *et al*., 2010 [126]), to detect the orientation of signals or the background structure in an image. By detecting the orientation of signals, one can identify the residual motion pertinent to the target lesions along known (unknown) directions. In the future study, we will investigate the impact of asymmetrical channels using our new acquired clinical PET/CT data, where the number of gates is limited by the radiation dose to the patients.

It is questionable whether the performance of 4D-N-G can be further improved if we increase the number of gated frames. However, Lalush *et al*. [127] showed that increasing the number of gated frames from 8 to 16 did not offer a significant advantage for a myocardial defect detection task in a gated-myocardial perfusion SPECT study. Thus, increasing the number of gated frames might only slightly improve the detection performance in our respiratory-gated PET detection task. Furthermore, even though humans can use information about the temporal shape of the signal, they cannot do it optimally as they perform some suboptimal matched filtering through time [107]. Humans have a limited ability to integrate the signal over the entire temporal duration because of suboptimal temporal-sampling efficiency, referring to the inability of observer to match the temporal profile perfectly [107]. Our further study may include

temporal processing of the human visual system and compare the performance of numerical observer to human observer.

4.7 Chapter Summary

The chapter has demonstrated improvement in lesion detectability when applying the 4D numerical observer on cine volumetric gated images. The 4D observer yields higher performance than using a 3D numerical observer on the motion-corrected images either from the image-based correction or the reconstruction-based correction method. Our algorithm was applied to simulated PET data with known inserted lesions in several conditions, and showed an increase in the detection signal-to-noise ratio, especially for the lesions with low motion, in which analysis was difficult using the conventional 3D method. The proposed 4D approach yielded a rigorous and objective evaluation of the gain that was expected from respiratory-gated PET imaging. Human observers using ROC analysis methodology may be proposed to perform the same task and compare the human observer performance to the detection performance using our 4D method. Our findings may be applied in other applications such as in different image modalities e.g., PET/MR, spectral CT, and parametric PET imaging in order to enhance the objective evaluation. Future work will involve the validation in lesion detectability using the 4D numerical observer in clinical data to ensure an appropriate objective assessment of the expected improvement when performing respiratory gating in clinical oncological PET.

Chapter 5

Lesion Detection in Respiratory–Gated Clinical PET/CT

The purpose of this chapter is to describe the application of the proposed numerical observer to clinical data acquired with the respiratory-gated PET/CT method. The methodology of this aim focuses on the patient data acquisition using a respiratory gating system, and the generation procedure of lesion-present datasets for the performance validation. The following sections of the experimental setup, results, and discussion will then be described.

5.1 Introduction

Respiratory gating allowed clinicians to more precisely detect and treat lung cancer with PET/CT imaging. The respiratory gating protocol was performed during the PET and the CT scanning for each patient. Real-Time Position Management (RPM) respiratory gating system marketed by Varian Medical Systems (Varian Medical Systems, Palo Alto, CA) was operated for monitoring patient's respiratory. The RPM was used to monitor respiratory motion by using a video camera to track the vertical displacement of 2 infrared reflective markers that rigidly mounted on a

plastic block placed on the patient's thorax [70]. By tracking the breathing pattern of the patients, the respiratory gating mechanism correlated lesion positions in relation to the patients' respiratory cycle to remove the breathing motion from PET images. The respiratory gating accounted of a triggered procedure (e.g., amplitude (displacement), fixed time, or phase gating) and the original data were consequently binned into multiple intervals according to the trigger signal in the respiratory cycles. Each binned dataset was then reconstructed to obtain the image corresponding to its time interval [70]. This technique reduced motion artifacts (e.g., lesion smearing effect) and thus improved lesion quantitative assessment, which was severely compromised by respiratory motion in the thorax without gating [73-75].

In this work, the author validated the proposed observer method on respiratory-gated clinical PET/CT in pulmonary oncology. Given the promising results in the previous simulated study, it therefore yielded insight into the performance of the developed observers and provided a confidence to continue proposing to real clinical images. The assessment of lesion detection on respiratory-gated clinical PET/CT using a novel numerical observer was performed for lesion detectability using gated (4D) methods. The proposed numerical observer with two-staged processing was applied: first, accommodating the spatial domain in each gated image using a set of 3D channel CHO. Each gated image was locally prewhitening and matched filtering to decorrelate and detect the presence of spatial signals. Second, integrating all spatial information and the temporal domain using a HO. The intermediate scores computed from all the CHOs were integrated to finally assess lesion detectability accounted both changes in lesion location and shape, which mimicked the viewing of cine movie of the gates by a physician.

Respiratory-gated clinical PET data were acquired from lung-cancer patients. To create a realistic clinical study with lesions present, while ensuring perfect knowledge of the presence

and location of each lesion, synthetic spherical lesions were added to patient data. The real patient data were added with simulated lesion targets, creating so-called *hybrid* images. These hybrid images were sufficient realism and able to characterize the deterministic and stochastic properties of the target lesions [8]. The synthetic 'lesion-present' studies were practically performed for image quality assessment in the clinical applications and had been validated in [17, 18].

For all gates acquired in a respiratory cycle, synthetic simulated spherical lesions were inserted into each gated patient background after incorporating the effect of patient attenuation in the lesion sinograms. Lesion locations were carefully selected to correspond to the most realistic lesion locations within the lung volumes. The validation was performed in a desired marginal detectability of lesion contrasts. The author used the motion of local anatomical features to fix the lesion position each gate in a realistic manner, and assumed that the lesion did not undergo deformation during the respiratory cycle. Lesion detection performance was computed for lesions located at high- and low-motion regions in the lungs, where the base had higher motion and the apex had lower motion. Typical lesion motion was derived from 4D CT (gated CT) images from diseased patients.

The 8-binning gated, motion-corrected, non-gated images were reconstructed with 3D OSEM. The ROIs of lesion-present and lesion-absent were input to the selected observers to compute detection SNRs. The lesion detection performance was compared for: 1) the proposed observer for gated, the 3D CHO for motion-corrected, and the 3D CHO for non-gated methods.

5.2 Overview of Methodology

Six patients were acquired with the respiratory-gating protocol for both gated ^{18}F-FDG PET and gated CT using GE Discovery PET/CT 690. The hybrid images of lesion-present were generated for four 13-mm spherical lesions added to each patient data. The motion fields derived from gated CT were used to translate those lesions in each respiratory gate. Each gated lesion sinogram was added with Poisson noise and then was convoluted with a 3D Gaussian function (FWHM of 3.42 mm), equivalent to the acquisition deteriorated by the point spread function (PSF) of the PET system. The sphere sinogram was fused with the patient sinogram associated with the patient-attenuation sinogram and a scaling factor for the marginal contrast of the lesion within the lung background. The lesion detectability was performed for different approaches to investigate the impact of respiratory-gating system.

5.3 4D PET/CT Image Acquisition

5.3.1 Patient Data Acquisition

Six lung-cancer patients were acquired using GE Discovery PET/CT 690 with the gated respiratory (Gated Resp Vip) tracking system at the University of Texas MD Anderson Cancer Center, Houston, Texas. 4D PET/CT data of the patients were anonymized according to MD Anderson standard operating procedures (SOP) prior to transfer. According to the NIH recommendations for Human Subject Protection and MGH SOP for Human Subject Protection, no IRB was necessary for this study, given that the data originated from studies acquired clinically at MD Anderson and that were anonymized.

^{18}F-FDG was injected to the patient and a typical whole-body PET scan was started 60 min after the intravenous administration of ±4.5 MBq per kg body weight [70]. The bed position of patient's thorax was selected to cover the lung regions near the lung-diaphragm interface within the axial FOV of the scanner. In this PET system, the axial FOV was 157.0 mm with the size of 4.7×6.3×25.0 mm per a detector crystal. The gantry size was 193.0×230.0×226.0 mm with the number of blocks per ring of 64. The radial crystals per block was 9 and the effective ring diameter was 827.0 mm, with the number of rings of 24, and the radial block size of 38.35 mm.

5.3.2 Respiratory Gating System

The tracker data of 8 gates were obtained by monitoring external respiratory signal in the RPM format [74, 75]. The gating rule used in this study was phase gating. The tracker sent a trigger to the scanner at the exhalation in the respiratory cycle and this was used to restart from Gate 1. The triggers were used for the synchronization of the PET list mode data in the trigger-based gating, where the trigger was assumed to indicate the start of the cycle. The time interval between two subsequent occurrences of phase 0 was linearly mapped to a varying phase from 0 to 2π. Figure 15 shows an example of the RPM data during tracking with the respiratory signal, phase, trigger, time input, and time output.

5.3.3 Gated PET/CT

In this study, both 4D-CT and 4D-PET acquisition protocols were employed for 4D PET/CT. Typically, CT was primarily used for attenuation correction for each gate. The 4D-PET and 4D-CT data were spatially matched on a phase-by-phase basis, with the respiratory phases corresponding to each of the 4D-CT image sets selected to match those of the 4D-PET. The

4D-PET and 4D-CT data were sorted according to their phase based on the RPM respiratory signal to produce 8-gated PET and 8-gated CT datasets, with equally spaced over the respiratory cycles. The 4D-PET and 4D-CT data of all gated bins were then transferred from to the scanner console. Figure 16 and Figure 17 depict the 8-gated PET and 8-gated CT images acquired in a respiratory cycle, respectively.

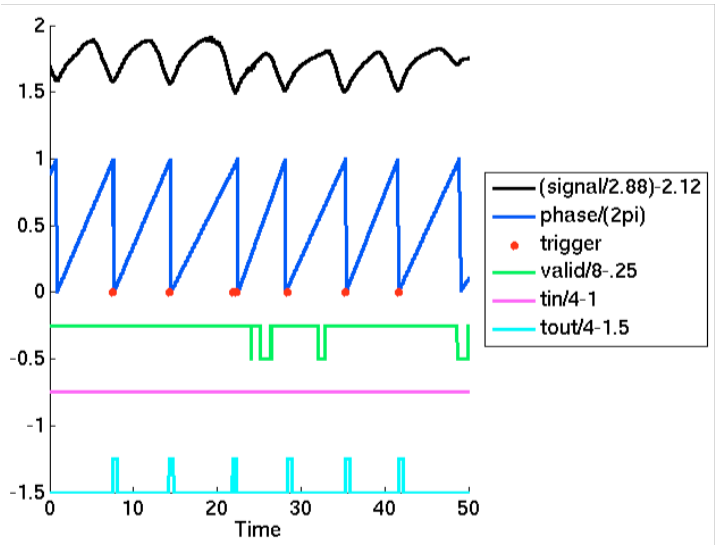

Figure 15 An example of the RPM data during tracking of a normal-breathing patient from time 0 to 50 seconds.

5.3.4 Motion Fields

The 4D-CT was not only used for correcting attenuation in PET images, but also utilized for deriving motion fields. The motion fields were extracted from the gated CT images operating with a non-rigid registration method. In addition, in this study, the motion fields were primarily used for generating the respiratory motion-corrected datasets and for translating the lesions from the first gate to the consecutive gates in the process of generating images with lesion-present. Figure 18 shows an example of the deformation fields derived from 8-gated CT images of a

patient. The pixel space of the deformation fields was 0.98×0.98×2.5 mm with the image size of 512×512×80.

5.4 Generation of Images with Lesion-Present

In order to model in realistic clinical studies with 13-mm lesions present, simulated spherical lesions were added in each respiratory gate yielding synthetic lesion-present studies [17]. The simulated lesions were realistic similar to the point sources (lesions) acquired in air using the GE PET/CT scanner. Figure 19 shows the reconstructed images and the lesion profile plots for the lesions acquired using the GE PET/CT scanner and simulated lesion generated using MATLAB, respectively. Figure 20 shows the procedure of the lesion-present image generation. To process the data acquired from GE PET/CT scanners, it required MATLAB toolbox software of PET and Motion, authorized by the GE Corporation.

As illustrated in Figure 20, a target sphere representing a lesion was generated and projected to become a sinogram. Poisson noise was added to the lesion sinogram to present the embedded noise in the acquired data. Despite the PSF describes the spread of information resulting the resolution capabilities of the imaging system, the incorporation of the PSF of the scanner system into the simulated lesion was essential. The Gaussian function mimicking the PSF of the PET scanner was convoluted with the generated sphere sinogram, where the PSF function was modeled as a 3D isotropic Gaussian kernel with the standard deviation the same size as the spatial resolution of the PET system (FWHM of 3.42 mm for GE Discovery PET/CT 690). This was equivalent to the spherical lesion deteriorated by the imperfection of the PET system. The noisy sphere sinogram was then attenuated by the attenuation volume, generated for each patient, and scaled by a scaling factor to have a desired contrast level. The scaling factor was selected to

obtain the contrast of lesion-to-background for the marginal detectability scheme. The sphere sinograms and the patient PET sinograms were fused as following Eq. (16) in Chapter 4. The lesion-present dataset was directly reconstructed by using the patient sinogram with no presence of the synthetic lesions.

The fused sinogram was then reconstructed using the conventional 3D OSEM with 2 iterations and 24 subsets. The proper corrections of attenuation, dead-time of detector, physical decay of radioactivity, randoms, and scattered photons were included in the image reconstruction process. The postfiltering was performed on the reconstructed images with a Gaussian function with the mean of zero and the standard deviation with the FWHM of 6 mm. The image size was 192×192×47 with the pixel size of 3.6×3.6×3.3 mm. The reconstructed images of the fused lesion and patient background were realistic as shown in [17]. For the gated dataset, the images were reconstructed separately and the motion fields were applied to translate the spherical lesions to different positions from Gate 2 to 8, respectively. In this study, the author assumed that scatter associated with the sphere was negligible as compared to the scatter associated with the patient. For each bed position, four sphere locations that corresponded to the most realistic lesion locations confounded by the respiratory motion within the volume were identified. The assumption made in this study was that the lesions did not undergo deformation during the respiratory cycle for the gated datasets.

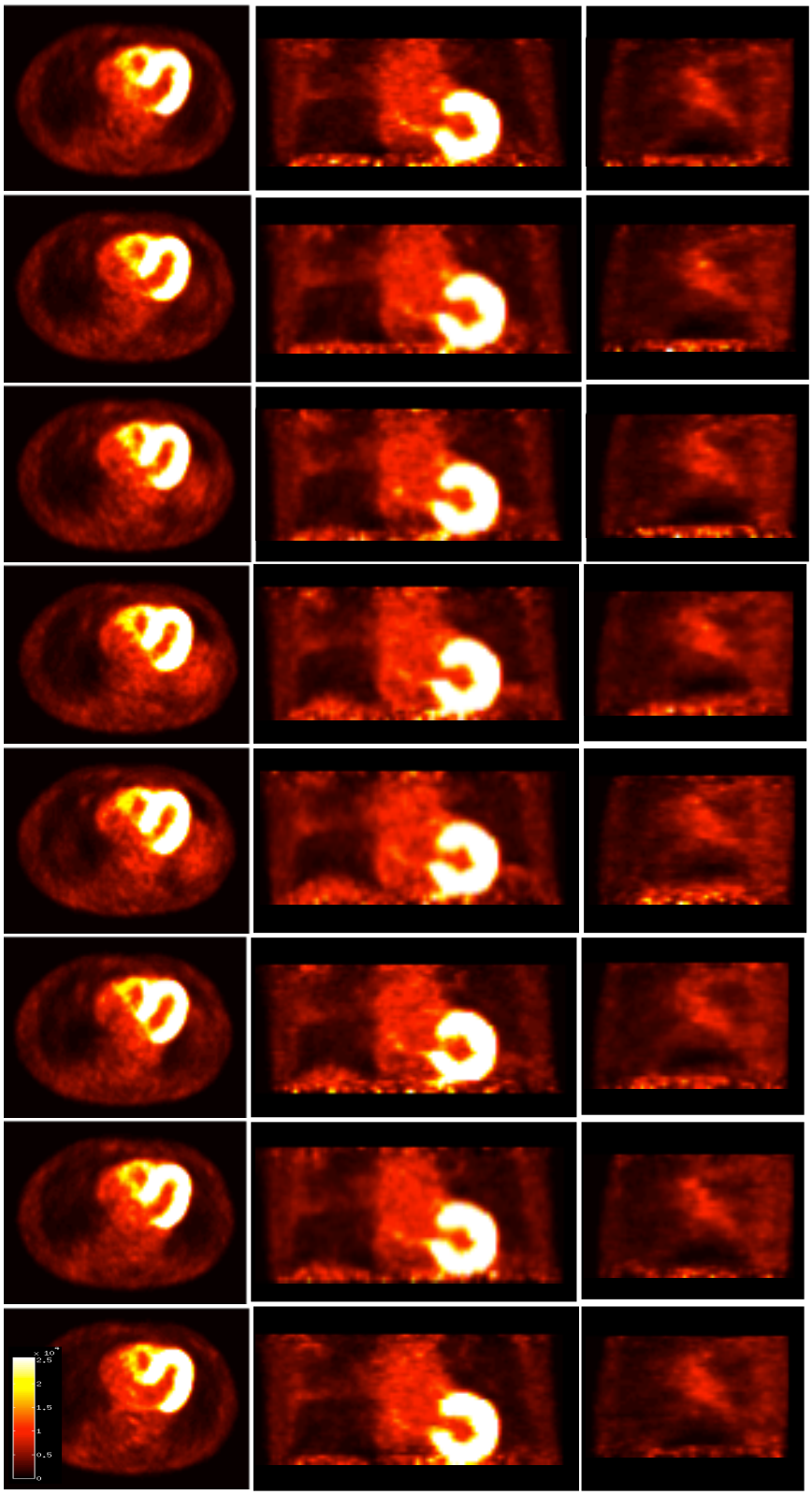

Figure 16 Examples of the gated PET images from Gate 1 to 8 of a patient in the transverse, coronal, and sagittal planes, respectively.

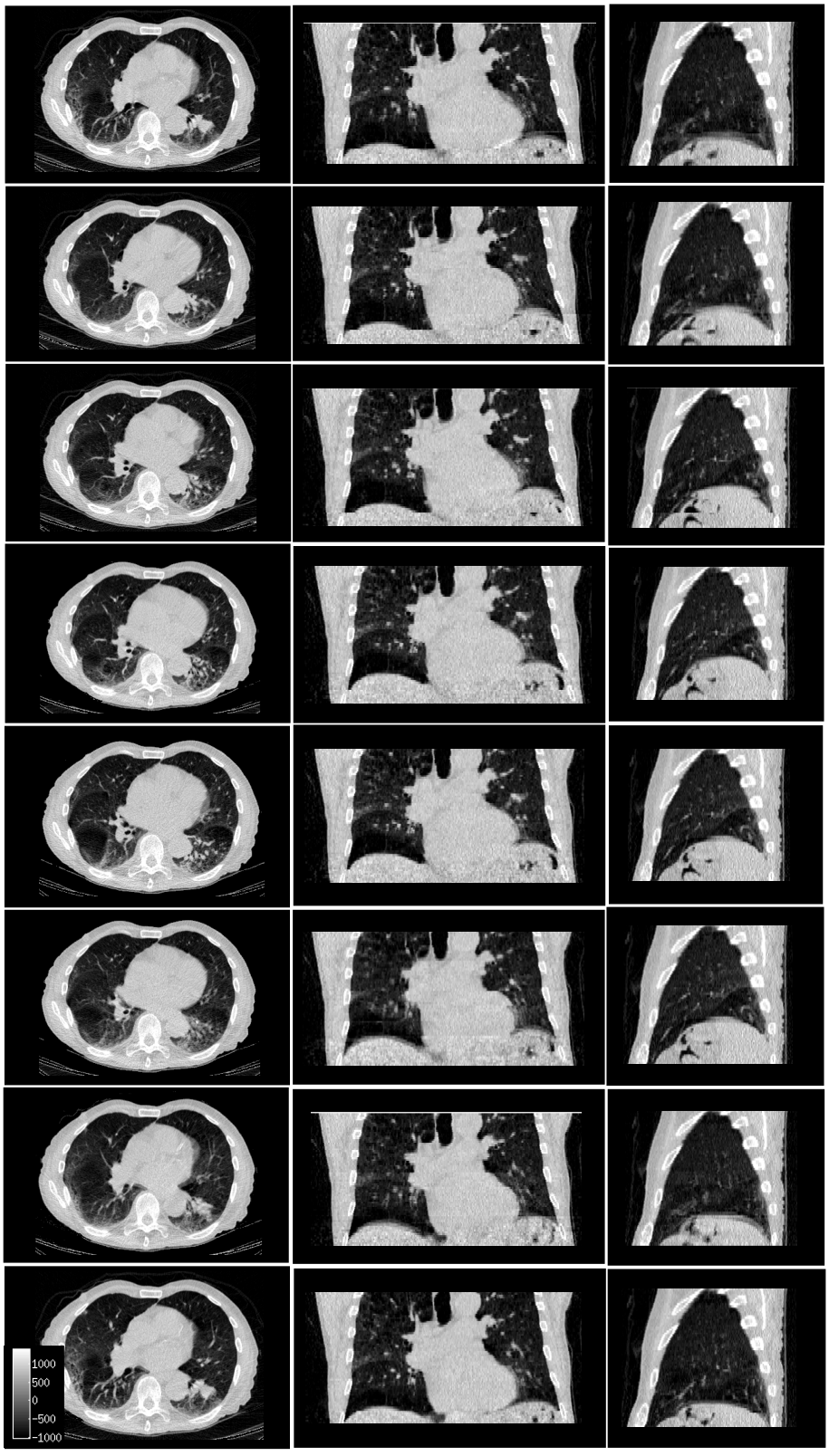

Figure 17 Examples of the gated CT images from Gate 1 to 8 in HU units of a patient in the transverse, coronal, and sagittal planes, respectively.

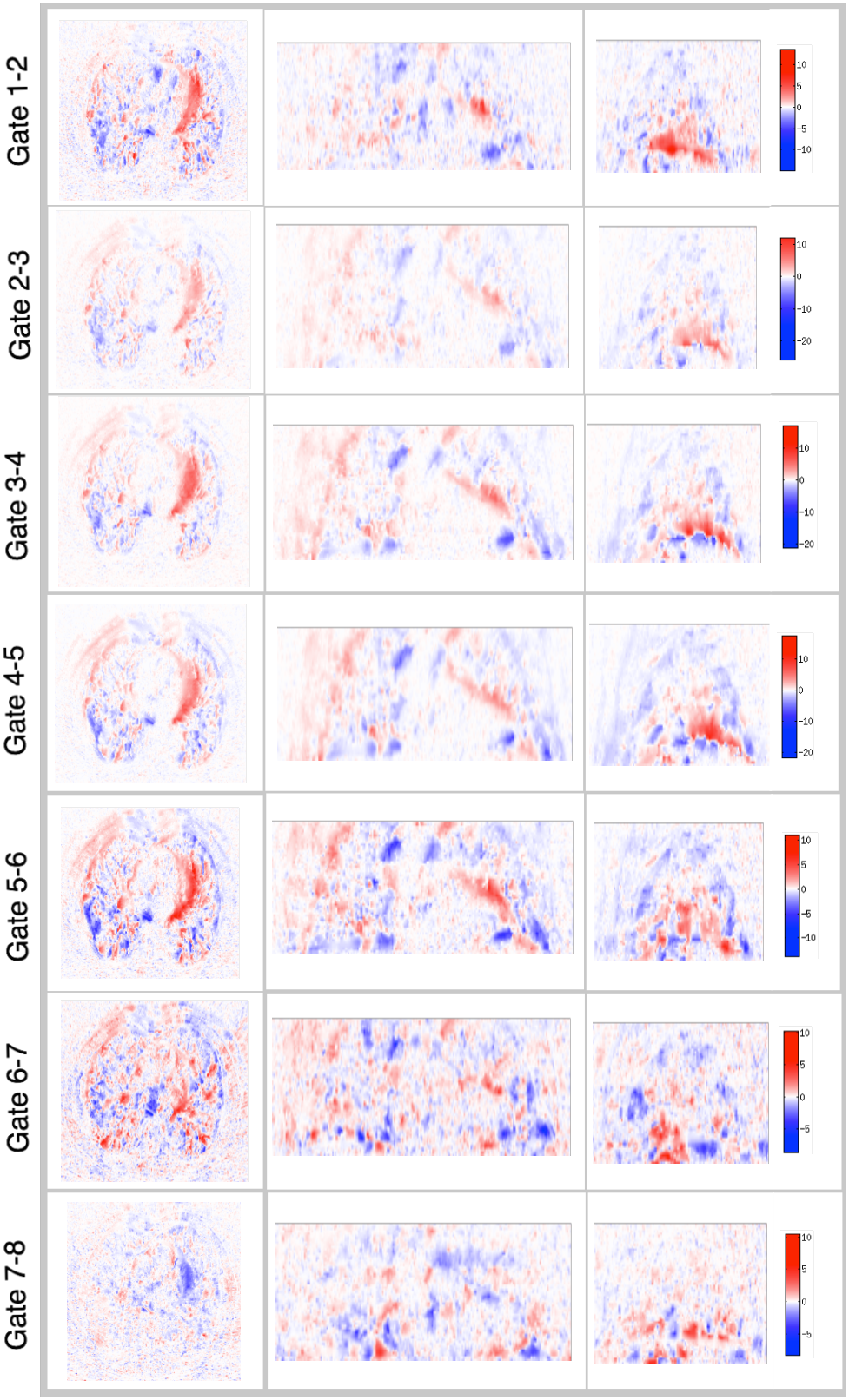

Figure 18 Examples of the deformation fields, ***dx*(*x*,*y*,*z*)**, extracted from the gated CT images from Gate 1 to 8 in pixel units of patient in the transverse, coronal, and sagittal planes, respectively.

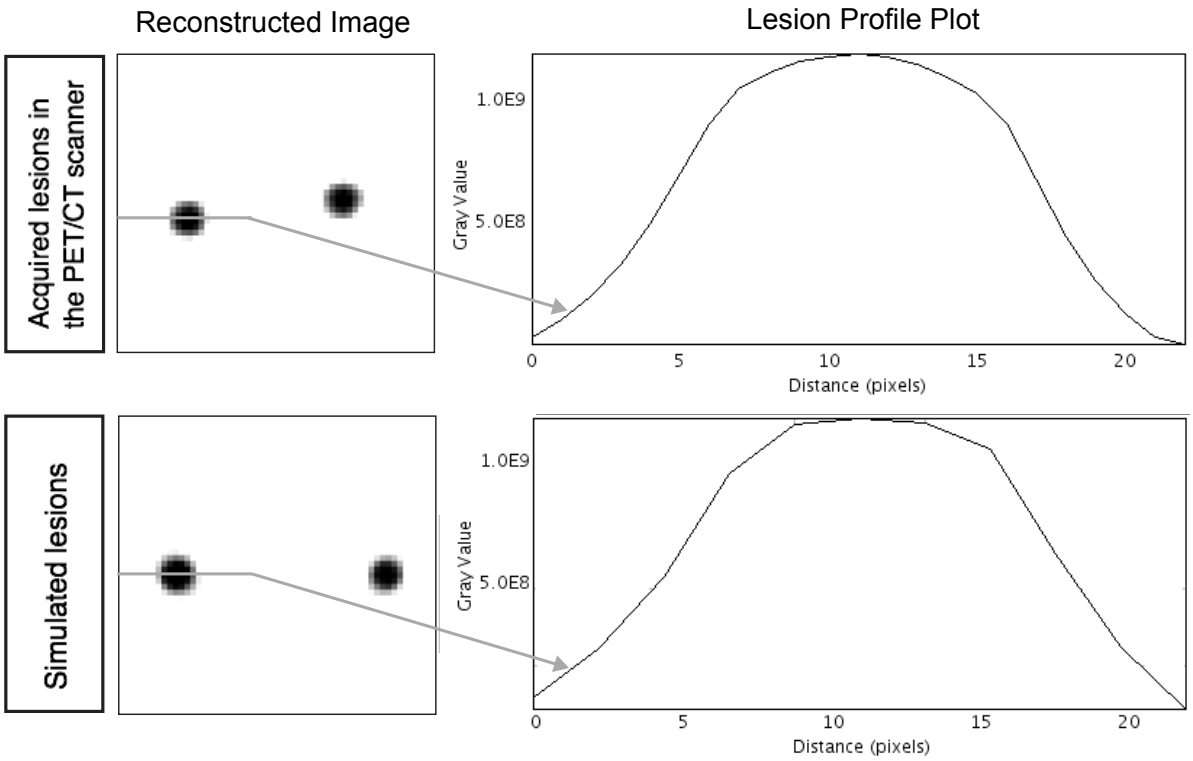

Figure 19 Reconstructed images and lesion profile plots for the point sources (lesions) acquired using the GE PET/CT scanner and simulated lesions generated using MATLAB.

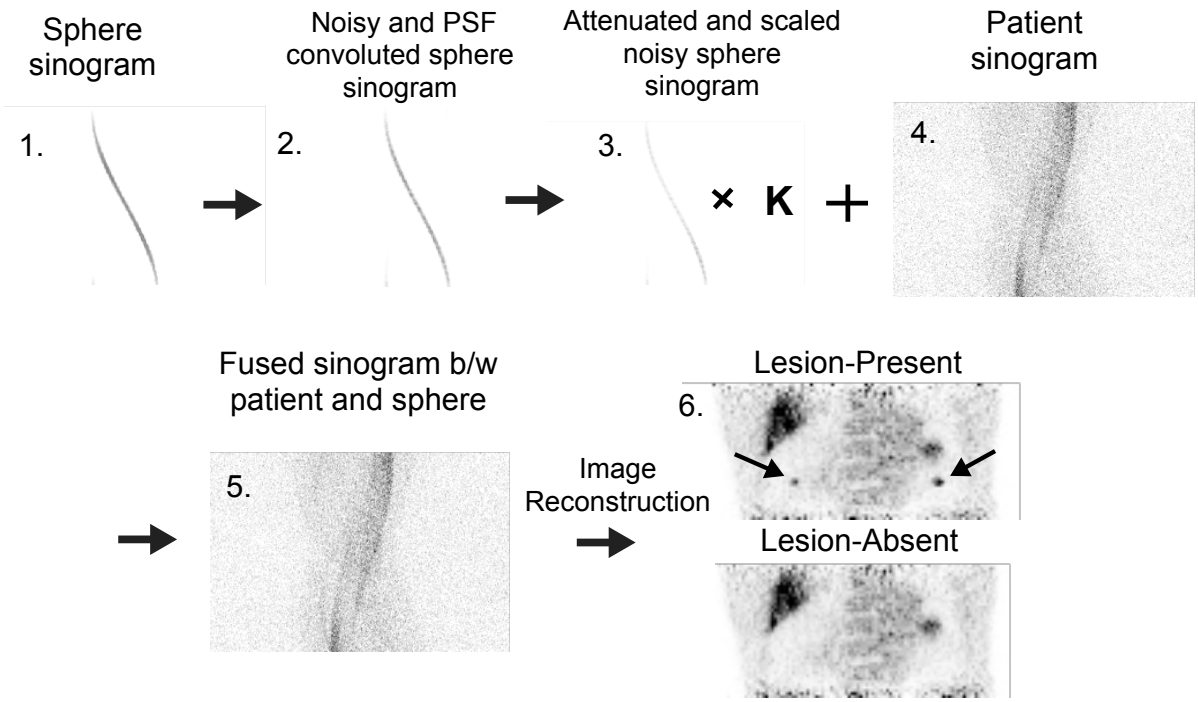

Figure 20 The procedure of the hybrid image generation to form the lesion-present and lesion-absent datasets.

5.5 Experiment Setup

The detection SNRs of the non-gated (3D-CH-NG), motion-corrected (3D-CH-MC), and gated (4D-N-G) methods were compared. The datasets were formed as following:

1) 3D-CH-NG had the location of the lesion averaged over all the gated locations in the gating cycle. The non-gated images were reconstructed from the summation of all the 8-gated sinograms. This 3D-CH-NG was evaluated the detectability using the 3D-CHO methodology. This dataset represented a non-gated study, which the lesion was blurred by respiratory motion.

2) 3D-CH-MC accounted the change in location over the respiratory cycle. This 3D-CH-MC image was corrected the motion by registering all the gated images back to the reference gated frames based on image-based method. This method accounted lesion translation but not deformation and was equivalent to applying the motion correction with the image-based motion-correction scheme.
3) 4D-N-G accounted both changes in lesion location and shape. The proposed 4D numerical observer was applied to all multiple gated volumes. The method allowed information from multiple gates in the computation of the detection SNR, which was designed to mimic the cine movie of the gates viewed by a physician.

The 11×11×11 sub-window of ROI was selected for both lesion-present and lesion-absent datasets. The non-gated sub-window of each lesion was centered at the non-gated centroid, which was computed by averaging the center positions of each lesion over all the 8-gated positions. The motion-corrected sub-image was centered at each lesion back to the first gated frame. The 8-gated sub-images were centered to form the 4D regions. Five channels were applied for both lesion-present and lesion-absent datasets and for all the observer methods.

Four 13-mm lesions were inserted into the six patient backgrounds at the similar locations within the lungs each patient, i.e., right posterior (RL), left posterior (LP), left anterior (LA), and right anterior (RA). In this study, the noise realization number (N_R) was formed with the population of six patients.

5.6 Results

Figure 21 shows the reconstructed images with lesion-absent and lesion-present of the non-gated, motion-corrected, and gated methods. As illustrated, the smearing effect (i.e., the effect of the

contrast lost and lesion dispersion), affected by the respiratory motion, was present in the non-gated case. The lesion of the motion-corrected method showed improved contrast as compared to the non-gated images. In overall, the motion-corrected images had similar image quality to the non-gated images according to the summing all the gated counts while the motion had been removed, which is illustrated in the lesion region with higher contrast as compared to gated images. The gated images are the noisiest as compared to other cases. This indicated that the gated images had reduced lesion smearing by means of respiratory gating, but resulted in reduced statistical photon counts causing the images noisier.

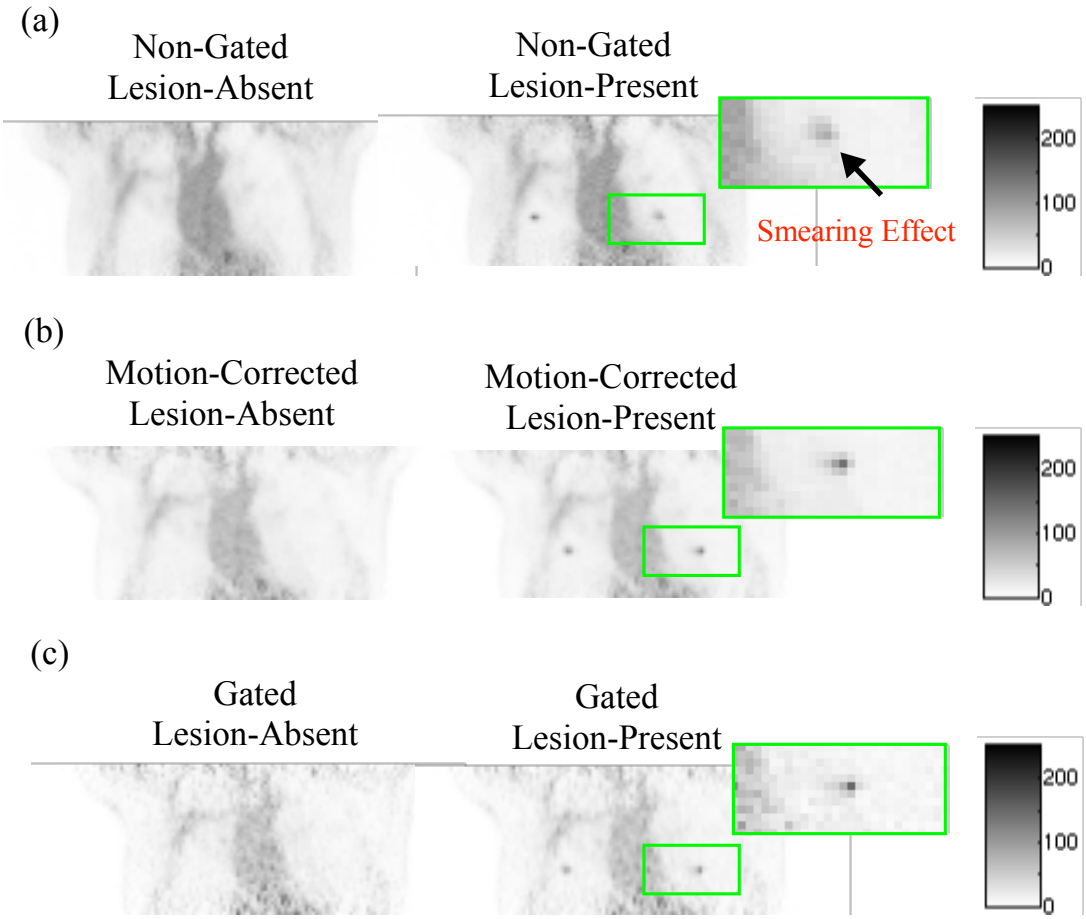

Figure 21 (a) The non-gated, (b) motion-corrected, and (c) gated (Gate 1) images with lesion-absent and lesion-present. The smearing effect (blurring) is indicated by the arrow in the non-gated case, whereas the lesion-present displays better contrast within the noisier image in the gated case.

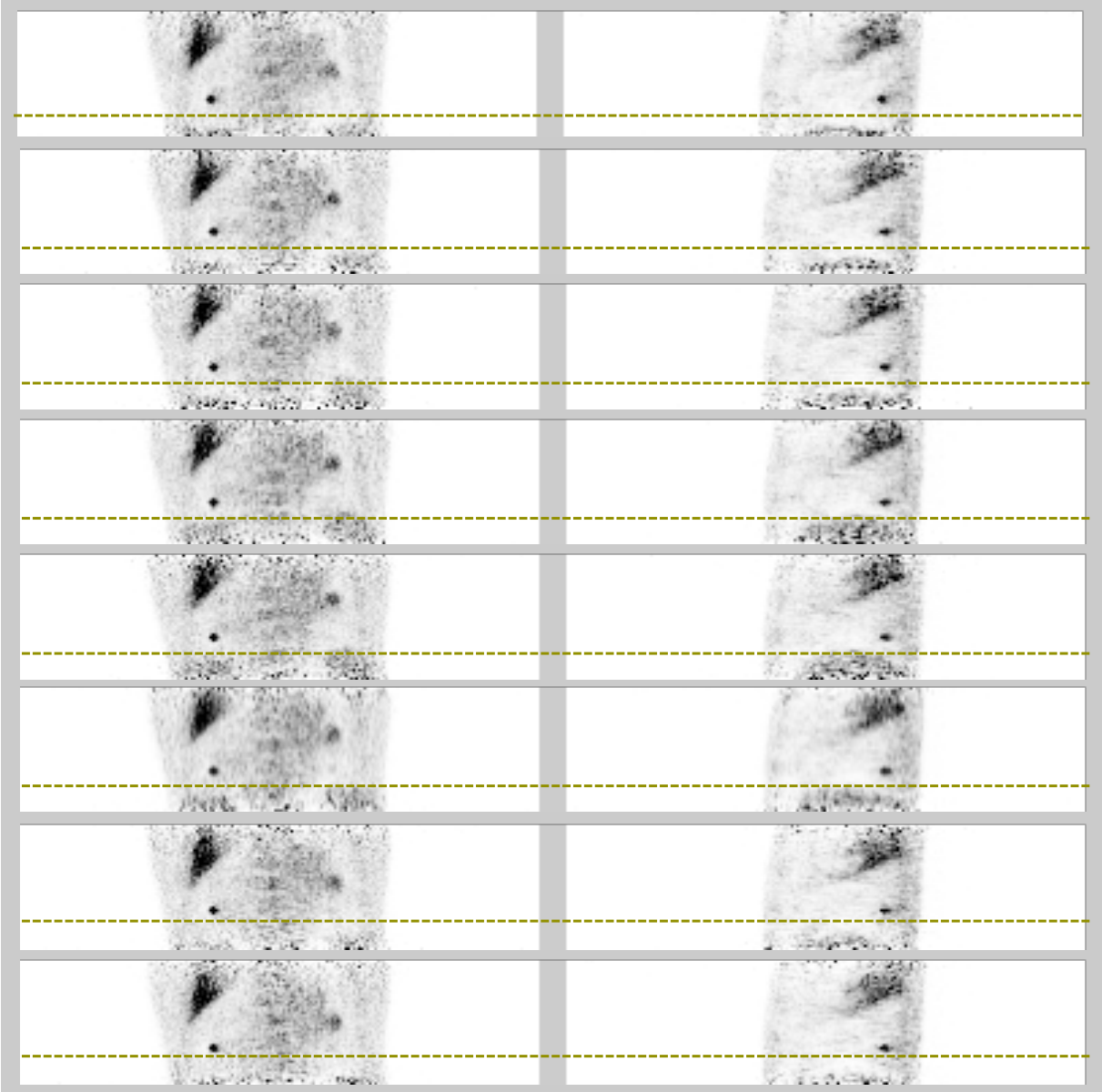

Figure 22 The gated images with lesion-absent from Gate 1 to 8 of a patient.

Table 10 Displacements in millimeter averaged over 6 patients of the 4 lesions from Gate 1 to 8 in a respiratory cycle.

Data	Lesion*	D (mm)	Gate 1-2 (mm)	Gate 2-3 (mm)	Gate 3-4 (mm)	Gate 4-5 (mm)	Gate 5-6 (mm)	Gate 6-7 (mm)	Gate 7-8 (mm)	$\lvert\Delta\vec{r}\rvert$ (mm)
Set#1	RP-1	13	11.1	0.0	28.0	28.0	28.0	28.0	0.6	57.1
	LP-2	13	11.3	0.5	28.0	28.0	54.1	28.0	27.0	78.4
Set#2	LA-1	13	38.0	31.1	79.9	26.1	11.5	30.6	22.3	105.1
	RA-2	13	34.1	31.1	79.3	25.5	21.4	31.2	44.1	111.6

* The lesion locations were right posterior (RL), left posterior (LP), left anterior (LA), and right anterior (RA)

Table 11 Reconstructed contrasts of the eight-gated and motion-corrected images.

Lesion	*$C_{r\text{-}G1}$	$C_{r\text{-}G2}$	$C_{r\text{-}G3}$	$C_{r\text{-}G4}$	$C_{r\text{-}G5}$	$C_{r\text{-}G6}$	$C_{r\text{-}G7}$	$C_{r\text{-}G8}$	**$C_{r\text{-}MC}$
RP-1	2.1 ± 0.1	1.9 ± 0.0	1.8 ± 0.0	1.9 ± 0.0	1.8 ± 0.1	1.8 ± 0.0	1.8 ± 0.0	1.9 ± 0.0	2.0 ± 0.1
LP-2	2.1 ± 0.3	2.1 ± 0.0	2.0 ± 0.0	1.9 ± 0.0	1.9 ± 0.0	2.0 ± 0.0	2.0 ± 0.0	2.1 ± 0.1	1.9 ± 0.3
LA-1	2.2 ± 0.2	2.2 ± 0.1	2.2 ± 0.1	2.3 ± 0.1	2.3 ± 0.0	2.3 ± 0.0	2.4 ± 0.0	2.4 ± 0.1	2.0 ± 0.0
RA-2	2.5 ± 0.2	2.7 ± 0.1	2.5 ± 0.1	2.3 ± 0.2	2.2 ± 0.1	2.2 ± 0.1	2.1 ± 0.1	2.4 ± 0.1	2.1 ± 0.0

*$C_{r\text{-}G}$ from Gate 1 to 8 were computed over 6 noise realizations of each gate. **$C_{r\text{-}MC}$ was the reconstructed contrast of the motion-corrected dataset over 6 noise realizations.

Table 10 illustrates the displacements of the deformation fields from Gate 1 to 8 for 4 lesions placing at different locations. Table 11 illustrates the 4 lesion-to-background contrasts of the gated images for all 8 gates and for the motion-corrected images, respectively. Noting that the lesion-to-background contrasts were calculated the same method illustrated in Section 4.4.1.1 in Chapter 4.

Figure 23 shows the detection SNR comparison computed from 6 patients for 4 lesions placed at the RP, LP, LA, and RA in the lungs. As illustrated in Figure 23, 4D-N-G provided superior detectability performance over 3D-CH-MC and 3D-CH-NG. On average, 4D-N-G improves detection SNR by 391.9% ($p < 0.03$), whereas 3D-CH-MC improves by 85.3% ($p < 0.08$). The relative SNR measurement (Gain = $SNR_{Observed}$ / $SNR_{3D\text{-}CH\text{-}NG}$) of lesion detection

obtained from 4D-N-G was significantly higher than from 3D-CH-MC by 171.2% ($p < 0.02$), where $Gain_{4D\text{-}N\text{-}G}$ was 4.92 ± 1.96 and $Gain_{3D\text{-}CH\text{-}MC}$ was 1.85 ± 0.64. The lesions with higher motion (LP-2, RA-2) had more 4D gains (i.e., $Gain_{4D\text{-}N\text{-}G}$ = 7.5, 5.2) than those (RP-1, LA-1) with lower motion (i.e., $Gain_{4D\text{-}N\text{-}G}$ = 3.8, 3.1). This indicated that the proposed method applied directly on all gated images instead of motion-corrected images provided better lesion detection performance to evaluate the performance achieved using the respiratory gating technology.

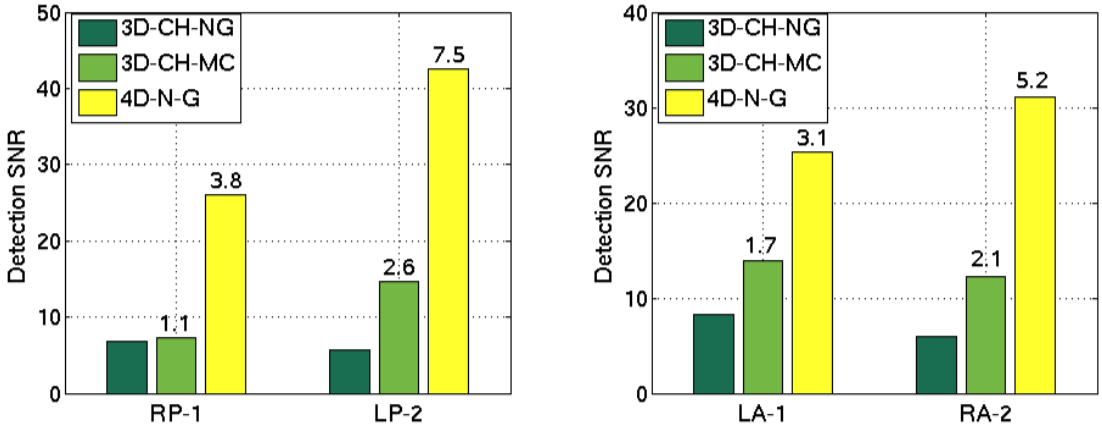

Figure 23 The detection SNR computed from 6 patients for 4 different lesions using 3D-CH-NG, 3D-CH-MC, and 4D-N-G. The spherical lesions located at left posterior (LP-2) and right anterior (RA-2) have higher motion than the lesions at right posterior (RP-1) and left anterior (LA-1), respectively. The SNR gains ($SNR_x/SNR_{3D\text{-}CH\text{-}NG}$) are indicated above the bar plots.

5.7 Discussion

By validating on clinical images, the proposed novel observer provides significant improvement in lesion detectability using respiratory-gated clinical PET/CT over the conventional 3D observer approach on motion-corrected and non-gated images. The outcome of the proposed framework confirms that the proposed 4D approach can be generalized to more complex clinical images.

This indicates that this proposed method is appropriate for lesion-detection evaluation of 4D images acquired using respiratory-gated PET.

The proposed 4D approach yields superior detection SNRs over the 3D approach; whereas, the lesion-detection performance evaluated on motion-corrected images cannot make a conclusion for the impact of the achieved performance gained from the respiratory gating method. As expected, the potential registration errors occurring in the motion-correction method may deteriorate the observer performance. In this study, the motion fields were derived from gated CT images, which were separately acquired before the gated PET acquisition. Even though both 4D-PET and 4D-CT were spatially matched on a phase-by-phase in a respiratory phase, there might be extensive errors. The 4D CT images were separately acquired to improve the registration in each gate; however, the intra-gate errors and post-processing errors can be embedded and reduced the image quality. Similar to our previous study in simulated images, the registration error problem between the PET and CT image modalities of all gated images based on image-based method may cause a major issue for both the attenuation correction and motion field extraction. For the attenuation correction during the PET reconstruction, the PET images are necessary corrected for attenuation using the attenuation volume obtained from the CT acquisition. The registration problem of these two modalities can cause inferior to the overall performance of lesion detection. For the motion correction, applying the motion fields derived from CT images to the PET images can cause extensive errors during the motion correction process. In addition, the nonlinear characteristics of OSEM of the direct summation of registered images for all gated frames may remain the bias issue in the post-reconstruction motion-corrected images, which is also mentioned in the discussion section in Chapter 4. As a result, the detection performance can be deteriorated by these aforementioned errors. This study

indicated that the proposed method applied directly on all gated images instead of motion-corrected images could avoid the inaccuracy of post processing obtained from the motion correction methods.

The key evidence of this study is that it shows the performance of the proposed novel observer to properly accounts on the complex variability of the noise embedded in clinical images. Typically, the noise in PET imaging has an impact on the clinical diagnosis. Particularly, clinical PET images have the sources of variability arising from quantum noise in the imaging process, anatomical variability in the ensemble of subjects being imaged, and the noise originated from the image reconstruction process that can induce a strong correlation structure in the resulting images [5]. The detection SNR has shown that the proposed observer appropriately accommodates the statistical properties of the noise variability of these sources in multiple gated images. Hence, the lesion-detection outcome in this study has shown that the proposed observer measures the uncertain variability of the realistic noise and the signals in clinical images properly.

For the objective assessment study, the hybrid images allow the truth verification and the possible presence of multiple lesions on a single image in the clinical validation. As known, the most challenging is the verification of absolute "truth" for images obtained from clinical studies. This means that other equally or even more reliable information about the presence or absence of lesion in the patient is necessary. Inserting a lesion in the patient background sinogram before reconstruction is therefore a practical procedure for generating the hybrid images of lesion-present demonstrated in this study. On the other hand, often nonimaging test (e.g., surgical results) may be obtained for verification of "truth" when clinical images are used [1]. This study

showed that using the hybrid images to validate the lesion-detection performance is hence realistic and crucial for clinical studies.

Alternative to the simulated point sources used as the synthetic lesions, a sphere phantom of a point source acquired with the same geometry of the PET/CT scanner is also sufficiently realistic to generate the hybrid images of lesion-present. The synthetic lesions can be added in each respiratory gate using, for example, plastic spheres filled with 74 kBq/ml of Ge-68 being acquired separately at the exact location in the patient volume. Practically, a synthetic lesion can be performed as: first, a grid can be used with 1,300 threaded holes that allows positioning of the spheres at any desired location in the PET scanner field of view within 5 mm accuracy in all 3 directions. Then, a styrofoam pad attached to the grid can be used to position more finely the lesion within 1-2 mm.

One reason that may cause larger SNR disparity between the 4D approach and the 3D approach of motion-corrected images than that in the simulation study in Chapter 4 may be because larger respiratory motion obtained from the clinical data. In the previous study, the displacements of deformation fields were 17.61 – 30.50 mm, whereas this clinical had 57.1 – 111.6 mm of the displacement amplitudes. This causes larger $Gain_{4D\text{-}N\text{-}G}$ in this clinical study (1.7 – 7.5) than that in the simulation study (1.2 – 1.7).

It is suggested to have more number of patient subjects to reduce the variability in the population of subjects. The larger number of patients can decrease variability of the statistical properties input to the SNR computation with reasonable effort.

5.8 Chapter Summary

This chapter demonstrated the clinical study of the performance in lesion-detection tasks on respiratory-gated, motion-corrected, and conventional non-gated methods. The proposed framework evaluated on multiple gated images provided superior performance over the other methods using hybrid images of lesion-present. In each of 8-gated frames, the simulated lesion sinograms were added to a set of background clinical PET data. Typical lesion motions were derived from gated 4D-CT images from the same diseased patients, and the motion of local anatomical features was used to fix the lesion position within a respiratory cycle in a realistic manner. Lesion detection performance was compared for lesions located at high- and low-motion regions in the lungs, where the base had higher motion showed high detection SNR than that at the apex with lower motion.

Chapter 6

Lesion Detection in Kinetic Parametric PET

The purpose of this chapter is to describe the application of the proposed numerical observer to kinetic parametric PET imaging. The first section describes the overview of the current research status. Then, the methodology of the patient data, data analysis with kinetic compartmental model analysis, Patlak graphical analysis, and image derived input function will be provided. Next, the section demonstrates the comparison of lesion-detection performance of different methods.

6.1 Introduction

In addition to the spatiotemporal data, another aim of this dissertation was to develop methods to assess lesion detection performance in parametric imaging. The complexity of parametric data (i.e., 3D in space + parametric *k*-domain) is the major problem and limited numerical observers are able to support these data. As a result, there are limited fully image assessment studies performed to investigate the observer performance for lesion detection in parametric imaging.

There is very limited numerical observer for assessing detection performance outcomes from different quantitative approaches and comparing those outcomes of multidimensional PET images. The proposed 4D numerical observer was capable to accommodate multiple dimensions of the data. Hence, the task-based assessment could be performed and compared among different approaches. This study was one of the early pilot studies in applying the objective performance assessment to parametric imaging on lesion detection tasks.

In this chapter, the author applied the novel numerical observer to assess lesion detection on kinetic parametric images and compared the detectability of lesions using parametric images, dynamic images, Patlak graphical analysis, and static images. The assessment of image quality of parametric PET imaging was performed using the proposed 4D numerical observer. The proposed numerical observer incorporating all parametric information was applied as a two-stage process illustrated in Chapter 3. First, 3D-CHO accounted on each parametric domain (i.e., K_1, k_2, and k_3) of parametric image volumes. Each parametric image volume was preprocessed by a 3D-CHO with a localized prewhitening process to decorrelate signals, and a localized matched filter to detect the presence of signals embedded in noise within the individual kinetic parameter (K_1, k_2, and k_3). Second, HO integrated the parametric information together to result the figures of merit. The scores of all the CHOs were integrated by a HO using an additional prewhitening and matched filter to yield the overall SNR.

The lesion detection performance of the proposed observer was evaluated using the ^{18}F-FDG PET data of 12 head and neck cancer patients (age 63±8 yrs, 370 MBq dose). The OSEM reconstructed images of dynamic PET were applied to estimate kinetic parametric and Patlak images. An irreversible two-compartment model was selected to derive the parametric outcomes using an in-house software for the parametric estimation process with image-derived

input functions. The SKE detection in the BKE uncorrelated noise of clinical data was performed. For SKE/BKE tasks, the lesion detection was performed using a numerical observer that positions a template over the location of the expected target tumor to yield the figures of merit. An 11×11×11 window centered on a target lesion was formed along with the corresponding backgrounds for 25 tumor targets in all patients.

The proposed 4D (3D+*k*) numerical observer and the conventional 3D CHO were employed to compare the detection performance in different quantitative approaches of kinetic analysis. The appropriate observers were selected to match the dimensionality of the investigated images. The 4D numerical observer was applied on parametric and dynamic image volumes due to they were both in the four dimensions. The 3D CHO was applied to static and Patlak PET image volumes owing to their 3D information domain.

6.2 Overview of Methodology

The validation of our approach was performed using 12 head-and-neck cancer patients with totally 25 tumors. All patients underwent the PET/CT scans of dynamic data acquisition for 45 minutes using FDG. Each image frame was reconstructed using the iterative reconstruction. After all image volumes have been reconstructed, the dynamic images were then analyzed using compartmental model analysis. An irreversible two-tissue compartmental model was used, which was sufficient to describe the time-activity curve for the data that acquired less than 60 minutes. Then, the rate constants K_1, k_2, and k_3 were estimated using non-linear least square fitting and image derived input function. The dynamic images were also analyzed using the simplified parametric method resulting K_i, which was the combination of K_1, k_2, and k_3. The experiment was then performed for comparing the lesion detection performance for 4 methods, i.e., static,

dynamic, Patlak, and parametric images. The template window of sub-image ROI was placed centered at the target lesion together with the corresponding background. For all the investigated methods, all 25 tumors were ensemble images that input to the proposed numerical observer.

6.3 Patient Studies and PET/CT Scanning

Twelve patients (11 males, 1 females; age, 63 ± 8 years old) with 25 biopsy-proven tumors, clinically suspected head-and-neck cancer were included in this study. All data acquisitions were performed on a GE Discovery ST-16 PET/CT scanner (GE healthcare, NY). The GE Discovery ST combines a multi-slice helical CT scanner with a PET tomograph, which consists of 10,080 BGO crystals arranged in 24 rings. The crystals are in the dimension of 6.3×6.3×30.0 mm^3 and organized in blocks of 6×6 crystals, coupled to a single photomultiplier tube with four anodes. The FOV covers 157 mm and the coincidence time window is set to 11.7 ns. The low- and high-energy thresholds are set to 375 and 650 keV, respectively.

Each patient was administered with 370 MBq of ^{18}F-FDG into the antecubital vein and the PET acquisition simultaneously began. The single-bed PET data of the head and neck regions were acquired in the list-mode format within the PET FOV. The 45-min dynamic data were stored into frames of: 4×20s, 4×40s, 4×60s, 4×180s, and 5×300s during the acquisition. Each PET image volume was reconstructed using a standard OSEM together with the Fourier rebinning algorithm (FORE) with 5 iterations and 32 subsets. The proper corrections for attenuation, normalization, scatters, and randoms photons were included in the reconstruction process. The post filtering with FWHM of 5.1 mm was applied to the reconstructed images. The image matrix size was 128×128×47 with a 4.7×4.7×3.3 mm^3 voxel size.

6.4 Data Analysis

6.4.1 Kinetic Compartmental Model Analysis

Mathematical kinetic models were used to analyze time sequences of PET image volumes. Two-tissue compartmental modeling with a plasma compartment of ^{18}F-FDG kinetics was applied for determining rates of glucose metabolism. This model describes the hexokinase-catalyzed phosphorylation of glucose that is the step introducing glycolysis for deoxyglucose and 2-deoxy-2[^{18}F]fluoro-D-glucose. As shown in Figure 24(a) and 24(b), hexokinase catalyzes the phosphorylation of glucose to glucose-6-PO_4 and FDG to FDG-6-PO_4, respectively. FDG is a competitive substrate with glucose in both transport and phosphorylation, but FDG-6-PO_4 is not a significant substrate for further metabolism. The FDG-6-PO_4 is not converted into glycogen to any significant extent for further glycolytic pathway and does not diffuse across cell membranes [1]. Hence, the primary FDG products of phosphorylation are trapped in the tissue and accumulate where they are formed for reasonably prolonged period of time [25]. This allows us to image the desired regions in the studies. Typically, the glucose metabolism in the tissue of interest is assumed to be in a steady state; therefore, the rate of the hexokinase reaction is the rate of the entire process of glycolysis [1].

Figure 24(b) represents the two-compartment model whose configuration consists of the FDG in tissues and the FDG-6-PO_4 in tissues, which corresponds to the comparable distributions of glucose. The FDG in plasma is not a compartment of the model because it is measurement component, not the one under study [25]. The first-order rate constants K_1 and k_2 describe the transport of FDG from blood to tissues and from tissues to blood, respectively. Whereas the first-order rate constants k_3 describes the phosphorylation of FDG.

In this study, an *irreversible* compartmental model was used, in which the dephosphorylation was ignored, i.e., k_4 was assumed to be zero. The transport and rate constants of the tracer were assumed to be linearly related to the concentration differences between the two compartments. According the scan duration in this study was 45 min, the irreversible model was sufficient to describe the tissue time activity curve (TAC) as reported by Dhawan *et al*. [128], who suggested applying the irreversible model for a scan duration less than 60 min.

Similar to the typical compartmental model analysis, several assumptions underlaid the compartmental model to interpret PET data were applied. The physiological process and molecular interactions were not influenced by injected radiotracer and should be constant during PET measurement. This was because of the sensitivity of PET imaging in the range of 10-11 – 10-12 mol/l, thus most PET studies fulfilled this assumption [24]. Each compartment was presumed to be homogeneous and the radiotracer that passed from one compartment to the other was instantaneously mixed in the compartment.

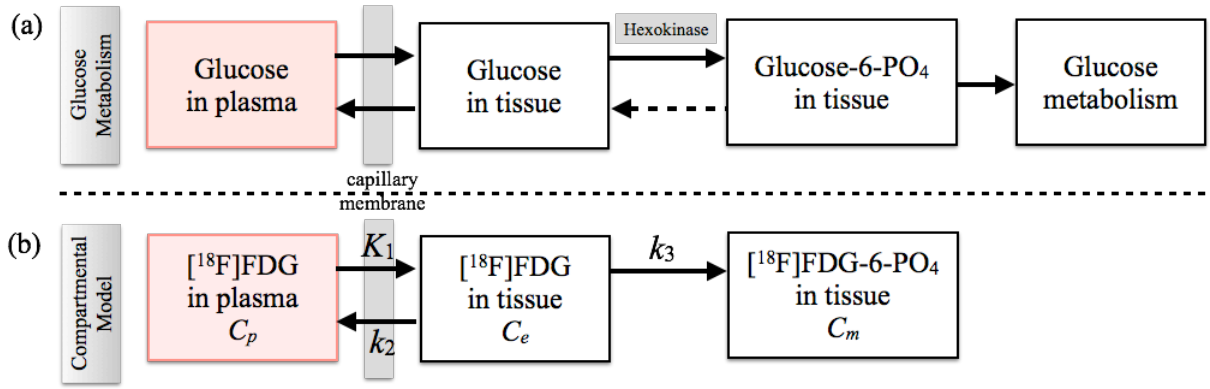

Figure 24 (a) The pathway of the glucose metabolism and (b) a two-compartment FDG model of irreversible dephosphorylation with the three first-order rate constants describing transport between the compartments. C_p, C_t, and C_m are the concentrations of FDG in plasma, tissue, and metabolized FDG (^{18}F-FDG-6-PO$_4$) in tissue, respectively.

The ordinary differential equations expressing the balance between the mass entering and exiting each compartment can be described as functions of time t [min] as followings:

$$\frac{dC_e(t)}{dt} = K_1 C_p(t) - \left(k_2 + k_3\right) C_e(t), \tag{17}$$

$$\frac{dC_m(t)}{dt} = k_3 C_e(t), \tag{18}$$

where C_p represents the concentrations of ^{18}F-FDG in the arterial plasma, C_e is the concentration of ^{18}F-FDG in the exchangeable pool in the tissue, and C_m is the concentration of metabolites of ^{18}F-FDG in the tissue, predominately ^{18}F-FDG-6-phosphate. The coefficients of the differential equations (i.e., Eqs. (17) and (18)) in the model are reflective of inherent kinetic properties of the particular tracer molecule in the system [25].

The solution of Eqs. (17) and (18) that constitutes the irreversible model can be expressed as: [129]

$$C_t(t) = \frac{K_1}{k_2 + k_3}\left(k_3 + k_2 e^{-(k_2+k_3)t}\right) \otimes C_p(t). \tag{19}$$

For the measured data obtained by a PET scanner, the total concentration of activity in the tissue, C_{PET}, are a summation of C_e and C_m, which is in the precursor and product tissue pools.

$$C_{\mathrm{PET}}(t) = C_e + C_m \tag{20}$$

By formally comparing the output of the model Eq. (19) to the experimentally obtained PET data Eq. (20), the kinetic parameters of K_1, k_2, and k_3 can be estimated. The information of the metabolism process in the tumor was extracted from the irreversible model driven by the radioactivity concentration in the blood supply [25]. The parameter estimation was performed by a non-linear least squares fitting procedure between the model and measured PET data with an input function of the arterial radioactivity concentration, $C_p(t)$. The $C_p(t)$ was measured

separately from the PET data acquisition. Typically, one assumes that the parameters of the model are time-invariant, at least over the duration of the study. The kinetic parameters estimated from a PET study provide a snapshot of the average state of the system. Due to the non-linear fitting was computational expensive, the ROI of the PET images was carefully chosen to be processed. In this study, the ROI of each patient was selected using a matrix size of 41×11×22 to ensure that the interested tumor and the surrounding regions were included in the ROI window. The ROIs were then performed using the non-linear fitting procedure based on the voxel-by-voxel fitting framework.

6.4.2 Patlak Graphical Analysis

The Patlak analysis [86, 87] is the most broadly-used graphical approach for kinetic analysis. This approach approximates a non-linear into linear problem and is appropriate when there is an irreversible or nearly irreversible trapping step in the model. The Patlak method employs the combinations of the parameters as macro parameters, in which it is sometimes more useful to represent the observed data in the macro perspective rather than the individual parameter. By assuming linear transfer kinetics, this Patlak model consists of a blood-plasma compartment, a reversible tissue region with an arbitrary number of compartments, and one or more irreversible tissue regions. Conceptually, the transformations of the Patlak plot convert a bolus injection experiment to a constant infusion. After appropriate mathematical transformation, the measured data can be converted into a straight-line plot whose slope and/or intercept has physiological meaning. For the case when the input function is not a constant, Eq. (21) expresses the solution of the equations for this Patlak model [24].

$$\frac{C_t(T)}{C_p(T)} = K_i \frac{\int_0^T C_p(t)\,dt}{C_p(T)} + \frac{K_1 k_2}{\left(k_2 + k_3\right)^2} \text{ for } t > t^*, \tag{21}$$

where $K_i = \frac{K_1 k_2}{\left(k_2 + k_3\right)}$ can be obtained by fitting the slope of the line after equilibrium t^*, i.e., $dC_f / dt = 0$ as C_f is the radioactivity concentration of nonmetabolized tracer in the tissue.

As illustrated in Eq. (21), a straight-line fitting process was performed on a graph of the ratio of the total tissue solute concentration at the times of sampling, and the plasma concentration at the respective time $C_t(T)/C_p(T)$ versus the ratio of the arterial plasma concentration-time integral to the arterial plasma $\int_0^T C_p(t)\,dt / C_p(T)$. The slope K_i is directly proportional to the rate of glucose. The ordinate intercept is proportional to the initial volume of distribution V_0. The glucose metabolism rate was then estimated. Because either lack of equilibration with the plasma of any precursor pool in the ROI or loss of metabolic products might cause nonlinearity of the graph, the identification of the appropriate linear segment of the curve was required for Patlak graphical analysis.

6.4.3 Image Derived Input Function

Because the frequent manual sampling of the arterial blood is invasive, the arterial-input function can be directly derived from PET images [130, 131]. The arterial-input function was estimated by extracting components of blood from PET images by means of image processing. In this study, the PET scan was acquired within a single-bed position of the head-and-neck region. Thus, the carotid arteries within the head-and-neck areas were manually segmented. Due to a common

strategy assumed that all pixels of the interest in the PET data shared the same arteries, the same arterial-input functions were used for both the tracer kinetic modeling and the Patlak methods.

6.5 Experiment Setup

The tumor locations of the head-and-neck anatomical background were manually defined in each patient. The target tumors were determined by considering the common high-uptake regions on the last dynamic frame, Patlak, and parametric image volumes. Then, the center of each target tumor was approximately defined within a template window of size 11×11×11. The same ROI position and the same size of an 11×11×11 window centered at a target tumor were used for all the approaches. Twenty-five tumors in the twelve patients were stacked to be ensembles of targets and realizations of the measurement noise. These ensembles were used to compute covariance matrix in the SNR computation for all methods. The D-DOG channel functions illustrated in Eq. (5) were selected for all the numerical observer methods. This was because the target lesions are mostly non-spherical shape and the D-DOG functions also included the frequency responses of the human visual system. The lesion detection FOMs were computed for: 1) S: static PET (last frame), 2) D: dynamic PET after 20 min, 3) P: Patlak, and 4) K: kinetic parametric image volumes of K_1, k_2, and k_3. The useful FOM included in this study were: 1) detection SNR and 2) AUC, as described in Eqs. (12) and (14).

Few factors were considered in the detection performance comparison among these four investigated approaches (i.e., static, dynamic, Patlak, and parametric images). Due to the fact that kinetic parameters (i.e., Patlak, and parametric images) were assumed to be a reflection of steady state of the system, the same steady state of the other approaches should also be used. Therefore,

the dynamic PET images after 20 minutes (last five frames), referred to the nearly steady state in this study, were used in the comparison.

6.6 Results

Figure 25 shows the examples of the investigated images with the presence of tumors in different approaches to utilizing the temporal information (i.e., dynamic PET, Patlak, and kinetic parametric images). As shown, the last frame of the dynamic PET images had high FDG uptake both in the background and the tumor. In contrast to dynamic PET, the parametric images (i.e., Patlak, kinetic parametric) showed lower background uptake but higher tumor uptake. By considering of the kinetic parametric images, the parametric volumes of K_1 and k_2 were noisier than that of k_3.

Table 12 illustrates the average of lesion-to-background contrasts over the 25 tumor ensembles of the 12 patients. As illustrated in the last five frames, the lesion-to-background contrasts of the dynamic PET increased as the time frames increased. The lesion-to-background contrasts of K_i and k_3 were relatively high, whereas the other contrasts (i.e., PET, K_1, k_2) were comparably low.

Figure 26 shows the SNR and AUC for the detection performance of the four different approaches (i.e., static, dynamic PET, Patlak, and kinetic parametric). As shown, the kinetic parametric method provided superior detection performance over the static, dynamic PET, and Patlak methods. SNR-K was 83.4%, 70.4%, and 27.7% ($p < 0.01$) greater than SNR-S, SNR-D, and SNR-P, respectively. The resulting AUC-K improved over AUC-S, AUC-D, and AUC-P, respectively.

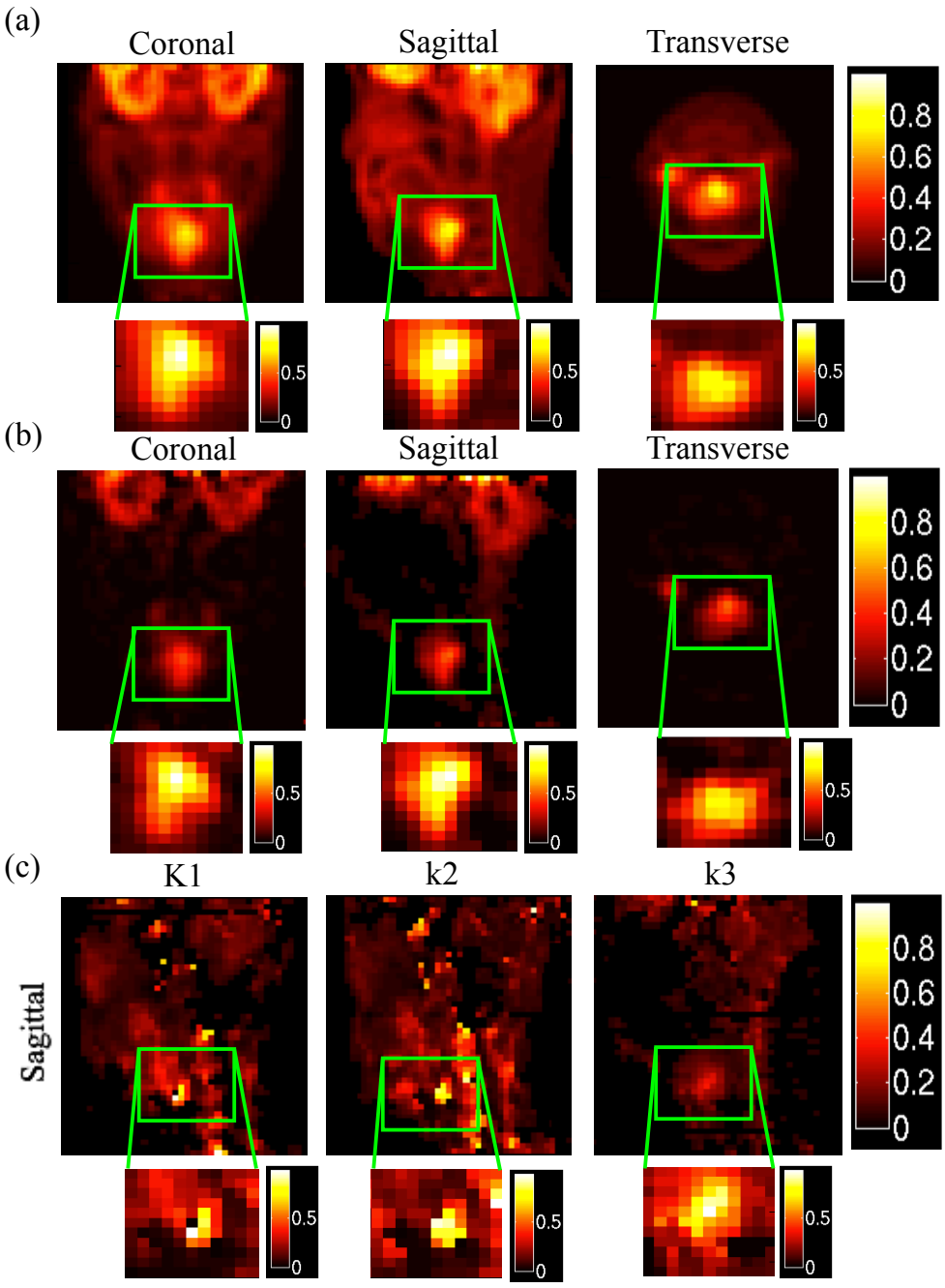

Figure 25 The examples of (a) the last frame of the dynamic PET image at 40 min (5 min scan), (b) the Patlak parametric image volume, and (c) the kinetic parametric volumes of K_1 [mL/min/g], k_2 [min^{-1}], and k_3 [min^{-1}] estimated by an irreversible two-compartment model, at the same view of the sagittal plane in (a) and (b).

Table 12 The average lesion-to-background contrasts over 25 tumors (ensembles) for 12 patients.

Method	Contrast of Lesions				
PET	N_{F-4}	N_{F-3}	N_{F-2}	N_{F-1}	N_F
	3.4 ± 1.3	3.9 ± 1.5	4.4 ± 1.7	4.8 ± 1.9	5.2 ± 2.0
Patlak	K_i				
	20.7 ± 13.1				
Kinetic Parameters	K_1	k_2		k_3	
	5.8 ± 2.7	4.3 ± 1.8		13.7 ± 8.2	

N_F is the last frame of the dynamic PET images. N_{F-1}, N_{F-2}, N_{F-3}, and N_{F-4} refer to the consecutive frames before the last frame, respectively.

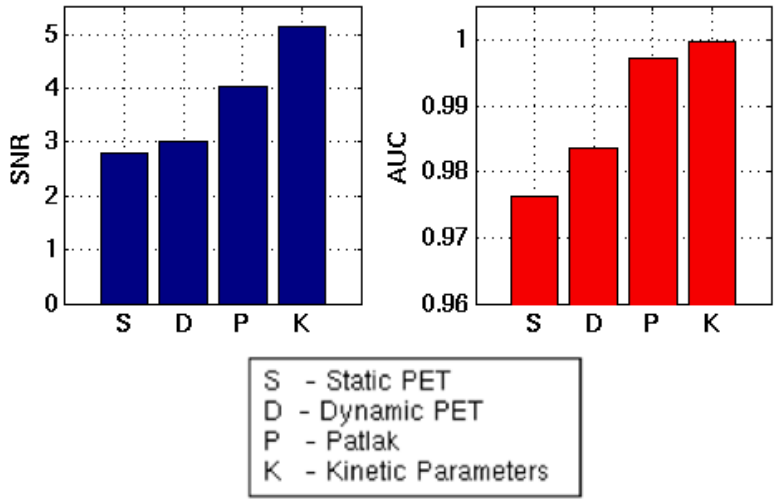

Figure 26 Detection performance comparisons of signal-to-noise ratio (SNR) and the area under the receiver operating characteristic curve (AUC) based on 1) static (S), 2) dynamic (D), 3) Patlak graphical analysis (P), and 4) parametric (K) PET images.

6.7 Discussion

This clinical study has shown that the assessment of lesion detectability on the kinetic parametric approach provides superior performance over the Patlak graphical analysis, dynamic, and static images. The proposed numerical observer appropriately integrated the information in kinetic parametric images, including the signal profiles and the pertinent noise in the images.

Interestingly, the noise embedded in the different approaches (i.e., static, dynamic, Patlak, and kinetic parametric) originates from different sources; however, the detection SNRs of different methods are reasonable as expected. As known, the noise of PET images originates from several different sources, such as the variability of quantum noise in the imaging process, the anatomical variability in the ensemble subjects, and the correlation structure of image reconstruction process. Because the parametric images (i.e. Patlak and kinetic parametric) are estimated from the dynamic PET images, the noise embedded in PET images has impact on the parametric images. The parametric images not only contain the effect of the aforementioned sources of noise, but they also have the pertinent noise arising from the model estimation processes (i.e., straight line fitting and compartmental model fitting processes). This indicates that the proposed observer computes the variability of the information in kinetic parametric images appropriately.

By investigating the contributed signals, the parametric k_3 image volume mainly dominated to the overall SNR of kinetic parametric images. The signal-to-noise ratios from individual images without combining the information from other parameters were computed. Typically, these individual SNRs were computed from the 3D-CHO stage of each kinetic parametric image volume (or each of dynamic image volume). Table 13 illustrated the contributed SNR in the PET (last five image frames), Patlak, and kinetic parametric images. Figure 24 showed the contributed percentage of the signal dominated in the kinetic parametric images of K_1, k_2, and k_3. This evidence confirms that k_3 mainly dominated approximately 72.0% to the overall signal-to-noise ratio from the proposed SNR, whereas K_1 and k_2 dominated to the proposed SNR by 20.0% and 8.0%, respectively. This indicates that the detection SNR mainly obtained the signal from the

phosphorylation of FDG due to the parameter k_3 referred to the rate constant of the entire glycolysis process of the glucose metabolism in the tumor.

Table 13 Contributed Signal-to-Noise Ratio in the PET, Patlak, and kinetic parametric images.

Method	Individual SNR					Proposed SNR
PET	N_{F-4}	N_{F-3}	N_{F-2}	N_{F-1}	N_F	3.02
	2.20	2.56	2.70	2.82	2.80	
Patlak	K_i					4.02
	4.02					
Kinetic Parameters	K_1	k_2		k_3		5.14
	1.41	0.57		5.04		

N_F is the last frame of the dynamic PET images. N_{F-1}, N_{F-2}, N_{F-3}, and N_{F-4} refer to the consecutive frames before the last frame, respectively.

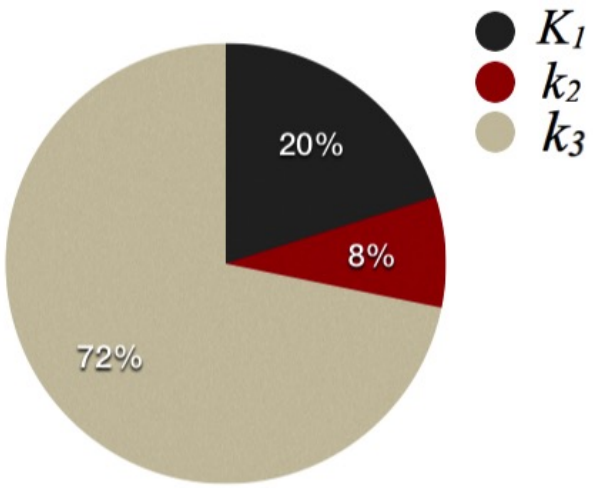

Figure 27 The contributed percentage of the signals dominated to the proposed SNR in the kinetic parametric images of K_1, k_2, and k_3.

For all the investigated approaches, it is suggested to improve the experimental results with relatively high AUCs (ranging from 0.97 to 1.00) by adding the noise to the investigated data. Because the target tumors in this study obtained from the real diseased patients, most tumors appear very high uptake of FDG. Thus, the target tumors are fully obvious and it is rather easy to

identify the pathology. In the observer analysis of an imaging method, a set of images that demonstrates abnormal pathology should be marginally visualized. The recommendation is to add Poisson noise into sinogram data before image reconstruction. This method can increase variability to the investigated images and result realistically marginal detection tasks.

6.8 Chapter Summary

This chapter demonstrated the clinical study of the assessment of lesion detection on kinetic parametric images using the proposed observer method. The lesion-detection performance was evaluated using 12 head-and-neck patients acquired with dynamic ^{18}F-FDG PET. The volume series of OSEM reconstructed images were analyzed to estimate kinetic parametric images using an irreversible two-compartment model with image-derived input functions. The SKE/BKE task of lesion detection was performed to the detection SNRs were computed. The lesion detectability was compared among static, dynamic, Patlak, and kinetic parametric images. The proposed observer approach has shown the appropriate SNR computation, which properly integrates the complex information in kinetic parametric images. Lesion detectability on kinetic parametric volume exceeded alternative analyses.

Chapter 7

Atherosclerotic Plaque Classification in Spectral CT

The purpose of this chapter is to describe the application of the proposed numerical observer to spectral CT imaging. The first section explains the overview of the current status of the research study. Then, the methodology of the research study will be described including data generation with anthropomorphic digital phantoms, insertion of carotid plaque features, and CT systems for comparison. The following sections of the performance comparison of discrimination tasks on SKE/BKE and SKS/BKE will be then demonstrated.

7.1 Introduction

Spectral computed tomography (SCT) generates better image quality than conventional CT. It has overcome several limitations for imaging atherosclerotic plaque. However, literature evaluating the performance of SCT based on objective image assessment is very limited for the task of discriminating plaques. In this work, the author applied the proposed novel

numerical-observer method to assess performance on discrimination vulnerable-plaque features, and compared the performance among multi-energy CT (MECT), dual-energy CT (DECT), and conventional CT methods.

In this chapter, the author applied the proposed numerical observer that incorporated multiple spectral information and a quantitative FOM, which could be used in the material discrimination for evaluating spectral CT imaging systems. Specifically, the proposed numerical observer accounted for all spectral information, not limited only to two energy spectra but rather incorporating several multiple energy spectra. In addition, our recent study demonstrated that the use of additional signal information in numerical observers could lead to more accurate image assessment [104, 132, 133]. These studies encouraged us to apply the proposed numerical observer to evaluate the discrimination performance using spectral CT images incorporating the extra spectral information. This proposed method could be used to evaluate the maximal performance obtained using the spectral CT technology, whose additional spectral information enhances the material characterization.

As the two-processing stage design, the proposed numerical observer could incorporate and evaluate all spectral information in Spectral CT imaging. First, each energy-window domain was preprocessed by a set of localized Channelized Hotelling Observers (CHO). In this step, the spectral image in each energy bin was decorrelated using localized prewhitening and matched filtering with a set of Laguerre-Gaussian channel functions. Second, the series of the intermediate scores computed from all the CHOs were integrated by a Hotelling Observer with an additional prewhitening and matched filter. The overall signal-to-noise ratio (SNR) and the area under the receiver operating characteristic curve (AUC) were obtained, yielding an overall discrimination performance metric.

The performance of the proposed observer was evaluated for the particular binary classification task of differentiating between alternative plaque characterizations in carotid arteries. A clinically realistic model of signal variability was also included in our simulation of the discrimination tasks. The inclusion of signal variation is key to applying the proposed observer method to spectral CT data. Hence, the task-based approaches based on the SKE/BKE framework and the clinical-relevant SKS/BKE framework were applied for analytical computation of FOM. The carotid-plaque discrimination task of deciding which of the two plaque features (e.g., calcified plaque, fatty-mixed plaque) present in a known background was performed. The plaque discrimination tasks were: 1) the SKE/BKE framework and 2) the SKS/BKE framework. Basically, the SKE/BKE task is widely used due to its convenience and simplicity as the signal is assumed to be a known deterministic entity to the observer, i.e., all parameters characterizing the signal location, size, shape, and known properties of the background noise. Unlike the SKE/BKE paradigm, the SKS/BKE paradigm is able to mimic clinical-oriented scenarios as the signal incorporates randomness through a statistically-defined distribution and associating parameters not known to the observer (e.g., with signal variability in plaque diameters or concentrations) [53].

In this study, the plaque feature present in the carotid vulnerable region was defined as a circular shape and its diameter was varied as a Gaussian-distributed function. The observer decided which of the two material hypotheses was true at a known location in each signal uncertainty. This SKS/BKE model incorporated the signal uncertainty yielded a more clinically relevant task for quantitative assessment of the spectral CT systems. This approach corresponded to the clinical practice of plaque imaging, as with the degree of stenosis or variation in

intraluminal diameters of the plaque possibly altered and task performance assessed as a function of changes of tube voltage levels in CT imaging [30].

Simulated data of a carotid-atherosclerosis patient were used to validate our methods. The author used an XCAT anthropomorphic digital phantom and three simulated plaque types (i.e., calcified plaque, fatty-mixed plaque, and iodine-mixed blood). The images were reconstructed using a standard FBP algorithm for all the acquisition methods and were applied to perform two different discrimination tasks of: 1) calcified plaque vs. fatty-mixed plaque and 2) calcified plaque vs. iodine-mixed blood. MECT, DECT, and conventional CT systems were compared for all cases of the SKE/BKE and SKS/BKE tasks.

7.2 Overview of Methodology

The validation of our approach was performed using simulated data. A digital anthropomorphic phantom (i.e., XCAT) was used to generate attenuation coefficient maps together with vulnerable carotid plaques. The plaque features with known compositions, including calcification, fat mixed (non-calcification), and iodine mixed, were separately generated and inserted into the vulnerable carotid plaques of the phantom background. Poisson-distributed noise was added to the projected sinograms, which were reconstructed to be investigated images using the filtered backprojection (FBP) algorithm. The classification performance was compared among the multi-energy (photon counting), dual-energy (dual-source, kVp-switching), and conventional (80, 120, 140 kVp) CT systems at equivalent dose.

7.3 Data Generation

The simulated data of a carotid atherosclerosis patient were used to validate the proposed numerical observer on the discrimination assessment framework. Figure 28 schematically illustrates the flow chart of the spectral CT image generation. The energy-dependent attenuation maps of the patient anatomy and vulnerable plaque in a carotid artery were generated using a digital anthropomorphic phantom. The specific plaque features were generated and then inserted into the vulnerable region in a carotid artery. Then, attenuation sinograms were created using a forward projector for fan-beam transmission tomography with realistic CT source spectra. Poisson-distributed noise was added to the sinograms and the CT images were reconstructed using FBP algorithms.

7.3.1 Anthropomorphic phantom

An extended Cardiac-Torso (XCAT) digital phantom was used to generate spectral attenuation coefficient $\mu(E,\vec{r})$ at position $\vec{r}$ of the patient anatomy. The attenuation maps of the anatomical background (denoted $\mu_{BG}(E,\vec{r})$) together with the attenuation maps of vulnerable plaque (denoted $\mu_{VP}(E,\vec{r})$) were generated using XCAT. Specifically, the $\mu_{VP}(E,\vec{r})$ were created by using the cardiac plaque generator available in XCAT version 2.0. The details of the chemically element compositions and densities were not specified, but the generated $\mu_{VP}(E,\vec{r})$ was realistic because the XCAT incorporated the parameterized models of humans, developed with highly detailed anatomies using nonuniform rational B-spline (NURBS) and the Visible Male/Female anatomical datasets provided by the National Library of Medicine [111]. The carotid artery's location was selected at the origin level located in the neck above the

brachiocephalic trunk of the right common carotid artery (CCA), which its average arterial diameter was approximately 9.1 ± 0.2 mm [134]. The $\mu_{VP}(E,\bar{r})$ were inserted into the lumen of the carotid artery present in an axial slice of the generated phantom. Figure 29(a) and 29(b) show the selected axial slice that has the presence of the carotid arteries in the XCAT phantom. Figure 29(c) shows an example of the attenuation map at energy 30 keV of the selected slice with a zoomed carotid lumen. The phantom pixel size of 1.03 × 1.03 mm^2 with the matrix size of 512 × 512 was used for these simulated data. The 8-mm diameter of circular-shaped vulnerable plaque was inserted into the carotid lumen, treated as a particular vulnerable plaque was accumulated within the carotid lumen.

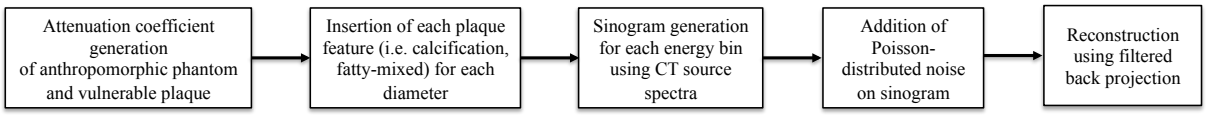

Figure 28 Flow chart of the spectral CT image generation.

7.3.2 Carotid Plaque Features

The circular-shaped plaque features with known compositions were inserted within the vulnerable-plaque region of the carotid artery, as shown in a schematic model in Figure 30(a). The different models of the plaque features were generated including: 1) calcified nodule (CN), 2) fatty-mixed nodule (FN), and 3) iodine-mixed blood (IB) in the vulnerable plaque.

The energy-dependent attenuation coefficients of each feature model were separately generated, regardless the generation using XCAT. According to the mixture rule of Lambert-Beer's Law, compound matter could be described as a superposition of element mass attenuation coefficients. Thus, the spectral attenuation coefficient $\mu_x(E)$ in the units of cm^{-1} was obtained as:

$$\mu_x(E) = \sum_{i=1}^{M} \mathrm{P}_i \left(\frac{\mu}{\rho} \right) (E, Z_i), \tag{22}$$

where the mass attenuation coefficient $(\mu/\rho)(E, Z_i)$ is a characteristic function of the *i*-th element indexed by the atomic number Z_i in the periodic table of elements and P_i is the partial density or concentration in g/cm^{-3} of the *i*-th element, and *M* is the number of elements in the compound matter [94, 135].

For each plaque-feature model, the attenuation map was generated using Eq. (22) with the element compositions and densities illustrated in Table 14 [136]. The energy-dependent mass attenuation coefficients, $(\mu/\rho)(E, Z_i)$, of each element were obtained from the National Institute of Standards and Technology (NIST) tables [137]. Figure 30(b) and 30(c) show the attenuation maps of the inserted plaque features in the vulnerable-plaque region for a fatty-mixed nodule and a calcified nodule, respectively. Figure 31 depicts the generated attenuation coefficients as a function of energies for the vulnerable plaque, the calcified nodule, the fatty-mixed nodule, and the iodinated-blood nodule.

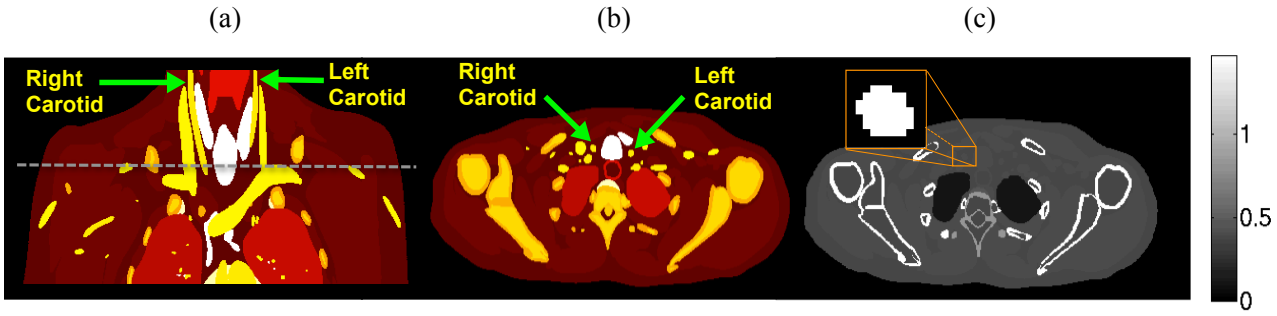

Figure 29 (a) An anthropomorphic torso phantom shows the right and left carotid arteries in the coronal plane. The *dashed horizontal line* marks the location of the axial slice to be measured. (b) The selected axial slice of the anthropomorphic torso phantom shows the right and left carotid arteries, and (c) the generated attenuation map of the anthropomorphic torso phantom (cm^{-1}) displays on the selected slice at energy 30 keV. The zoomed window shows the right carotid artery.

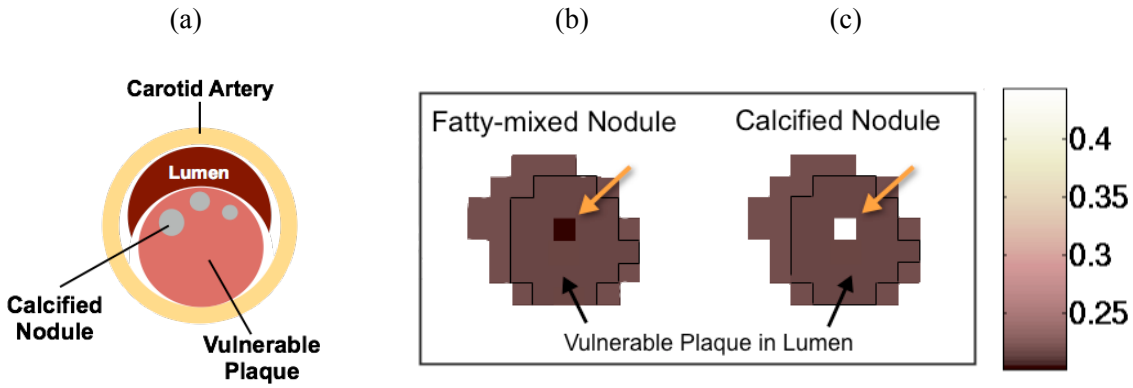

Figure 30 (a) the schematic diagram of the carotid atherosclerosis model. The XCAT attenuation maps (cm^{-1}) at 30 keV of (b) the inserted fatty-mixed and (c) calcified nodules in the vulnerable plaque within the right carotid artery.

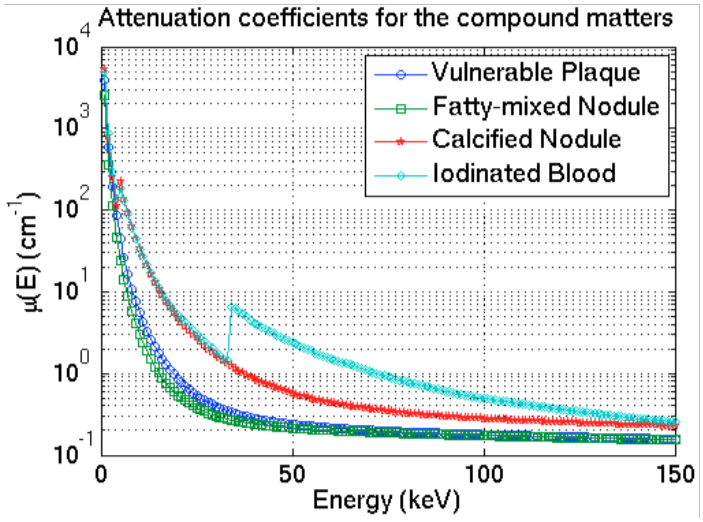

Figure 31 The attenuation coefficient $\mu(E)$ as a function of energies for the simulated vulnerable plaque, the inserted features of calcified nodule, fatty-mixed nodule, and iodinated blood nodule. These $\mu(E)$ were generated using Lambert-Beer's Law for the superposition of element mass attenuation coefficients.

Table 14 Element Compositions and densities (ρ) of calcified, fatty-mixed, and iodinated-blood nodules [136].

		H	C	N	O	P	Cl	Ca	I	ρ (g/cm3)
	Atomic Number (Z)	1	6	7	8	15	17	20	53	
	Atomic Weight (A)	1.01	12.01	14.01	16.00	30.97	35.45	40.08	126.90	
	Tissue Substitutes	Elemental Compositions (percentage by mass)								
1	Calcified Nodule (CB2-50% CaCO3)	4.8	41.6	1.5	32.0	0.0	0.1	20.0	0.0	1.560
2	Fatty-Mixed Nodule	9.1	72.2	2.3	16.3	0.0	0.1	0.0	0.0	1.049
3	Iodine-Mixed Blood	10.2	11.0	3.3	74.5	0.1	0.3	0.0	20.0	1.060

7.3.2.1. Simulated Sinograms and Image Reconstructions

The CT measurement was simulated based upon the geometry of a GE LightSpeed CT scanner (GE Healthcare, Milwaukee, Wisconsin), which has fan-beam transmission tomography with an arc detector. The attenuation sinograms were obtained using a Fourier-based forward projector

[138]. The fan-beam sinogram size was 888 samples in the angle of the ray relative to the source (σ), spaced by $\Delta\sigma \approx 0.06°$ and 984 source positions (ξ) over 360°. The source-to-detector distance was approximately 949 mm. The isocenter-to-detector distance was approximately 408 mm. A quarter-detector offset was also included to reduce aliasing. The effective width of the arc detector varied from 0.22 mm to 0.64 mm over a 40 cm field of view.

A measured projection, $p(\xi)$, having the intensity of X-rays passed through an object with the energy dependence of the attenuation coefficient, $\mu(\xi,\eta,E)$, along the path *s* in the spatial coordinate, η, could be expressed as:

$$p(\xi) = -\ln\left(\frac{1}{I_0}\int_{E_0}^{E_{TH}} S(E)D(E)e^{-\int_0^s \mu(\xi,\eta,E)d\eta}\,dE\right), \tag{23}$$

where $I_0 = \int_{E_0}^{E_{TH}} S(E)D(E)dE$ is the blank measurement, $S(E)$ is the X-ray source spectrum, and $D(E)$ is the detector response. For an ideal integrating detector, we could assume $D(E) = E$ [60, 135]. Note that $(E_0, E_{TH}) \in [0, E_{\max}]$ for energy integrating detectors and $(E_0, E_{TH}) \in [E_{lower}, E_{upper}]$ for multi-energy CT with the lower threshold, E_{lower}, and the upper threshold, E_{upper}, for each energy bin were assigned in the simulation.

Poisson-distributed noise was added to the generated sinograms to simulate statistical fluctuations in the measurement before the image reconstruction. The noisy fan-beam sinograms were reconstructed using a conventional FBP reconstruction algorithm alternatively with Ramp or Hanning (the cut-off frequency at 0.6) filter kernels [138]. The reconstructed image pixel size was 0.98 × 0.98 mm^2 with the matrix size of 512 × 512. The CT images were reconstructed for

each plaque feature separately, assumed that the plaque feature was perfectly decomposed from the mixture materials, so that only one plaque feature was present in the modeled region.

7.4 CT Systems for Comparison

The discrimination assessment of plaque features was compared among various CT systems including:

1) a conventional CT system operated at 80 kVp (CT-80kVp),

2) a conventional CT system operated at 120 kVp (CT-120kVp),

3) a conventional CT system operated at 140 kVp (CT-140kVp),

4) a dual-energy CT system based on dual-source CT using 80 and 140 kVp sources (DECT-DS),

5) a dual-energy CT system based on rapid-kVp-switching CT using 80 and 140 kVp sources (DECT-SW), and

6) a multi-energy CT system based on photon-counting detectors with a source operated at 120 kVp (MECT-PC).

For all the CT systems, the source spectra were generated using SPEKTR [139]. Figure 32 and Table 15 illustrate the PDF of photon flux as a function of energy (keV) and the details of the X-ray spectra for each CT system, respectively. As illustrated, the lower energy spectrum mainly consisted of Bremsstrahlung, while the higher energy spectrum included the characteristic lines of the tungsten anode. For all the investigated modalities, the source spectra were normalized to deliver the same amount of dose to the patient phantom. The total entrance skin exposures applied to the phantom for all the CT systems were the same with X-ray exposure of 20 mR entrance skin per projection. With the same phantom and the same detector geometry being used,

the amount of dose was matched for all CT systems [140]. In practice, this was equivalent to adjusting the tube current (mAs) to deliver the same total number of X-ray quanta. In the simulation, there were 10^4 to 10^6 quanta for an I_0 measurement.

For DECT-DS, an additional tin (*Sn*) filtration of 1.0 mm at 140 kV was applied to increase the spectral separation between the low- and the high-energy spectra as well as to narrow the 140-kV spectrum [61, 141]. For both DECT-DS and DECT-SW, the X-ray exposure from both tubes matched that of a single-source CT protocol, with the dose ratio of the low- and high-energy spectra set to 19:1. By performing the experiment, this ratio was chosen empirically to maximize the discrimination performance of DECT. Due to the fact that the lower energy photons carry larger contrast between different materials than higher energy photons [68], a larger fraction was given to the low-kVp source rather than the high-kVp source. The MECT-PC system separated detected photons into five different energy bins with upper thresholds at 33, 49, 65, 80, and 120 keV, which were selected to exploit the K-edge of iodine while the rest of the energy thresholds chosen for a nearly equal number of counts contained in each bin, following the work by Baturin *et al*. [33]. The mean energies of the kV spectra were 41.80, 52.51, 56.47, 41.80(98.14), 41.80(52.51), and 52.51 keV for CT-80kVp, CT-120kVp, CT-140kVp, DECT-DS, DECT-SW, and MECT-PC, respectively. For all the CT systems, projection data were simulated with energy-weighted integrals over 1 keV spectral steps. For MECT-PC, the multi-energy sinograms were acquired and reconstructed for each energy bin. Although data acquired at each energy (either within a bin of photon-counting detectors or at a single tube-voltage setting) were treated as independent measurements, a high degree of correlation among these energy-specific datasets was achieved due to the exactly same patient anatomy was measured in each case [35]. Two independent measurements with and without the object (blank scans) were acquired for

each CT method for a population of 50 noise realizations. As is ideal, the simulation and analyses were performed on an ensemble of the reconstructed images from the same phantom under identical scan conditions, in order to remove the impact of the correlated nature of the CT image noise as well as to remove the potential biases due to image artifacts resulting from the imperfect system calibration [95].

To demonstrate the method, several assumptions were made for the CT systems in the observer performance comparison. For all the CT systems, the detector response was assumed to provide 100% quantum detection efficiency. For DECT-SW, the actual tube voltage was assumed to yield the ideal rectangular switching curve. As a result, there was no overlapping of data acquisition from the under- and overshoot of the X-ray tube voltage during switching processes. For MECT-PC, the photon counting detectors were assumed to have perfect energy resolution with no charge sharing and pulse pile-up effects, and therefore no distortions in the detected spectrum.

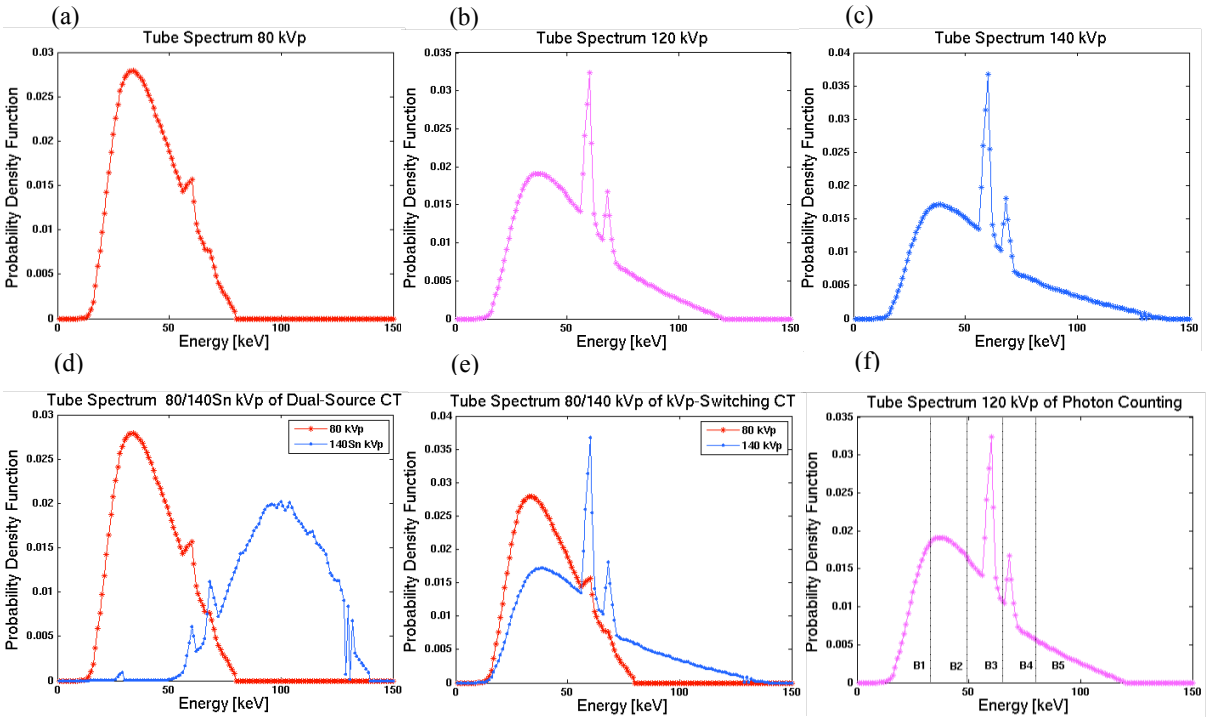

Figure 32 The probability density function of photon flux as a function of energy (keV) of X-ray spectra generated by SPEKTR: (a) the tube spectrum of CT-80kVp, (b) the tube spectrum of CT-120kVp, (c) the tube spectrum of CT-140kVp, (d) the tube spectrums of DECT-DS, (e) the tube spectrums of DECT-SW, and (f) the tube spectrum of MECT-PC systems. Vertical dashed lines in (f) represent energy bin thresholds assigned as 33, 49, 65, 80, and 120 keV.

Table 15 Tube spectrum information [139].

Tube Spectrum	**Exposure** (mR/mAs at SAD)*	**Fluence/Exposure** (X-rays/mR/mm^2)	**Mean Energy** (keV)
80 kVp	9.70	193,578	41.80
120 kVp	19.12	224,812	52.51
140 kVp	24.37	229,793	56.47
140 kVp with Sn 1.0 mm	1.00	237,155	98.14

*mR = milli-roentgen (described X-ray exposure), mAs = milli-amphere (described tube current), SAD is the distance from the fan-beam vertex to the center of rotation.

7.5 Performance Evaluation

The observer performance was evaluated for two discrimination tasks: 1) calcified plaque vs. fatty-mixed plaque (DT-1) and 2) iodinated blood vs. calcified plaque (DT-2) on the reconstructed images, using FBP with Ramp and Hanning kernels. In these defined tasks, the first scenario was equivalent to the identification task for calcified in non-contrast imaging. The second scenario was equivalent to the identification task for calcified plaque when using iodinated contrast agent. However, the discrimination task for fatty-mixed plaque and iodinated blood was not included in this study because it is known in the field it is straightforward to distinguish these two materials in spectral CT (both in DECT and MECT) [61, 142]. The indistinguishability of these two materials can occur in conventional CT, and we here focus on spectral CT performance, rather than the performance of conventional CT.

Feature-to-vulnerable-background contrasts (C_F) for calcified nodule, fatty-mixed nodule, and iodinated-blood nodule were calculated. First, the ROI of an 11×11 window centered on each plaque feature was defined in the reconstructed CT image. This ROI was then divided into two sub-regions: a 4×4 ROI centered on the plaque feature (denoted ROI_{PF}), and a surrounding 7×7 ROI shell (denoted ROI_{VPB}), treated as the vulnerable-plaque background for that particular plaque feature. The contrast metric was computed as the average over N_R noise realizations:

$$C_F = \frac{1}{N_R}\sum_{r=1}^{N_R}\hat{C}_F^r , \tag{24}$$

where $\hat{C}_F^r = \dfrac{avg\left(\mathrm{ROI}_{PF}^r\right)}{avg\left(\mathrm{ROI}_{VPB}^r\right)}$ for each noise realization r. Note that $avg(\mathrm{ROI}_x^r) = \dfrac{1}{Q}\sum_{i\in \mathrm{ROI}_x^r}\gamma_i^r$ is the average intensity value of the total number of Q pixels inside the ROI for noise realization r.

Feature contrast ratios (CR_F) of the images – defined as a contrast ratio of the material-paired combinations described in the identification task of DT-1 and DT-2 – were computed.

The appropriate numerical observers were selected to match with the dimensionality of the investigated images. In this study, the simulated images in each energy window of MECT (or integrated energy) were in the $\Re^2$ domain resulting the image dimensionality in 2D+*e*. Hence, the channel functions and the preprocessing CHO were formed in $\Re^2$ for this study. For CT-80kVp, CT-120kVp, and CT-140kVp, the observer evaluation was performed using a conventional 2D CHO model. For DECT-DS and DECT-SW, the proposed numerical observer with two energy bins (J = 2) was used, and one with five energy bins (J = 5) was used for MECT-PC. The ROI of a 31×31 window centered on a target plaque feature for a pair of investigated materials were input to a numerical observer. The different window size of the investigated material did not alter the FOM results. The material identification was performed on the given the plaque features for the discrimination tasks of DT-1 and DT-2. For all the CT methods, the plaque discrimination was evaluated for:

- *Performance comparison of discrimination task on SKE/BKE*: the diameter of the signal (ϕ) was constant at 1.8 mm, referred to constant plaque density or concentration.
- *Performance comparison of discrimination task on SKS/BKE*: the diameter of the signal was increased as a Gaussian-distributed function, $\phi \in [2.3,\ 7.1]$ mm, referred to changes of plaque density or concentration. Note that the diameter of 1.8-mm plaque was not included here because this task was already performed in the previous experiment. In principle, the SKS task is the extended paradigm of the SKE, in which the observer performs multiple SKE tasks with varying target diameters.

The figure-of-merits of SNR and AUC for the two discrimination tasks of DT-1 and DT-2 were computed using Eqs. (12) and (14). The discriminated SNR per a unit of dose (SNR_{DIS}) was computed as:

$$SNR_{DIS} = SNR/\sqrt{D}, \tag{25}$$

where D is the total skin exposure [33, 60].

For SKS/BKE, according to the outcome AUC range in Eq. (14) was limited by the Gaussian error function, where the SNRs of all the varied signals were first obtained using Eq. (12) for all the CT modalities. Consequently, the SNRs of all the varying signals and for all the CT systems were converted to a certain range that approximately fitted the criterion of AUC, covering the range from 0.5 to 1.0, prior input to Eq. (14). With this conversion, it improved the analysis investigation of the performance comparison for all the investigated CT systems.

7.6 Results

7.6.1 Simulation Results

The plaque-feature discrimination tasks were performed on simulated images reconstructed for different CT systems (i.e., CT-80kVp, CT-120kVp, CT-140kVp, DECT-DS, DECT-SW, and MECT-PC) and different reconstruction parameters (i.e., FBP-Ramp and FBP-Hanning), as shown in Figure 33. As expected, the reconstructed images using FBP-Ramp were noisier than those reconstructed using FBP-Hanning for all CT systems. For both the reconstructed parameters, the image intensities of the lower energy spectra (or energy bins for MECT) were brighter than those of the higher energy spectra, when comparing within the same type of the acquisition method (i.e., among three conventional CTs or between the low- and high-energy

kVp for DECT or among energy bins for MECT). As expected, more beam hardening artifacts in the form of shading and streaking artifacts were found at lower energy bins.

Table 16 and Table 17 show C_F for the CN, FN, and IB features obtained using FBP-Ramp and FBP-Hanning, respectively. FBP-Ramp yielded similar C_F means as FBP-Hanning for all features. However, the standard deviations (std) of C_F appeared higher for FBP-Ramp as compared to FBP-Hanning. For the conventional CT simulations, CT-80kVp yielded higher C_F than both CT-120kVp and CT-140kVp for the CN and IB features. Similar results were also observed in MECT-PC, as the lower energy bins yielded higher C_F than did the higher energy bins. These results were consistent with the previous study performed by Saba *et al*. [28]. However, we did not see this characteristic for the FN feature, as the $C_{F\text{-}FN}$ for all energy spectra for all CT systems were not very different. Energy bins j = 2 of DT-2 were the highest as compared to other energy bins for MECT-PC in both reconstructed images.

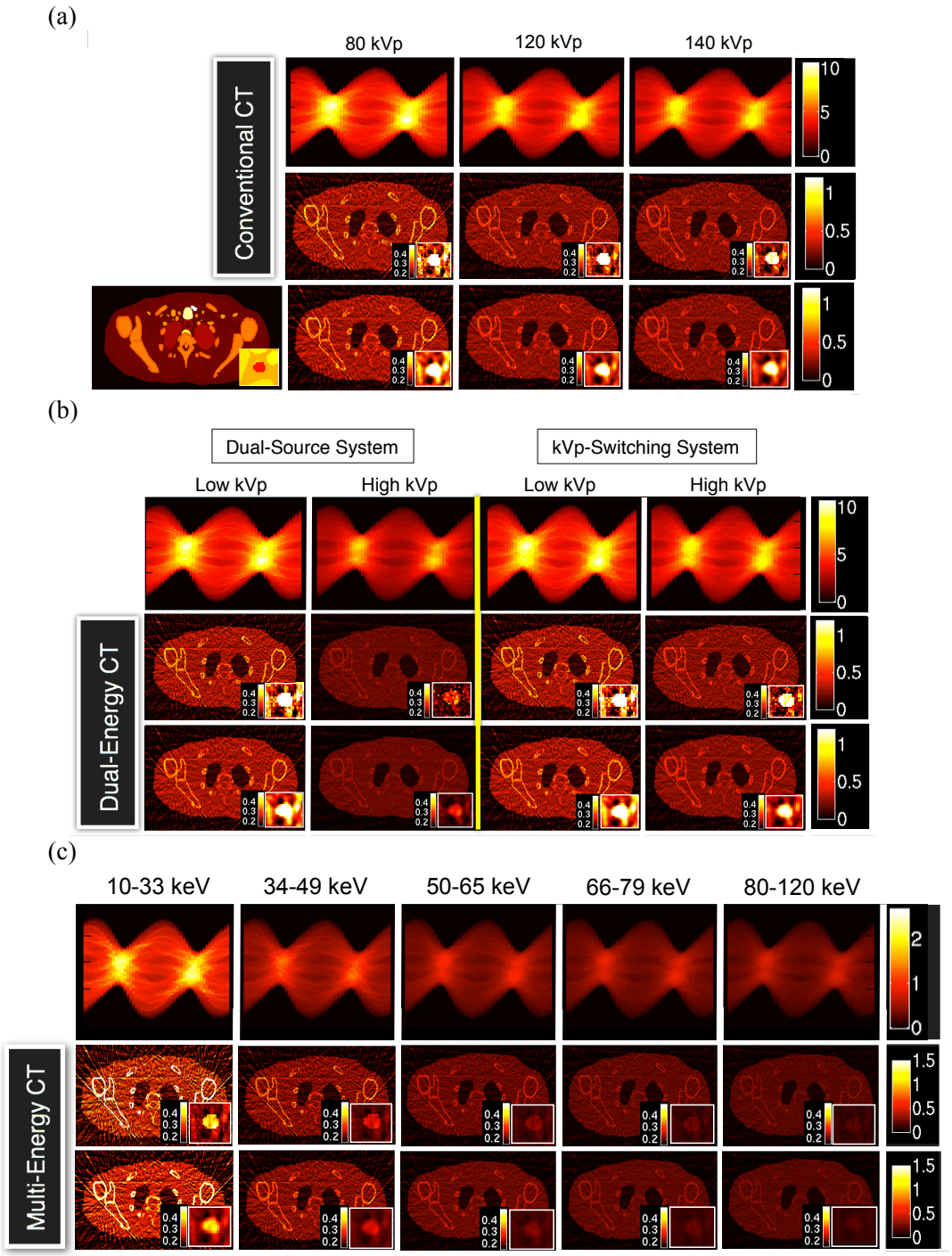

Figure 33 The generated fan-beam sinograms and reconstructed images using the FBP reconstruction method for Ramp and Hanning filters: (a) the conventional CT with 80, 120, and140 kVp (denoted CT-80kVp, CT-120kVp, and CT-140kVp, respectively); (b) the dual-energy CT of dual-source CT (denoted DECT-DS) and rapid kVp switching CT (denoted DECT-SW); and (c) the multi-energy CT using photon-counting detector (denoted MECT-PC). The carotid calcified plaque of 8-mm diameter is displayed at the bottom right corner of each image. The ground truth image (XCAT) is displayed at the lower left in (a).

Table 16 The feature-to-vulnerable-background contrasts (C_F) for calcified nodule, fatty-mixed nodule, and iodinated-blood nodule of the investigated CT systems with FBP-Ramp.

CT System		**Feature-to-Vulnerable-Background Contrast (C_F)***		
		Calcified Nodule (CN)	Fatty-Mixed Nodule (FN)	Iodinated-Blood Nodule (IB)
		FBP-Ramp	**FBP-Ramp**	**FBP-Ramp**
CT-80kVp		1.3e+0±1.0e-2	9.8e-1±9.4e-3	2.3e+0±1.3e-2
CT-120kVp		1.2e+0±1.3e-2	1.0e+0±1.2e-2	2.0e+0±1.3e-2
CT-140kVp		1.2e+0±1.1e-2	1.0e+0±1.2e-2	1.9e+0±1.4e-2
DECT-DS	$j = 1$	1.3e+0±1.0e-2	9.8e-1±1.2e-2	2.3e+0±1.3e-2
	$j = 2$	1.8e+0±4.5e-2	1.3e+0±3.5e-2	3.1e+0±6.1e-2
DECT-SW	$j = 1$	1.3e+0±1.0e-2	9.8e-1±1.2e-2	2.3e+0±1.3e-2
	$j = 2$	1.5e+0±3.0e-2	1.1e+0±2.7e-2	2.6e+0±6.1e-2
MECT-PC	$j = 1$	1.6e+0±2.4e-2	9.0e-1±1.8e-2	1.6e+0±1.9e-2
	$j = 2$	1.3e+0±1.8e-2	9.6e-1±1.6e-2	3.1e+0±2.7e-2
	$j = 3$	1.2e+0±2.1e-2	1.0e+0±1.9e-2	1.9e+0±2.2e-2
	$j = 4$	1.1e+0±3.0e-2	1.0e+0±3.6e-2	1.6e+0±3.5e-2
	$j = 5$	1.0e+0±3.1e-2	1.0e+0±3.1e-2	1.3e+0±3.0e-2

*Each C_F was in the format as mean ± standard deviation (std), where std was computed over the contrasts of 50 noise realizations.

Table 17 The feature-to-vulnerable-background contrasts (C_F) for calcified nodule, fatty-mixed nodule, and iodinated-blood nodule of the investigated CT systems with FBP-Hanning.

CT System		**Feature-to-Vulnerable-Background Contrast (C_F)***		
		Calcified Nodule (CN)	Fatty-Mixed Nodule (FN)	Iodinated-Blood Nodule (IB)
		FPB-Hanning	**FBP-Hanning**	**FBP-Hanning**
CT-80kVp		1.3e+0±0.5e-2	1.0e+0±0.4e+2	2.2e+0±0.6e-2
CT-120kVp		1.2e+0±0.5e-2	1.0e+0±0.5e-2	1.9e+0±0.5e-2
CT-140kVp		1.2e+0±0.5e-2	1.0e+0±0.4e-2	1.9e+0±0.5e-2
DECT-DS	$j = 1$	1.3e+0±0.5e-2	1.0e+0±0.5e-2	2.2e+0±0.7e-2
	$j = 2$	1.8e+0±2.0e-2	1.4e+0±1.6e-2	3.1e+0±2.8e-2
DECT-SW	$j = 1$	1.3e+0±0.5e-2	1.0e+0±0.5e-2	2.2e+0±0.7e-2
	$j = 2$	1.5e+0±1.4e-2	1.1e+0±1.1e-2	2.6e+0±1.9e-2
MECT-PC	$j = 1$	1.6e+0±1.1e-2	1.0e+0±0.9e-2	1.7e+0±0.8e-2
	$j = 2$	1.3e+0±0.8e-2	1.0e+0±0.8e-2	3.0e+0±1.3e-2
	$j = 3$	1.2e+0±0.9e-2	1.0e+0±0.7e-2	1.9e+0±1.0e-2
	$j = 4$	1.1e+0±1.1e-2	1.0e+0±1.3e-2	1.6e+0±1.6e-2
	$j = 5$	1.1e+0±1.3e-2	1.0e+0±1.3e-2	1.3e+0±1.4e-2

Figure 34 and Figure 35 illustrate the boxplots of CR_F, the ratios of the feature contrasts for calcified plaque vs. fatty-mixed plaque ($C_{F\text{-}CN}/C_{F\text{-}FN}$) and iodinated blood vs. calcified plaque ($C_{F\text{-}IB}/C_{F\text{-}CN}$) at the diameter of 1.8 mm for DT-1 and DT-2. CR_F means were similar while CR_F stds were higher for FBP-Ramp as compared to FBP-Hanning for both DT-1 and DT-2 and for all CT systems. CR_F of DT-2 yielded higher CR_F than DT-1, as observed in both FBP-Ramp and FBP-Hanning. Similar to Table 16 and Table 17, we observed that CR_F of lower energy spectra was higher than those of the higher energy spectra, as compared among the different conventional CTs and that among different energy bins of MECT-PC, respectively. Interestingly, this observation did not appear for DT-2 for MECT-PC, as energy bin $j = 1$ and $j = 2$ yielded relatively low and high values, respectively, both in FBP-Ramp and FBP-Hanning.

7.6.2 Performance comparison of discrimination task on signal-known-exactly and background-known-exactly (SKE/BKE)

The discrimination SNRs of the plaque material identification tasks were compared among the different investigated CT systems and different reconstruction parameters, as shown in Figure 36(a) and 36(b) for DT-1 and DT2, respectively. As illustrated in Figure 36(a), the overall discrimination SNRs of all CT systems for DT-1 was inferior to that of DT-2 shown in Figure 36(b) by 32.9% and 34.7% for FBP-Ramp and FBP-Hanning, respectively. The FBP-Hanning images provided higher discrimination performance than did the FBP-Ramp images for all CT acquisition methods. Superior discrimination performance was achieved using MECT-PC over the DECT (-DS, -SW) and conventional CT (80kVp, 120kVp, 140kVp) methods for both identification tasks. Among the three conventional CTs, the discrimination SNRs decreased as

tube voltages increased. For both tasks, the observer performances of the DECT systems outperformed that of the conventional CTs.

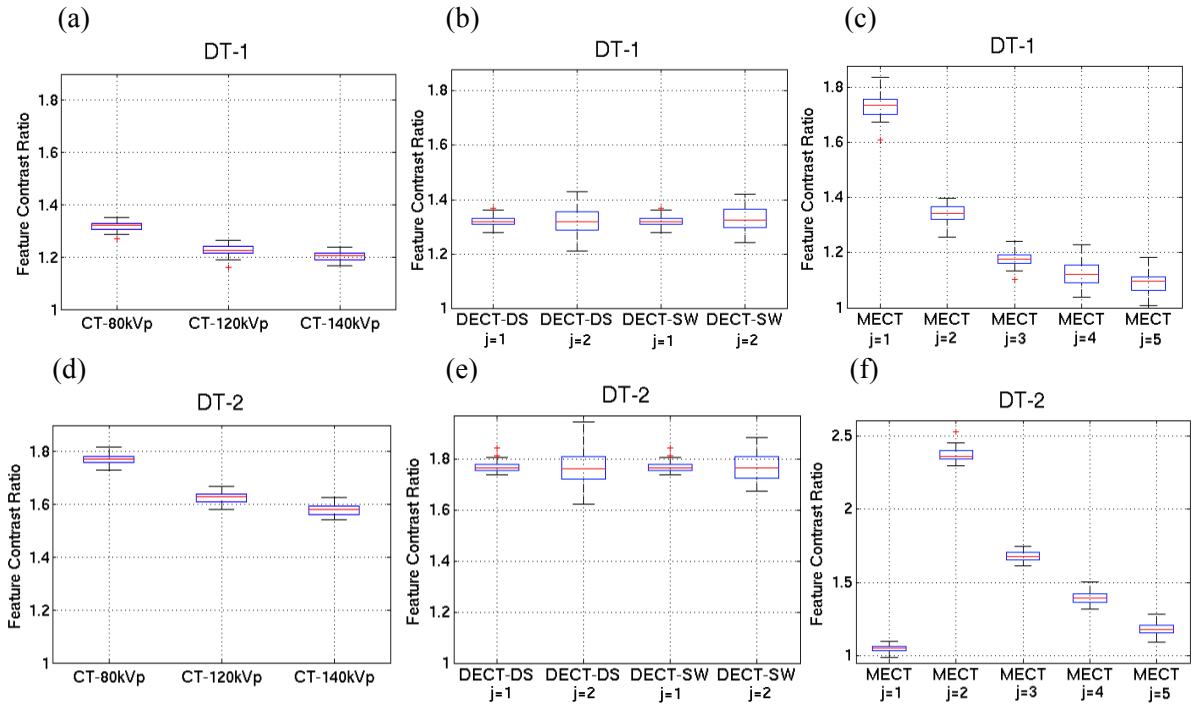

Figure 34 The boxplots illustrate the feature contrast ratios (CR_F) for the identification task of calcified plaque vs. fatty-mixed plaque (DT-1) and the identification task of iodinated blood vs. calcified plaque (DT-2) using FBP-Ramp images for: (a,d) conventional CT (CT-80kVp, CT-120kVp, and CT-140kVp), (b,e) dual-energy CT (DECT-DS and DECT-SW), and (c,f) multi-energy CT (MECT-PC).

However, the discrimination SNRs using FBP-Hanning images of both DECT systems were not as good as that of CT-80kVp for DT-2. By comparing the two dual-energy CT systems, we could not conclude which system performed better performance. The findings indicated that the multi-energy CT system yielded superior performance over other CT systems for the identification tasks of calcified plaque, fatty-mixed plaque, and iodinated-mixed blood as compared at equivalent dose.

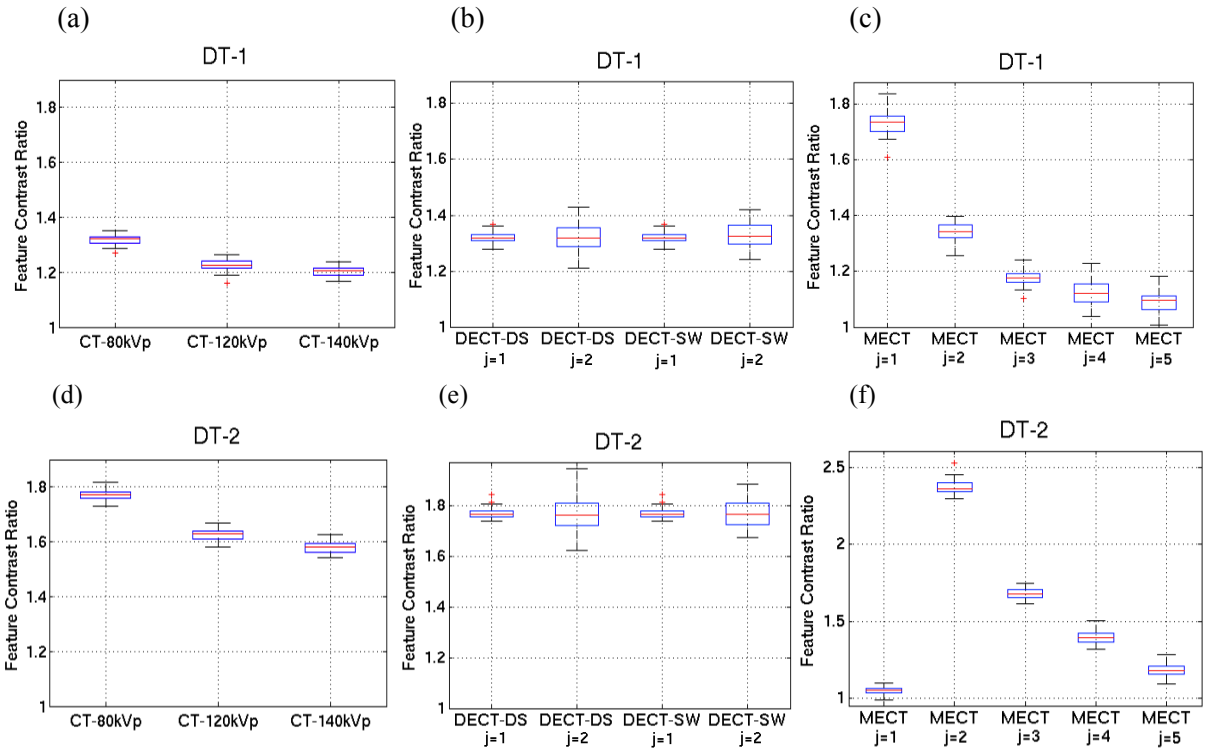

Figure 35 The boxplots illustrate the feature contrast ratios (CR_F) for the identification tasks of DT-1 and DT-2 using FBP-Hanning images for: (a,d) conventional CT (CT-80kVp, CT-120kVp, and CT-140kVp), (b,e) dual-energy CT (DECT-DS and DECT-SW), and (c,f) multi-energy CT (MECT-PC).

7.6.3 Performance comparison of discrimination task on signal-known-statistically and background-known-exactly (SKS/BKE)

The effect of mass thicknesses and diameters of Gaussian-shaped inserted plaque features were investigated in the identification tasks of DT-1 and DT-2 on the tested CT systems. All discrimination AUCs of all varied signals for DT-1 and DT-2 were computed for both reconstruction parameters. Figure 37 shows the plots of AUC as a function of signal certainty (defined as the varied diameters as a Gaussian distribution of the plaque features) for the plaque

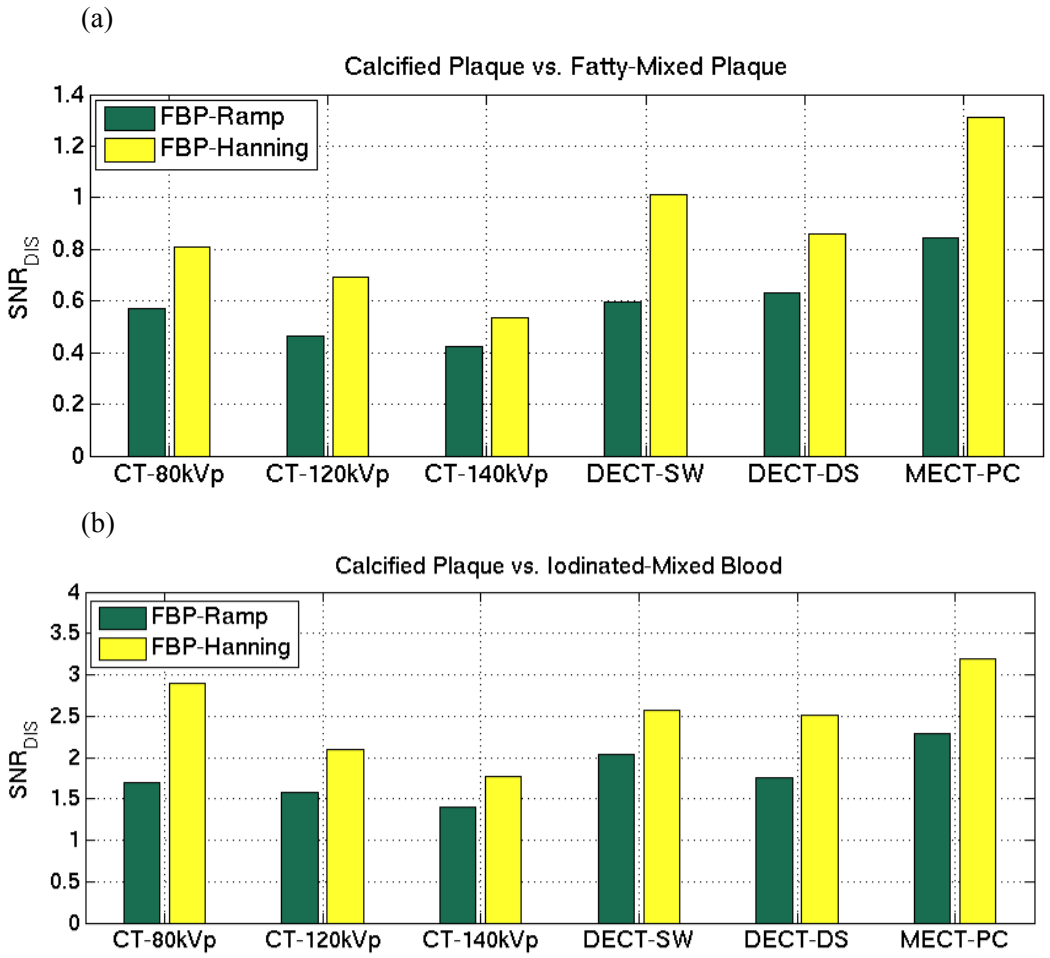

Figure 36 The discrimination SNR results per an effective dose for (a) the identification task of DT-1 and (b) the identification task of DT-2 as compared for CT-80kVp, CT-120kVp, CT-140kVp, DECT-DS, DECT-SW, and MECT-PC using the FBP reconstructed algorithm with Ramp and Hanning filters.

discrimination task using different CT systems and different reconstruction parameters. The AUC values were fitted using polynomial functions and the results were plotted. For all the investigated CT systems, the observer performance increased as the increased signal certainty, whereas MECT-PC yielded the highest performance at all levels of the signal certainties, as illustrated in both reconstruction parameters. By comparing among the conventional CTs, the higher energy-spectrum CTs (CT-120kVp, CT-140kVp) yielded almost the least performance,

whereas CT-80kVp and the dual-energy CT systems (DECT-DS, DECT-SW) provided comparable performance. Figure 37(a) and 37(c) show the discrimination AUCs for the identification tasks of DT-1 and DT-2 with the FBP-Ramp algorithm, while Figure 37(b) and 37(d) illustrate results for FBP-Hanning of DT-1 and DT-2, respectively. As expected, FBP-Ramp reconstructed images provided inferior discrimination performance than did the FBP-Hanning reconstructed images for all signal levels. With the different identification tasks, the overall AUCs of all CT systems for DT-2 were higher than those for DT-1 for both FBP-Ramp and FBP-Hanning. These results demonstrated that the multi-energy CT system outperformed other methods in discriminating carotid plaque features for all levels of signal uncertainties and reconstructed methods.

7.7 Discussion

In this study, a numerical observer incorporated multiple spectral energies and a material-discrimination framework for spectral CT assessment were proposed and evaluated. The binary-discrimination tasks of the SKE/BKE framework and the signal variability based on the SKS/BKE framework were performed in classifying the carotid-plaque features. Significant improvements in terms of observer performance for multi-energy CT were achieved as compared to dual-energy CT and conventional CT systems at an equivalent dose level.

It is clear that MECT-PC provides superior performance over the other acquisition methods for all cases. On average of signal variability, MECT-PC outperformed DECT-DS, DECT-SW, CT-80kVp, CT-120kVp, and CT-140kVp, as the SNR improvements of the classification tasks were in the range of 46.8% - 65.3% (all $p < 0.01$) for FBP-Ramp images and 53.2% - 67.7% (all $p < 0.01$) for FBP-Hanning images in both identification tasks. The SNR improvements of

MECT-PC as compared to the other modalities were calculated as illustrated in Table 18. As illustrated in Table 18, the overall improvements of FBP-Ramp were higher than those of FBP-Hanning for both identification tasks. This implies that MECT-PC can be used to improve material-discrimination performance when a reconstruction method is chosen.

Table 18 The improvement of the discrimination performance of MECT-PC as compared to other investigated CT systems on the average of signal variability.

No.	CT System	SNR Improvement of MECT-PC (%)			
		DT-1		DT-2	
		FBP-Ramp	FBP-Hanning	FBP-Ramp	FBP-Hanning
1.	CT-80kVp	65.3	47.8	63.8	53.2
2.	CT-120kVp	55.8	48.7	59.0	59.9
3.	CT-140kVp	51.2	47.0	55.8	57.9
4.	DECT-DS	62.1	46.8	64.8	54.0
5.	DECT-SW	64.1	48.5	67.7	54.8

The proposed numerical observer appropriately accounts for both signal and noise appearing in images. In this study, the noise is attributable to the measurement process (Poisson-distributed noise) and also that appeared in reconstructed images, which is pertinent to the reconstruction process. Specifically, the different noise levels using the different reconstruction parameters constitute important evidence to demonstrate that our numerical observer properly correlates the image noise that occurred in each energy bin and across different energy bins of MECT-PC (or different voltage spectra of DECT) in the FOM computation. As expected, the overall SNR of FBP-Ramp images is inferior to that of FBP-Hanning images for all cases. These indicate that our numerical observer can be used to appropriately assess and compare the overall diagnostic values of material discrimination in different CT systems and reconstructions.

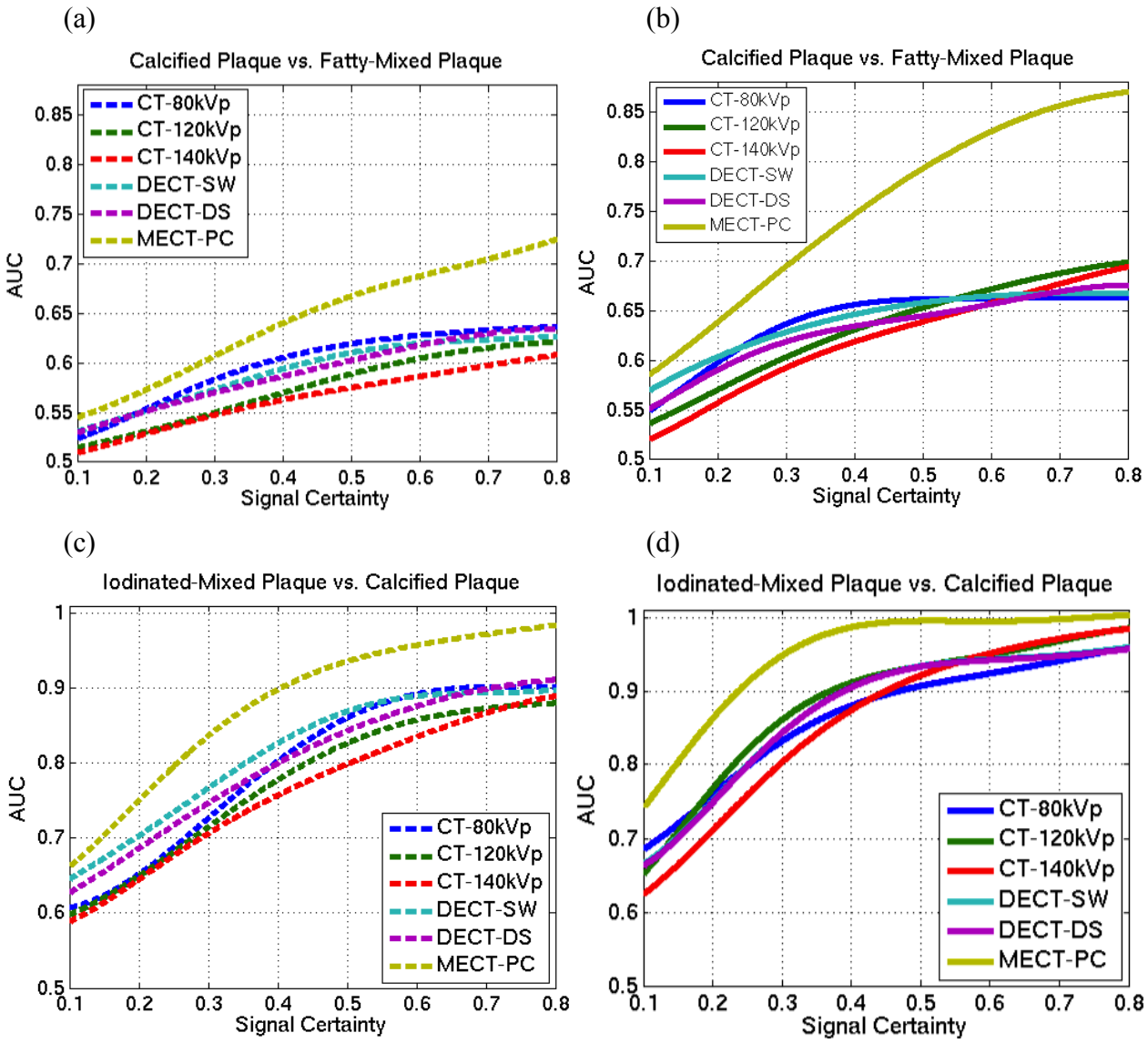

Figure 37 The area under the receiver operating characteristic curve (AUC) as a function of signal certainty for (a,b) the identification task of DT-1 using FBP-Ramp and FBP-Hannning, respectively; and (c,d) the identification task of DT-2 using FBP with Ramp and Hanning, respectively, acquired using the CT-80kVp, CT-120kVp, CT-140kVp, DECT-DS, DECT-SW, and MECT-PC systems. Note that the *dashed lines* referred to using FBP with the Ramp filter and the *solid lines* referred to using FBP with the Hanning filter.

The reconstructed images using the FBP algorithm with Ramp filters have poorer noise performance than those with Hanning filters. Typically, the Ramp-filtered kernel preserves high-frequency contents (i.e., edges) in the projection data while it also enhances image noise, with most noise presenting itself as high-frequency features. Using the FBP algorithm, the choice of the filter kernel represents a trade-off between noise and spatial resolution. The spatial resolution of CT systems can be quantified using the impact of the modulation transfer function (MTF) (defined as the ratio of the output modulation to the input modulation), which is useful for measuring a system response to different frequencies. Typically, a high-resolution reconstruction kernel yields an increased noise level. Hence, for each clinical application, an appropriate choice of the filter kernel is specifically chosen to balance these two factors. For example, the GE LightSpeed CT scanner has six different types of filters: soft, standard, detail, lung, bone, and edge [95], which the bone kernel is often used to examine fine structures but providing noisier images. With an increased inherent spatial resolution, the later scanner Discovery CT750 HD (GE Healthcare; Milwaukee, WI) provides additional five reconstruction kernels to optimize the appearance of stent, calcified plaques, soft plaques, or stenosis for cardiac imaging [95]. Unfortunately, the design details of these filters are commonly considered proprietary and are inaccessible in the public domain.

For the conventional CTs, it is not surprising that CT-80kVp has the highest discrimination performance as compared to CT-120kVp and CT-140kVp. With an increasing tube voltage, the efficiency of the X-ray tube as well as the penetration of the radiation is increased. As a result, there is larger penetration of the radiation and it causes the image contrast to decrease [60]. This can be shown in terms of the attenuation coefficient characteristics illustrated in Figure 31. As shown, the attenuation differences between the higher atomic number (Z) plaque materials (i.e.,

iodine, calcium) and the lower Z plaque material (i.e., mixed fat) become smaller at higher energy levels. The plaque composition with higher Z material, such as iodine (Z = 53, density = 4.93 g/cm^3) or calcium (Z = 20, density = 1.55 g/cm^3), usually attenuates more radiation. Hence, both the elevated density and the calcium/iodine mass contributions lead to a comparably strong X-ray attenuation of calcified/iodinated materials, especially in particular for low energies, yielding high attenuation values. This attenuation is most pronounced for the photoelectric effect owing to these materials' high effective atomic number. By contrast, the composition with lower Z material, such as soft tissue or fat (effective Z = 10, density = 1 g/cm^3), shows a smaller effect and yields low attenuation values due to Compton scattering dominance [29, 30]. At increasing tube voltages, the material discrimination performance decreases according to the material contrast decreases.

Using the DECT systems, even though they have additional characteristic information from the high-kVp sources, they seem to not provide great benefit. The additional high-kVp information is unlikely to significantly enhance the detail of the material characteristics. As can be seen in Figure 35(b,e) and Figure 36(b,e), the CR_F values of the low- and high-kVp are almost similar. This implies the similar characteristics using the low- and high-tube voltages. Through the higher noise of the high-kVp sources, it is because of the contribution of fewer photon counts due to the dose domination setup, as the fraction of the high-kVp source spectrum is quite small (1:19). Hence, the lower-energy spectrum of DECT used almost the same tube current as applying to the single source of the conventional CT systems. As a result, the influence of low-kVp mainly dominates to the signals and the DECT systems show the similar performances to the conventional CT systems, especially CT-80kVp. In addition, increasing the dose fraction for high-kVps does not improved the SNRs, as we have tested in the experiment. Interestingly,

the discrimination SNRs of DECT are sometimes worse than of the single-source CT with 80kVp, as shown in DT-2 using FBP-Hanning in the SKE/BKE framework (see Figure 36). Like the SKE/BKE task, the signal-variation study (SKS/BKE) sometimes shows inconsistency of the discrimination performances among the DECT (-DS, -SW) systems and the conventional CT systems, especially CT-80kVp. These findings are similar to the recent comparison studies showing that dual-energy acquisitions can provide similar or even improved contrast-to-noise ratios at equivalent dose [143, 144]. This indicates that additional material characteristics obtained using DECT may not reliably improve the ability to differentiate various material compositions in plaque imaging.

Furthermore, for DECT, we have investigated and compared discrimination performance between the proposed observer method evaluating on the low- and high-energy images and the conventional CHO observer evaluating on energy-subtracted images (i.e., subtraction of the low- and high-energy images). As expected, we have found that on average of the signal variability, the proposed method provided superior SNR over the conventional CHO evaluating on subtracted images by 589.3% (DT-1) and 747.0% (DT-2) for DECT-SW; and by 249.5% (DT-1) and 223.4% (DT-2) for DECT-DS using FBP-Ramp images. For FBP-Hanning, we found that the discrimination SNRs of the proposed method were better than that of the subtracted images by 500.6% (DT-1) and 535.9% (DT-2) for DECT-SW; and by 186.5% (DT-1) and 156.7% (DT-2) for DECT-DS. The increased percentage of the improvement on DECT-SW is larger than that of DECT-DS because DECT-SW has more overlap between the low- and high-energy spectra than DECT-DS. As a result, the subtracted images of DECT-SW lost more signal than that of DECT-DS. This indicates that it is inappropriate to evaluate the discrimination performance on qualitative subtracted images of DECT. This is because the inferior image

quality of subtracted images regarding reduced signals (photon counts) and increased image noise (variance). Evaluating the low- and high-energy images separately using the proposed observer method can avoid the given issues, which would cause inferior image quality were the subtraction method to be used.

MECT-PC provides substantial differentiation because it makes use of additional specific characteristics obtained from the energy discrimination capability of photon-counting detectors. Unlike the CT systems that are equipped with integrating detectors, photon-counting detectors separate the energy deposits of each individual photon interacting with the detector, thereby providing better classification performance. The conventional CTs and some designs of DECT systems integrate the charge generated by X-ray photon interactions in the detector, so they provide non-specific energy information regarding individual photons. In principle, the overlap of the weighting functions between the narrowly-separated energy bins can be eliminated using an ideal energy-resolving counting detector. Hence, images using photon-counting detectors can reduce relative errors (uncertainty) in material decomposition [35]. As demonstrated in our study, MECT-PC has improved the FOM over other CT systems. Similar to DECT, the low-energy bins of MECT-PC mainly contribute to the SNR. Typically, the material characteristics between the spotty calcification and the iodine contrast agents can be readily separated, as the information obtained in each energy bin shows very different characteristics, especially in energy bin $j = 1$ and $j = 2$ for the identification tasks of DT-1 and DT-2 (see Figure 34(c,f) and Figure 35(c,f)). The large contrast at energy bin $j = 2$ of DT-2 contains the K-edge energy information of iodine (33.2 keV), illustrating the different characteristics of this material. Figure 38 can be used to confirm the specific attenuation characteristics of the plaque features within the ROIs from the five energy bins of MECT-PC. As shown, the energy bin $j = 2$ contains the peak of the iodine

attenuation coefficients. This demonstrates that the proposed numerical observer locally processes the information (i.e., signal, noise) from each energy bin and provides a proper integration of this information across the multiple energy bins.

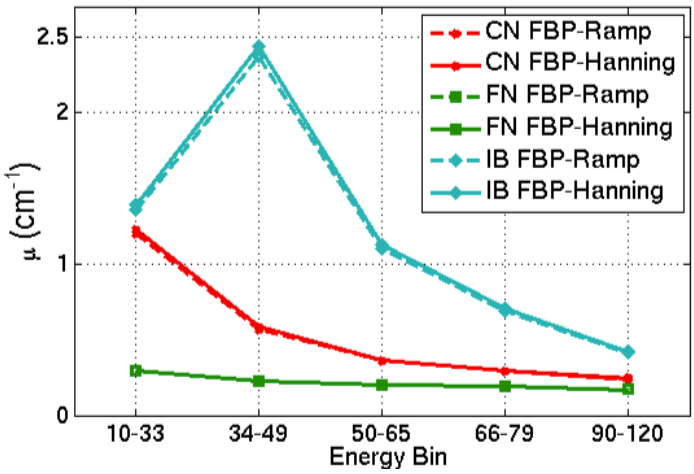

Figure 38 The attenuation coefficients, μ (cm^{-1}), of the features inserted within the vulnerable plaque region: 1) calcified nodule (CN), 2) fatty-mixed nodule (FN), and 3) iodinated blood (IB), reconstructed using filtered back projection (FBP) with Ramp and Hanning filters.

It may be suggested that the proposed numerical observer and the material-discrimination framework can be applied to investigate or compare imaging systems with no limitation on the data dimensionality. The underlying reasons of the advantages of the proposed two-staged design were described in our previous work [132]. For spectral CT imaging, the proposed method can be extended to investigate volumetric 3D or 4D images (i.e., 3D in space and 1D in time), as the channel functions can be modified to support the increased dimensionality.

There is some question as to whether the increasing the number of energy bins of MECT-PC has significant impact on the FOM of the material classification or not. Leng *et al*. has shown that the selection of the number, width, and location of energy bins have influence in material differentiation and noise of spectral CT [35]. There is a tradeoff between energy bin size

(or energy bin number) and image noise. For example, a narrow energy bin has better energy resolution compared to a wider energy bin, and it enables better material differentiation. However, using narrow bins (imply more number of energy bins) allows smaller number of photons available in each energy bin, and therefore the image noise within each bin increases. Multiple energy bins provide more data points available along the attenuation-energy curve, and enable better curve-fitting to promote better material differentiation. In contrast, the increased image noise may make it impossible to detect small differences in material composition. Therefore, the proposed numerical observer can be used to investigate the overall performance of the material differentiation with varying these parameters, as the proposed observer can assess both material specificity and image noise throughout multiple energy bins simultaneously.

We acknowledge as a limitation of this work that several assumptions are made to demonstrate the method as implemented for comparison of all the investigated CT systems. Yet we cannot validate the proposed framework if the experiment is performed on real scanner systems. This is because the possible degradation problems that may occur in the real detector systems might confound our conclusions through device-specific effects. For example, the measurements of photon-counting detectors can deviate from the truth due to numerous factors (e.g. pulse pileup, Compton scattering, K-escape x-rays or charge-sharing effects), which lead to various degradations in both recorded counts and energy spectra. However, several research studies demonstrated and validated their methods on the assumptions of ideal detectors, especially on photon-counting spectral CT [33, 145, 146]. It is suggested that one may apply decreased efficiency to the implementations of detectors and energy resolution to model more realistic systems for further investigation of the photon-counting spectral CT performance, e.g., applying 10% decrease in energy resolution with the quantum detection efficiency varying with

photon energy [33], or using 12% full width at half maximum (FWHM) energy resolution [145]. In our future study, we will validate the performance of MECT in different detector designs with ideal and decreased QDE detectors as well as real acquisition data from a clinical scanner system using the proposed observer method. Furthermore, consistent advances in several strategies and developments have been proposed to improve high-quality MECT photon-counting detector systems [147-157]. Therefore, the proposed numerical observer framework may be a valuable tool to evaluate the achieved performance obtained from the new development methods. On the other hand, this study has shown the performance of an ideal MECT, which can serve an upper bound and may thereby aid real MECT by providing an ideal reference.

7.8 Chapter Summary

In this chapter, the author has demonstrated to applying a novel numerical observer with an image assessment framework for material discrimination tasks using spectral CT images. Our method overcomes the main limitation of the current quantitative metrics for evaluating spectral CT imaging, whose data domain is complex and multidimension. The proposed observer has been designed to have two-step processing: first, accommodating the spatial attenuation information in each energy bin and second, integrating all spatial-attenuation information to finally assess the material characteristics acquired from multiple energy windows of spectral CT. The proposed methods were evaluated using simulated data, in which attenuation coefficient maps were generated using XCAT and fused to the generated plaque features with known elemental compositions. Binary classification tasks, which are based on the standard SKE/BKE task and which mimic clinical scenarios with the variation of signal certainty based on the SKS/BKE task, were performed. The proposed methods showed the improvement of plaque

classification tasks, which were measured by discrimination SNR and AUC figures of merit, using multi-energy CT systems as compared to the different acquisition methods of both dual-energy CT and conventional CT systems at equivalent dose.

Chapter 8

Conclusions and Future Research Directions

8.1 Conclusions of the Research Studies

This dissertation developed the methodological approach to automatically evaluate the performance of the improvement achieved from the new image-acquisition and image-processing techniques with their data in multidimension. The key findings of the dissertation are summarized below:

In Chapter 3, the author developed **a novel numerical observer for multidimensional imaging assessment**. The numerical observer consisted of spatial and additional (i.e., temporal, kinetic parametric, spectral) information that is considered appropriate for an image quality assessment. The proposed numerical observer constructed with a 3D Channelized Hotelling Observer for the spatial domain followed by a Hotelling Observer for the additional domain. With this two-staged design, the proposed observer could be applied to several clinical

applications whose data improved by using developed technologies and that moving toward the use of multidimensional images (e.g., 3D+*t*, 3D+*k*, 3D+*e*).

In Chapter 4, we presented the first validation study investigating the **lesion-detection performance in respiratory–gated PET**. This work presented a novel 4D observer framework and carefully validated it on simulated images. The author used the 4D XCAT phantoms that was modeled based highly detailed human anatomies and human respiratory motion, and was widely accepted as a standard tool to simulate realistic patient studies. The lesion conditions (e.g., sizes, contrasts, positions) were chosen based on typical clinical studies for a detection task of the observer study in lung cancer. The uptake activities, data noise levels, number of events, and geometry of the simulated clinical PET scanner were set following the realistic PET imaging acquisition. Furthermore, the simulation tool with GATE Monte Carlo used in this study is based on a statistical method and widely accepted by researchers for investigation and validation of new analysis/reconstruction methods.

The assessment of signal detection (image quality) in simulated 4D PET imaging demonstrated promising results of the improvement obtained from respiratory-gated PET as compared to the standard methods (i.e., non-gated, and motion-corrected methods). Specifically, this study shows that a numerical observer (3D+*t*) with rigorous objective evaluation that applied directly on all gated frames instead of conventional motion-corrected images demonstrates the existing detection performance achieved from respiratory-gated PET. One of the reasons is that this approach can avoid the effect of inaccuracy of post processing obtained from the motion correction methods. In addition, this methodological approach can be used as an upper bound to investigate the performance of the motion correction method.

In Chapter 5, we examined the performance of **lesion detection in respiratory–gated clinical PET/CT**. This research study has demonstrated that the proposed framework can be generalized in clinical-oriented scenarios. The validation of realistic lesion-detection tasks in clinical gated PET and gated CT data of diseased patients illustrates promising evidence of the use of the proposed method in the complex clinical data. The lesion-detection framework with realistic artificial lesions added into a population of patients is appropriate to specify the lesion properties in the SKE/BKE lesion detection study.

This research study has contributed clinical values to the achievement of the respiratory-gated PET technology. The proposed 4D approach provides a more reliable objective assessment for the impact of respiratory-gated PET, which substantially improves lesion detectability over the standard 3D observer methods (i.e., non-gated and motion-corrected).

In Chapter 6, we presented the validation study of **lesion detection in kinetic parametric PET**. This research study has demonstrated the evaluation of the quantitative analysis of kinetic parameters estimated by mathematical methods, such as a nonlinear least-square algorithm with compartmental model and graphical analysis (i.e., Patlak). Whereas there are very limited studies in objective image-quality assessment of parametric PET using computer observers, this work has demonstrated the impact of the improvement achieved from this quantitative analysis method.

The lesion-detection SNRs evaluated by applying the proposed framework has shown significantly improved image quality in clinical kinetic parametric images over Patlak graphical analysis, dynamic, static PET images, respectively. These outcomes illustrate that the proposed observer framework takes account signal profiles and variability of noise in different uncertainty of different approaches in imaging acquisitions and quantitative analyses.

In Chapter 7, the author has validated the performance of **atherosclerotic plaque classification in Spectral CT**. This research study has confirmed the universal utility of the proposed methodological approach in various types of the imaging domains. This study has presented the validation in classification tasks of different materials in various CT imaging techniques. This work has demonstrated that the proposed numerical observer can be used not only in tomographic emission imaging, but also in radiology imaging. As known, the noise embedded in CT images is mainly dominated by the sources of diagnostic radiation energy (i.e., Compton scattering and Photoelectric effects). Interestingly, this work has shown that the proposed observer takes account on various tasks and conditions of noise. Moreover, this work includes the signal variability framework based on SKS/BKE paradigm for assessing material characterization obtained through the additional energy-dependent attenuation information of spectral CT. These methods can be further extended to other clinical tasks such as kidney or urinary stone identification applications.

8.2 Future Research Directions

This dissertation provides a useful image-quality assessment metric of multidimensional images for new developments widespread in medical imaging community. These research studies can be extended to several further directions described as followings:

First, the proposed methods can be employed for task-based assessment in any applications, making use of **higher dimensional data** with no dimensional limitation. H. H. Barrett *et al*. [8] state that a numerical observer has no dimensional limitation. With benefit of the layered numerical-observer design, one may build a multi-layered numerical observer for supporting higher dimensional data that have more information domains. For example, one might apply a

multi-layered numerical observer to optical imaging in the spatiotemporal format with its spectral data, containing 5D information (3D + time + spectral information), or apply to dynamic magnetic resonance imaging with magnetic resonance spectroscopy (4D MRI + MRS), or multimodality imaging (PET/MR + MRI-T1 + MRI-T2) [158-161].

Second, we can perform the validation of **clinical studies for the spectral CT work**. According to SKE/BKE (or SKS/BKE), the physical and statistical properties of the set of objects to be imaged may be specified, with use of the simulation of material features one can provide the investigator with optimal methods for characterizing the properties of the objects. Adding simulated targets to real images (creating so-called hybrid images) becomes an interesting realistic option for task-based assessment studies [8, 17, 18, 162]. Hence, image fusion between the simulated plaque features and patient's background demonstrated in our framework may be appropriately applied in clinical validation. This simulation work, which is a pilot study for the assessment of spectral CT in plaque imaging, can be applied to other clinical applications, such as coronary artery plaque imaging, differentiation of kidney stones [163], or identification of gouty tophi [164].

Third, we can perform **multi-class material discrimination tasks for spectral CT**. MECT-PC has the ability to decompose more than two materials, as more than one K-edge contrast medium can be simultaneously imaged and distinguished using four or more energy thresholds or windows [68, 165]. In this case, the proposed framework can be extended to support multiclass discrimination tasks or multiple-decision L-class problem with $L > 2$, where the data are to be assigned to one of L possible hypotheses or the underlying classes. Thus, multiple discriminant functions and partitioning rules are required to support multiple material-classification tasks. The observer then makes decision D_i, deciding in favor of

hypothesis H_i [8]. The relevant study performed by He et al. has demonstrated the three-class task performance based on linear discrimination analysis [166].

Forth, the numerical observer can be developed based on **machine learning**. The machine learning approach can be used to train and predict human observer performance. Selected image features and human observer scores can be trained using, for example, the regression model based on nonlinear support vector machine (SVM), or relevance vector machines (RVM) (a modern Bayesian learning methodology). Then, the numerical observer developed based on machine learning can predict human performance for unseen data in the evaluation of new imaging devices or reconstruction methods. Existing studies are presented in [167, 168]. With this concept, it can extend to apply to multidimensional imaging.

Finally, the proposed multi-layered observer can be used for investigating the data with **multivariate distribution** (e.g., Gaussian mixture distributed data). It is suggested to decompose the mixture of one or more multivariate Gaussian distribution components using various analysis methods, such as Gaussian mixture density decomposition (GMDD) [169], expectation-maximization (EM), K-means clustering, factor analysis, or principal component analysis (PCA). Then, we can use the proposed multi-layer numerical observer by applying each CHO of the first layer to each isolated Gaussian distribution component, and then combine all the CHOs with the HO integration. In principle, the CHO and HO models support both Gaussian and non-Gaussian distributed data. If the data are Gaussian distributed, the HO is identical to the ideal observer. If the data are non-Gaussian, HO requires knowledge of only the mean and variance of the data. Therefore, the decomposition of the Gaussian mixtures prior to the CHO/HO computation can provide the maximum SNR values for the multivariate distributed data.

Bibliography

1. Cherry, S.R., J.A. Sorenson, and M.E. Phelps, *Physics in Nuclear Medicine*. 2012: Elsevier Saunders.

2. Eckstein, M.P., C.K. Abbey, and F.O. Bochud, *A Practical Guide to Model Observers for Visual Detection in Synthetic and Natual Noisy Images*, in *Handbook of Medical Imaging*. 2000, Society of Photo-Optical Instrumentation Engineers.

3. Bushberg, J.T., J.A. Seibert, J. Edwin M. Leidholdt, and J.M. Boone, *The Essential Physics of Medical Imaging*. 1994, Maryland, USA: Williams & Wikins.

4. Bunyaviroch, T. and R.E. Coleman, *PET evaluation of lung cancer.* J Nucl Med, 2006. **47**(3): p. 451-69.

5. Abbey, C.K. and H.H. Barrett, *Human- and model-observer performance in ramp-spectrum noise: effects of regularization and object variability.* Journal of the Optical Society of America. A, Optics, image science, and vision, 2001. **18**(3): p. 473-88.

6. Park, S., H.H. Barrett, E. Clarkson, M.A. Kupinski, and K.J. Myers, *Channelized-ideal observer using Laguerre-Gauss channels in detection tasks involving non-Gaussian distributed lumpy backgrounds and a Gaussian signal.* Journal of the Optical Society of America. A, Optics, image science, and vision, 2007. **24**(12): p. B136-50.

7. Gifford, H.C., M.A. King, D.J. de Vries, and E.J. Soares, *Channelized hotelling and human observer correlation for lesion detection in hepatic SPECT imaging.* Journal of nuclear medicine : official publication, Society of Nuclear Medicine, 2000. **41**(3): p. 514-21.

8. Barrett, H.H. and K.J. Myers, *Foundations of Image Science*, ed. B.E.A. Saleh. 2004: Wiley-Interscience. 913-1000.

9. Platisa, L., B. Goossens, E. Vansteenkiste, S. Park, B.D. Gallas, A. Badano, and W. Philips, *Channelized Hotelling observers for the assessment of volumetric imaging data sets.* Journal of the Optical Society of America. A, Optics, image science, and vision, 2011. **28**(6): p. 1145-63.

10. Myers, K.J., H.H. Barrett, M.C. Borgstrom, D.D. Patton, and G.W. Seeley, *Effect of noise correlation on detectability of disk signals in medical imaging.* Journal of the Optical Society of America. A, Optics and image science, 1985. **2**(10): p. 1752-9.

11. Fiete, R.D., H.H. Barrett, W.E. Smith, and K.J. Myers, *Hotelling trace criterion and its correlation with human-observer performance.* Journal of the Optical Society of America. A, Optics and image science, 1987. **4**(5): p. 945-53.

12. Barrett, H.H., J. Yao, J.P. Rolland, and K.J. Myers, *Model observers for assessment of image quality.* Proceedings of the National Academy of Sciences of the United States of America, 1993. **90**(21): p. 9758-65.

13. Rolland, J.P. and H.H. Barrett, *Effect of random background inhomogeneity on observer detection performance.* Journal of the Optical Society of America. A, Optics and image science, 1992. **9**(5): p. 649-58.

14. Barret, H., C. Abbey, B. Gallas, and M. Eckstein, *Stabilized Estimates of Hotelling-Observer Detection Performance in Patient Structured Noise*, in *SPIE*1998. p. 27-43.

15. Zhang, L., *Numerical observers for the objective quality assessment of medical images*, 2012, Université d'Angers.

16. Burgess, A.E., X. Li, and C.K. Abbey, *Visual signal detectability with two noise components: anomalous masking effects.* Journal of the Optical Society of America. A, Optics, image science, and vision, 1997. **14**(9): p. 2420-42.

17. El Fakhri, G., P.A. Santos, R.D. Badawi, C.H. Holdsworth, A.D. Van Den Abbeele, and M.F. Kijewski, *Impact of acquisition geometry, image processing, and patient size on lesion detection in whole-body 18F-FDG PET.* Journal of nuclear medicine : official publication, Society of Nuclear Medicine, 2007. **48**(12): p. 1951-60.

18. El Fakhri, G., S. Surti, C.M. Trott, J. Scheuermann, and J.S. Karp, *Improvement in lesion detection with whole-body oncologic time-of-flight PET.* Journal of nuclear medicine : official publication, Society of Nuclear Medicine, 2011. **52**(3): p. 347-53.

19. Tseng, H.W., J. Fan, M.A. Kupinski, P. Sainath, and J. Hsieh, *Assessing image quality and dose reduction of a new x-ray computed tomography iterative reconstruction algorithm using model observers.* Med Phys, 2014. **41**(7): p. 071910.

20. Sanchez, A.A., E.Y. Sidky, and X. Pan, *Task-based optimization of dedicated breast CT via Hotelling observer metrics.* Med Phys, 2014. **41**(10): p. 101917.

21. Detorie, N. and M. Dahlbom, *Motion Correction for Respiratory Gated PET Images*, in *IEEE Nuclear Science Symposium* 2006. p. 3273-3277.

22. Thielemans, K., R.M. Manjeshwar, X. Tao, and E. Asma, *Lesion detectability in motion compensated image reconstruction of respiratory gated PET/CT*, in *IEEE Nuclear Science Symposium* 2006. p. 3278-3282.

23. Petibon, Y., J. Ouyang, X. Zhu, C. Huang, T.G. Reese, S.Y. Chun, Q. Li, and G. El Fakhri, *Cardiac motion compensation and resolution modeling in simultaneous PET-MR: a cardiac lesion detection study.* Physics in medicine and biology, 2013. **58**(7): p. 2085-102.

24. Ikoma, Y., H. Watabe, M. Shidahara, M. Naganawa, and Y. Kimura, *PET kinetic analysis: error consideration of quantitative analysis in dynamic studies.* Ann Nucl Med, 2008. **22**(1): p. 1-11.

25. Morris, E.D., C.J. Endres, K.C. Schmidt, B.T. Christian, R.F.M. Jr., and R.E. Fisher, *Kinetic Modeling in Positron Emission Tomography*. 2004, Elsevier Inc. p. 499-540.

26. Chen, J. and X. Yu, *Rapid Assessment of Parametric PET Images with Computer Observers*, in *IEEE NSS/MIC*2004. p. 2625-2628.

27. Wang, G. and J. Qi, *Investigation of Lesion Detectability in Dynamic PET Data Sets*, in *IEEE MIC* 2006. p. 1344-1347.

28. Saba, L., G.M. Argiolas, P. Siotto, and M. Piga, *Carotid artery plaque characterization using CT multienergy imaging.* AJNR Am J Neuroradiol, 2013. **34**(4): p. 855-9.

29. Cormode, D.P., E. Roessl, A. Thran, T. Skajaa, R.E. Gordon, J.P. Schlomka, V. Fuster, E.A. Fisher, W.J. Mulder, R. Proksa, and Z.A. Fayad, *Atherosclerotic plaque composition: analysis with multicolor CT and targeted gold nanoparticles.* Radiology, 2010. **256**(3): p. 774-82.

30. Paul, J., M.M. Tan, M. Farhang, M. Beeres, and T.J. Vogl, *Dual-energy CT spectral and energy weighted data sets: carotid stenosis and plaque detection.* Acad Radiol, 2013. **20**(9): p. 1144-51.

31. Zainon, R., J.P. Ronaldson, T. Janmale, N.J. Scott, T.M. Buckenham, A.P. Butler, P.H. Butler, R.M. Doesburg, S.P. Gieseg, J.A. Roake, and N.G. Anderson, *Spectral CT of carotid atherosclerotic plaque: comparison with histology.* Eur Radiol, 2012. **22**(12): p. 2581-8.

32. Alessio, A.M. and L.R. MacDonald, *Quantitative material characterization from multi-energy photon counting CT.* Med Phys, 2013. **40**(3): p. 031108.

33. Baturin, P., Y. Alivov, and S. Molloi, *Spectral CT imaging of vulnerable plaque with two independent biomarkers.* Phys Med Biol, 2012. **57**(13): p. 4117-38.

34. Rigie, D.S. and P.J.L. Riviere, *Task Based Characterization of Spectral CT Performance via the Hotelling Observer*, in *IEEE Nucl. Sci. Symp. & Med. Img. (NSS/ MIC)*2012.

35. Leng, S., L. Yu, J. Wang, J.G. Fletcher, C.A. Mistretta, and C.H. McCollough, *Noise reduction in spectral CT: reducing dose and breaking the trade-off between image noise and energy bin selection.* Med Phys, 2011. **38**(9): p. 4946-57.

36. Sommer, W.H., A. Graser, C.R. Becker, D.A. Clevert, M.F. Reiser, and K. Nikolaou, *Image quality of virtual non-con- trast images derived from dual energy CT angiography after endovascular aneurysm repair.* J Vasc Interv Radiol, 2010. **21**: p. 315-321.

37. Stolzmann, P., T. Frauenfelder, T. Pfammatter, N. Peter, H. Scheffel, and M. Lachat, *Endoleaks after endovascular abdomi- nal aortic aneurysm repair: detection with dual-energy dual- source CT.* Radiology, 2008. **249**(2): p. 682-691.

38. Chandarana, H., M. Godoy, I. Vlahos, A. Graser, J. Babb, and C. Leidecker, *Abdominal aorta: evaluation with dual-source dual-energy multidetector CT after endovascu- lar repair of aneurysms–initial observations.* Radiology, 2008. **2**(249): p. 692-700.

39. Wang, Z., A.C. Bovik, and L. Lu, *Why is image quality assessment so difficult?*, in *2002 IEEE International Conference on Acoustics, Speech, and Signal Processing (ICASSP)*2002: Orlando, FL, USA. p. IV-3313 - IV-3316.

40. Chen, M., J. Bowsher, A. Baydush, K. Gilland, D. DeLong, and R. Jaszczak, *Using the Hotelling observer on multislice and multiview simulated SPECT myocardial images.* IEEE Trans. Nucl. Sci., 2002. **49**: p. 661-667.

41. Qi, W., Y. Yang, X. Niu, and M.A. King, *A quantitative study of motion estimation methods on 4D cardiac gated SPECT reconstruction.* Medical physics, 2012. **39**(8): p. 5182-93.

42. Hernandez-Giron, I., J. Geleijns, A. Calzado, and W.J. Veldkamp, *Automated assessment of low contrast sensitivity for CT systems using a model observer.* Medical physics, 2011. **38 Suppl 1**: p. S25.

43. Sanchez, A.A., E.Y. Sidky, I. Reiser, and X. Pan, *Comparison of human and Hotelling observer performance for a fan-beam CT signal detection task.* Medical physics, 2013. **40**(3): p. 031104.

44. Yu, L., S. Leng, L. Chen, J.M. Kofler, R.E. Carter, and C.H. McCollough, *Prediction of human observer performance in a 2-alternative forced choice low-contrast detection task using channelized Hotelling observer: Impact of radiation dose and reconstruction algorithms.* Medical physics, 2013. **40**(4): p. 041908.

45. Eckstein, M.P. and J.S. Whiting, *Lesion detection in structured noise.* Academic radiology, 1995. **2**(3): p. 249-53.

46. Myers, K.J. and H.H. Barrett, *Addition of a channel mechanism to the ideal-observer model.* Journal of the Optical Society of America. A, Optics and image science, 1987. **4**(12): p. 2447-57.

47. Yao, J. and H. Barret, *Predicting Human Performance by a Channelized Hotelling Observer Model*, in *SPIE Math Methods Med Imaging*1992. p. 161-168.

48. Wilson, H.R. and J.R. Bergen, *A four mechanism model for threshold spatial vision.* Vision research, 1979. **19**(1): p. 19-32.

49. Daly, S., *The Visual Differences Predictor: An Algorithm for the Assessment of Image Fidelity*. Digital Images and Human Vision, ed. W. AB. 1993, Cambridge: Mass: MIT Press.

50. Eckstein, M.P., C.K. Abbey, B. FO, and W. JS, *The Effect of Image Compression in Model and Human Observers*, in *SPIE Image Perception*1999. p. 243-252.

51. Eckstein, M.P., C.K. Abbey, and W. JS, *Human Vs Model Observers in Anatomic Backgrounds*, in *SPIE*1998.

52. Park, S., E. Clarkson, H. Barret, M.A. Kupinski, and K.J. Myers, *Performance of a channelized-ideal observer using Laguerre-Gauss channels for detecting a Gaussian signal at a known location in different lumpy backgrounds*, in *SPIE*2006.

53. Zhou, L., *Low-contrast Lesion Detection in Tomosynthetic Breast Imaging*, in *Electrical and Computer Engineering*2007, Stony Brook University.

54. Bendriem, B. and D.W. Townsend, *The Theory and Practice of 3D PET*. 2010, Dordrecht, Boston, London: Kluwer Academic Publishers.

55. *Cancer Facts and Figures*, 2013, American Cancer Society.

56. De Wever, W., S. Stroobants, J. Coolen, and J.A. Verschakelen, *Integrated PET/CT in the staging of nonsmall cell lung cancer: technical aspects and clinical integration.* Eur Respir J, 2009. **33**(1): p. 201-12.

57. Bar-Shalom, R., N. Yefremov, L. Guralnik, D. Gaitini, A. Frenkel, A. Kuten, H. Altman, Z. Keidar, and O. Israel, *Clinical performance of PET/CT in evaluation of cancer: additional value for diagnostic imaging and patient management.* J Nucl Med, 2003. **44**(8): p. 1200-9.

58. Neal, A.J. and P.J. Hoskin, *Clinical Oncology Basis Principles and Practice*. 2009: CRC Press.

59. Fornaro, J., S. Leschka, D. Hibbeln, A. Butler, N. Anderson, G. Pache, H. Scheffel, S. Wildermuth, H. Alkadhi, and P. Stolzmann, *Dual- and multi-energy CT: approach to functional imaging.* Insights Imaging, 2011. **2**(2): p. 149-159.

60. Buzug, T.M., *Computed Tomography From Photon Statistics to Modern Cone-Beam CT*. 2008, Berlin Heidelberg: Springer-Verlag Berlin Heidelberg.

61. Johnson, T.R.C., C. Fink, and S.O. Schonberg, *Dual Energy CT in Clinical Practice*. Medical Radiology Diagnostic Imaging, ed. A.L. Baert, et al. 2011, Heidelberg Dordrencht London New York: Springer-Verlag Berlin Heidelberg.

62. Jashari, F., P. Ibrahimi, R. Nicoll, G. Bajraktari, P. Wester, and M.Y. Henein, *Coronary and carotid atherosclerosis: similarities and differences.* Atherosclerosis, 2013. **227**(2): p. 193-200.

63. Go, A.S., D. Mozaffarian, V.L. Roger, E.J. Benjamin, J.D. Berry, M.J. Blaha, S. Dai, E.S. Ford, C.S. Fox, S. Franco, H.J. Fullerton, C. Gillespie, S.M. Hailpern, J.A. Heit, V.J. Howard, M.D. Huffman, S.E. Judd, B.M. Kissela, S.J. Kittner, D.T. Lackland, J.H. Lichtman, L.D. Lisabeth, R.H. Mackey, D.J. Magid, G.M. Marcus, A. Marelli, D.B. Matchar, D.K. McGuire, E.R. Mohler, 3rd, C.S. Moy, M.E. Mussolino, R.W. Neumar, G. Nichol, D.K. Pandey, N.P. Paynter, M.J. Reeves, P.D. Sorlie, J. Stein, A. Towfighi, T.N. Turan, S.S. Virani, N.D. Wong, D. Woo, M.B. Turner, C. American Heart Association Statistics, and S. Stroke Statistics, *Heart disease and stroke statistics--2014 update: a report from the American Heart Association.* Circulation, 2014. **129**(3): p. e28-e292.

64. van Werkhoven, J.M., J.D. Schuijf, O. Gaemperli, J.W. Jukema, E. Boersma, W. Wijns, P. Stolzmann, H. Alkadhi, I. Valenta, M.P. Stokkel, L.J. Kroft, A. de Roos, G. Pundziute, A. Scholte, E.E. van der Wall, P.A. Kaufmann, and J.J. Bax, *Prognostic value of multislice computed tomography and gated single-photon emission computed tomography in patients with suspected coronary artery disease.* J Am Coll Cardiol, 2009. **53**(7): p. 623-32.

65. Ibrahimi, P., F. Jashari, R. Nicoll, G. Bajraktari, P. Wester, and M.Y. Henein, *Coronary and carotid atherosclerosis: how useful is the imaging?* Atherosclerosis, 2013. **231**(2): p. 323-33.

66. Wintermark, M., S.S. Jawadi, J.H. Rapp, T. Tihan, E. Tong, D.V. Glidden, S. Abedin, S. Schaeffer, G. Acevedo-Bolton, B. Boudignon, B. Orwoll, X. Pan, and D. Saloner,

High-resolution CT imaging of carotid artery atherosclerotic plaques. AJNR Am J Neuroradiol, 2008. **29**(5): p. 875-82.

67. de Weert, T.T., M. Ouhlous, E. Meijering, P.E. Zondervan, J.M. Hendriks, M.R. van Sambeek, D.W. Dippel, and A. van der Lugt, *In vivo characterization and quantification of atherosclerotic carotid plaque components with multidetector computed tomography and histopathological correlation.* Arterioscler Thromb Vasc Biol, 2006. **26**(10): p. 2366-72.

68. Taguchi, K. and J.S. Iwanczyk, *Vision 20/20: Single photon counting x-ray detectors in medical imaging.* Med Phys, 2013. **40**(10): p. 100901.

69. Cook, G.J., *Artefacts and Normal Variants in Whole-Body PET and PET/CT Imaging*, in *Positron Emission Tomography Basic Sciences*, D.L. Bailey, et al., Editors. 2005.

70. Nehmeh, S.A. and Y.E. Erdi, *Respiratory motion in positron emission tomography/computed tomography: a review.* Seminars in nuclear medicine, 2008. **38**(3): p. 167-76.

71. Goerres, G.W., E. Kamel, B. Seifert, C. Burger, A. Buck, T.F. Hany, and G.K. Von Schulthess, *Accuracy of image coregistration of pulmonary lesions in patients with non-small cell lung cancer using an integrated PET/CT system.* J Nucl Med, 2002. **43**(11): p. 1469-75.

72. Hofmann, M., B. Pichler, B. Scholkopf, and T. Beyer, *Towards quantitative PET/MRI: a review of MR-based attenuation correction techniques.* Eur J Nucl Med Mol Imaging, 2009. **36 Suppl 1**: p. S93-104.

73. Lupi, A., M. Zaroccolo, M. Salgarello, V. Malfatti, and P. Zanco, *The effect of 18F-FDG-PET/CT respiratory gating on detected metabolic activity in lung lesions.* Annals of nuclear medicine, 2009. **23**(2): p. 191-6.

74. Nehmeh, S.A., Y.E. Erdi, C.C. Ling, K.E. Rosenzweig, H. Schoder, S.M. Larson, H.A. Macapinlac, O.D. Squire, and J.L. Humm, *Effect of respiratory gating on quantifying PET images of lung cancer.* Journal of nuclear medicine : official publication, Society of Nuclear Medicine, 2002. **43**(7): p. 876-81.

75. Nehmeh, S.A., Y.E. Erdi, C.C. Ling, K.E. Rosenzweig, O.D. Squire, L.E. Braban, E. Ford, K. Sidhu, G.S. Mageras, S.M. Larson, and J.L. Humm, *Effect of respiratory gating*

on reducing lung motion artifacts in PET imaging of lung cancer. Medical physics, 2002. **29**(3): p. 366-71.

76. Phelps, M.E., *PET: The merging of biology and imaging into molecular imaging.* The Journal of Nuclear Medicine, 2000. **41**: p. 661-681.

77. Woo, S.K., K.M. Kim, G.J. Cheon, K.S. Woo, W.S. Chung, J.H. Kang, T.H. Choi, T.S. Lee, C.W. Choi, and S.M. Lim. *Respiratory gating of microPET and clinical CT studies using list-mode acquisition*. in *IEEE Nuclear Science Symposium and Medical Imaging Conference*. 2006. San Diego, CA.

78. Nehmeh, S.A., Y. Erdi, C.C. Ling, K.E. Rosenzweig, H. Schoder, S.M. Larson, H.A. Macapinlac, O.D. Squire, and J.L. Humm, *Effect of respiratory gating on quantifying PET images of lung cancer.* The Journal of Nuclear Medicine, 2002. **43**: p. 876-881.

79. Boucher, L., S. Rodrigue, R. Lecomte, and F. Benard, *Respiratory gating for 3-dimensional PET of the thorax: feasibility and initial results.* The Journal of Nuclear Medicine, 2004. **45**: p. 214-219.

80. Klein, G.J., R.W. Reutter, and R.H. Huesman, *Four dimensional affine registration models for respiratory-gated PET.* IEEE Trans. Nuc. Sci., 2001. **48**: p. 756-760.

81. Klein, G.J., R.W. Reutter, M.H. Ho, J.H. Reed, and R.H. Huesman, *Real-time system for respiratory-cardiac gating in Positron Emission Tomography.* IEEE Trans. Nuc. Sci., 1998. **45**: p. 2139-2143.

82. Lalush, D.S., M.K. Jatko, and W.P. Segars, *An observer study methodology for evaluating detection of motion abnormalities in gated myocardial perfusion SPECT.* IEEE Trans. Biomed. Engin., 2005. **52**: p. 480-485.

83. Polycarpou, I., C. Tsoumpas, and P.K. Marsden, *Analysis and comparison of two methods for motion correction in PET imaging.* Medical physics, 2012. **39**(10): p. 6474-83.

84. Lamare, F., M.J. Ledesma Carbayo, T. Cresson, G. Kontaxakis, A. Santos, C.C. Le Rest, A.J. Reader, and D. Visvikis, *List-mode-based reconstruction for respiratory motion correction in PET using non-rigid body transformations.* Physics in medicine and biology, 2007. **52**(17): p. 5187-204.

85. Zhuang, H., M. Pourdehnad, E.S. Lambright, A.J. Yamamoto, M. Lanuti, P. Li, P.D. Mozley, M.D. Rossman, S.M. Albelda, and A. Alavi, *Dual time point 18F-FDG PET imaging for differentiating malignant from inflammatory processes.* J Nucl Med, 2001. **42**(9): p. 1412-7.

86. Patlak, C.S. and R.G. Blasberg, *Graphical Evaluation of Blood-to-Brain Transfer Constants from Multiple-T ime Uptake Data. Generalizations.* Journal o/Cerebral Blood Flow and Metabolism, 1985. **5**: p. 584-590

87. Patlak, C.S., R.G. Blasberg, and J.D. Fenstermacher, *Graphical Evaluation of Blood-to-Brain Transfer Constants from Multiple-Time Uptake Data.* Journal of Cerebral Blood Flow and Metabolism 1983. **3**: p. 1-7

88. Krak, N.C., J.J. van der Hoeven, O.S. Hoekstra, J.W. Twisk, E. van der Wall, and A.A. Lammertsma, *Measuring [(18)F]FDG uptake in breast cancer during chemotherapy: comparison of analytical methods.* Eur J Nucl Med Mol Imaging, 2003. **30**(5): p. 674-81.

89. Messa, C., Y. Choi, C.K. Hoh, E.L. Jacobs, J.A. Glaspy, S. Rege, E. Nitzsche, S.C. Huang, M.E. Phelps, and R.A. Hawkins, *Quantification of glucose utilization in liver metastases: parametric imaging of FDG uptake with PET.* J Comput Assist Tomogr, 1992. **16**(5): p. 684-9.

90. Necib, H., C. Garcia, A. Wagner, B. Vanderlinden, P. Emonts, A. Hendlisz, P. Flamen, and I. Buvat, *Detection and characterization of tumor changes in 18F-FDG PET patient monitoring using parametric imaging.* J Nucl Med, 2011. **52**(3): p. 354-61.

91. Karakatsanis, N.A., M.A. Lodge, A.K. Tahari, Y. Zhou, R.L. Wahl, and A. Rahmim, *Dynamic whole-body PET parametric imaging: I. Concept, acquisition protocol optimization and clinical application.* Phys Med Biol, 2013. **58**(20): p. 7391-418.

92. van der Veldt, A.A., N.H. Hendrikse, H.J. Harms, E.F. Comans, P.E. Postmus, E.F. Smit, A.A. Lammertsma, and M. Lubberink, *Quantitative parametric perfusion images using 15O-labeled water and a clinical PET/CT scanner: test-retest variability in lung cancer.* J Nucl Med, 2010. **51**(11): p. 1684-90.

93. Muzi, M., H. Vesselle, J.R. Grierson, D.A. Mankoff, R.A. Schmidt, L. Peterson, J.M. Wells, and K.A. Krohn, *Kinetic analysis of 3'-deoxy-3'-fluorothymidine PET studies: validation studies in patients with lung cancer.* J Nucl Med, 2005. **46**(2): p. 274-82.

94. Heismann, B., B. Schmidt, and T. Flohr, *Spectral Computed Tomography*. 2012, Washington, USA: SPIE.

95. Hsieh, J., *Computed Tomography Principles, Design, Artifacts, and Recent Advances*. 2 ed. 2009, Bellingham, Washington USA: Wiley Inter-Science SPIE PRESS.

96. De Zordo, T., K. von Lutterotti, C. Dejaco, P.F. Soegner, R. Frank, F. Aigner, A.S. Klauser, C. Pechlaner, U.J. Schoepf, W.R. Jaschke, and G.M. Feuchtner, *Comparison of image quality and radiation dose of different pulmonary CTA protocols on a 128-slice CT: high-pitch dual source CT, dual energy CT and conventional spiral CT.* Eur Radiol, 2012. **22**(2): p. 279-86.

97. Rakvongthai, Y., W. Worstell, G. El Fakhri, J. Bian, A. Lorsakul, and J. Ouyang, *Spectral CT Using Multiple Balanced K-Edge Filters.* IEEE Trans Med Imag, 2015. **34**(3): p. 740-747.

98. Boussel, L., P. Coulon, A. Thran, E. Roessl, G. Martens, M. Sigovan, and P. Douek, *Photon counting spectral CT component analysis of coronary artery atherosclerotic plaque samples.* Br J Radiol, 2014. **87**(1040): p. 20130798.

99. Wang, X., A. Zamyatin, and D. Shi, *Dose reduction potential with photon counting computed tomography*, in *SPIE*2012. p. 831349.

100. Gifford, H., M. King, P. Pretorius, and R. Wells, *A comparison of human and model observers in multislice LROC studies.* IEEE Trans. Med. Imag. , 2005. **24**: p. 160-169.

101. Kim, J.S., P. Kinahan, C. Lartizien, C. Comtat, and T. Lewellen, *A comparison of planar versus volumetric numerical observers for detection task performance in whole-body PET imaging.* IEEE Trans. Nucl. Sci., 2004. **51**: p. 34-40.

102. Lee, T.-S., E. Frey, and B. Tsui, *Development of 4D channelized Hotelling observer model for gated myocardial perfusion SPECT.* J Nucl Med, 2012. **53 Suppl 1**: p. S487.

103. T.-S. Lee, E. C. Frey, and B. M. W. Tsui, *4D Mathematical Observer Models for the Task-Based Evaluation of Gated Myocardial Perfusion SPECT Images*, in *2012 IEEE Medical Imaging Conference (MIC)*2012: Anaheim, CA, USA.

104. Lorsakul, A., Q. Li, C. Hoog, Y. Petibon, and G.E. Fakhri, *4D Mathematical model observer for lesion detection on respiratory-gated PET imaging.* J Nucl Med. , 2013: p. 54 (Supplement 2):538.

105. Zhang, Y., B.T. Pham, and M.P. Eckstein, *Evaluation of internal noise methods for Hotelling observer models.* Medical physics, 2007. **34**(8): p. 3312-22.

106. Barrett, H.H., C.K. Abbey, and E. Clarkson, *Objective assessment of image quality. III. ROC metrics, ideal observers, and likelihood-generating functions.* Journal of the Optical Society of America. A, Optics, image science, and vision, 1998. **15**(6): p. 1520-35.

107. Eckstein, M.P., J.S. Whiting, and J.P. Thomas, *Role of knowledge in human visual temporal integration in spatiotemporal noise.* Journal of the Optical Society of America. A, Optics, image science, and vision, 1996. **13**(10): p. 1960-8.

108. Eckstein, M.P., J.S. Whiting, and J.P. Thomas, *Role of knowledge in human visual temporal integration in spatiotemporal noise.* JOSA, 1996. **13**: p. 1960-1968.

109. Xue, P. and D.L. Wilson, *Detection of moving objects in pulsed-x-ray fluoroscopy.* JOSA, 1998. **15**: p. 375-388.

110. Jan, S., G. Santin, D. Strul, S. Staelens, K. Assie, D. Autret, S. Avner, R. Barbier, M. Bardies, P.M. Bloomfield, D. Brasse, V. Breton, P. Bruyndonckx, I. Buvat, A.F. Chatziioannou, Y. Choi, Y.H. Chung, C. Comtat, D. Donnarieix, L. Ferrer, S.J. Glick, C.J. Groiselle, D. Guez, P.F. Honore, S. Kerhoas-Cavata, A.S. Kirov, V. Kohli, M. Koole, M. Krieguer, D.J. van der Laan, F. Lamare, G. Largeron, C. Lartizien, D. Lazaro, M.C. Maas, L. Maigne, F. Mayet, F. Melot, C. Merheb, E. Pennacchio, J. Perez, U. Pietrzyk, F.R. Rannou, M. Rey, D.R. Schaart, C.R. Schmidtlein, L. Simon, T.Y. Song, J.M. Vieira, D. Visvikis, R. Van de Walle, E. Wieers, and C. Morel, *GATE: a simulation toolkit for PET and SPECT.* Physics in medicine and biology, 2004. **49**(19): p. 4543-61.

111. Segars, W.P., G. Sturgeon, S. Mendonca, J. Grimes, and B.M. Tsui, *4D XCAT phantom for multimodality imaging research.* Medical physics, 2010. **37**(9): p. 4902-15.

112. Møller, J. and F.P. Schoenberg, *Thinning spatial point processes into Poisson processes.* Adv. in Appl. Probab, 2010. **42**(2): p. 347-358.

113. Streit, R.L., *Poisson Point Processes*. 2010: Springer Science+Business Media, LLC.

114. Wagner, R.F., H.-P. Chan, B. Sahiner, N. Petrick, and J.T. Mossoba, *Finite-sample effects and resampling plans: Applications to linear classifiers and computere-aided diagnosis*, in *SPIE* 1997. p. 467-477.

115. Morey, A.M. and D.J. Kadrmas, *Effect of varying number of OSEM subsets on PET lesion detectability.* J Nucl Med Technol, 2013. **41**(4): p. 268-73.

116. Dikaios, N. and T.D. Fryer, *Acceleration of motion-compensated PET reconstruction: ordered subsets-gates EM algorithms and a priori reference gate information.* Phys Med Biol, 2011. **56**(6): p. 1695-715.

117. Thielemans, K., R.M. Manjeshwar, X. Tao, and E. Asma. *Lesion detectability in motion compensated image reconstruction of respiratory gated PET/CT*. in *IEEE Nucl. Sci. Symp. Conf.* . 2006.

118. Dikaios, N. and T.D. Fryer, *Improved motion-compensated image reconstruction for PET using sensitivity correction per respiratory gate and an approximate tube-of-response backprojector.* Med Phys, 2011. **38**(9): p. 4958-70.

119. Barrett, H.H., D.W. Wilson, and B.M. Tsui, *Noise properties of the EM algorithm: I. Theory.* Phys Med Biol, 1994. **39**(5): p. 833-46.

120. Wilson, D.W., B.M. Tsui, and H.H. Barrett, *Noise properties of the EM algorithm: II. Monte Carlo simulations.* Phys Med Biol, 1994. **39**(5): p. 847-71.

121. Klein, G.J., B.W. Reutter, M.H. Ho, J.H. Reed, and R.H. Huesman, *Real-Time System for Respiratory-Cardiac Gating in Positron Tomography.* IEEE Trans. Nucl. Sci., 1998. **45**(4): p. 2139-2143.

122. Ouyang, J., Q. Li, and G. El Fakhri, *Magnetic resonance-based motion correction for positron emission tomography imaging.* Seminars in nuclear medicine, 2013. **43**(1): p. 60-7.

123. Qiao, F., T. Pan, J.W. Clark, Jr., and O.R. Mawlawi, *A motion-incorporated reconstruction method for gated PET studies.* Phys Med Biol, 2006. **51**(15): p. 3769-83.

124. LaCroix, K.J., B.M.W. Tsui, and E.C. Frey, *Rotationally Symmetric vs. Oriented Frequency Channels for the Hotelling Observer: A Comparison with Human Observers*, in *Nuclear Science Symposium*2000, IEEE: Seattle, WA. p. 1402-1406.

125. Wollenweber, S.D., B. M. W. Tsui, D.S. Lalush, E. C. Frey, K.J. LaCroix, and G.T. Gullberg, *Comparison of Radially-Symmetric Versus Oriented Channel Models Using Channelized Hotelling Observers for Myocardial Defect Detection in Parallel-Hole SPECT*, in *Nuclear Science Symposium*1999, IEEE: Toronto, Ont. p. 2090 - 2094.

126. Goossens, B., L. Platisa, E. Vansteenkiste, and W. Philips, *The Use of Steerable Channels for Detecting Asymmetrical Signals with Random Orientations*, in *Medical Imaging: Image Perception, Observer Performance, and Technology Assessment*2010, SPIE. p. 1-11.

127. Lalush, D.S., M.K. Jatko, and W.P. Segars, *An Observer Study Methodology for Evaluating Detection of Motion Abnormalities in Gated Myocardial Perfusion SPECT.* IEEE Trans. Biomed. Eng., 2005. **52**(3): p. 480-485.

128. Dhawan, V., J.R. Moeller, S.C. Strother, A.C. Evans, and D.A. Rottenberg, *Effect of selecting a fixed dephosphorylation rate on the estimation of rate constants and rCMRGlu from dynamic [18F] fluorodeoxyglucose/PET data.* J Nucl Med, 1989. **30**(9): p. 1483-8.

129. Phelps, M.E., S.C. Huang, E.J. Hoffman, C. Selin, L. Sokoloff, and D.E. Kuhl, *Tomographic measurement of local cerebral glucose metabolic rate in humans with (F-18)2-fluoro-2-deoxy-D-glucose: validation of method.* Ann Neurol, 1979. **6**(5): p. 371-88.

130. Iida, H., I. Kanno, A. Takahashi, S. Miura, M. Murakami, K. Takahashi, Y. Ono, F. Shishido, A. Inugami, N. Tomura, and et al., *Measurement of absolute myocardial blood flow with H215O and dynamic positron-emission tomography. Strategy for quantification in relation to the partial-volume effect.* Circulation, 1988. **78**(1): p. 104-15.

131. Choi, Y., S. Huang, R. Hawkins, J. Kim, and C. Hoh, *Quantification of myocardial blood flow using 13N-ammonia and PET: comparison of tracer models.* J. Nucl Med, 1999. **40**(6): p. 1045-1055.

132. Lorsakul, A., Q. Li, C.M. Trott, C. Hoog, Y. Petibon, J. Ouyang, A.F. Laine, and G. El Fakhri, *4D numerical observer for lesion detection in respiratory-gated PET.* Med Phys, 2014. **41**(10): p. 102504.

133. Lorsakul, A., G.E. Fakhri, N. Guo, R.-F. Yen, M. Normandin, N. Alpert, A. Laine, and Q. Li, *A numerical observer for task-based assessment on kinetic parametric imaging.* J Nucl Med. , 2014: p. 55 (Supplement 1):48.

134. Ribeiro, R.A., J.A.d.S. Ribeiro, O.A.R. Filho, A.G. Caetano, and V.P.S. Fazan, *Common Carotid Artery Bifurcation Levels Related to Clinical Relevant Anatomical Landmarks.* Int. J. Morphol., 2006. **24**(3): p. 413-416.

135. Heismann, B. and M. Balda, *Quantitative image-based spectral reconstruction for computed tomography.* Med Phys, 2009. **36**(10): p. 4471-85.

136. Yang, M., *Dual Energy Computed Tomography for Proton Therapy Treatment Planning*, 2011, The University of Texas: Health Science.

137. Hubbell, J.H. and S.M. Seltzer. *Tables of x-ray mass attenuation coefficients and mass energy-absorption coefficients*. Available from: http://physics.nist.gov/PhysRefData/XrayMassCoef/cover.html.

138. O'Connor, Y.Z. and J.A. Fessler, *Fourier-based forward and back-projectors in iterative fan-beam tomographic image reconstruction.* IEEE Trans. Med. Imag., 2006. **25**(5): p. 582-589.

139. Siewerdsen, J.H., A.M. Waese, D.J. Moseley, S. Richard, and D.A. Jaffray, *Spektr: A computational tool for x-ray spectral analysis and imaging system optimization.* Med. Phys., 2004. **31**(11): p. 3057-3067.

140. Shikhaliev, P.M. and S.G. Fritz, *Photon counting spectral CT versus conventional CT: comparative evaluation for breast imaging application.* Phys Med Biol, 2011. **56**(7): p. 1905-30.

141. Primak, A.N., J.C. Giraldo, C.D. Eusemann, B. Schmidt, B. Kantor, J.G. Fletcher, and C.H. McCollough, *Dual-source dual-energy CT with additional tin filtration: Dose and image quality evaluation in phantoms and in vivo.* Am. J. Roentgenol, 2010. **195**(5): p. 1164-1174.

142. Boll, D.T., M.H. Hoffmann, N. Huber, A.S. Bossert, A.J. Aschoff, and T.R. Fleiter, *Spectral coronary multidetector computed tomography angiography: dual benefit by facilitating plaque characterization and enhancing lumen depiction.* J Comput Assist Tomogr, 2006. **30**(5): p. 804-11.

143. Schenzle J., C., H. Sommer W., and K. Neumaier, *Dual energy CT of the chest: how about the dose?* Invest Radiol, 2010. **45**: p. 347–353.

144. Li, B., G. Yadava, and J. Hsieh, *Head and body CTDIw of dual energy x-ray CT with fast-kVp switching*, in *SPIE Medical Imaging*2010, SPIE: San Diego, CA. p. 7622–7669.

145. Alivov, Y., P. Baturin, H.Q. Le, J. Ducote, and S. Molloi, *Optimization of K-edge imaging for vulnerable plaques using gold nanoparticles and energy resolved photon counting detectors: a simulation study.* Phys Med Biol, 2014. **59**(1): p. 135-52.

146. Schmidt, T.G., K.C. Zimmerman, and E.Y. Sidky, *The effects of extending the spectral information acquired by a photon-counting detector for spectral CT.* Phys Med Biol, 2015. **60**(4): p. 1583-600.

147. Hsieh, S.S. and N.J. Pelc, *The feasibility of a piecewise-linear dynamic bowtie filter.* Med Phys, 2013. **40**(3): p. 031910.

148. Roessl, E. and R. Proksa, *Dynamic beam-shaper for high flux photon-counting computed tomography*, in *Workshop on Medical Applications of Spectroscopic X-ray Detectors*2013: Geneva, Switzerland.

149. Miyajima, S., K. Imagawa, and M. Matsumoto, *CdZnTe detector in diagnostic x-ray spectroscopy.* Med Phys, 2002. **29**(7): p. 1421-9.

150. Kappler, S., S. Hoelzer, E. Kraft, K. Stierstorfer, and T.G. Flohr, *Quantum-counting CT in the regime of count-rate paralysis: Introduction of the pile-up trigger method*, in *SPIE*2011. p. 79610T.

151. Kraft, E., F. Glasser, S. Kappler, D. Niederloehner, and P. Villard, *Experimental evaluation of the pile-up trigger method in a revised quantum counting CT detector*, in *SPIE*2011. p. 83134A.

152. Cammin, J., J.S. Iwanczyk, and K. Taguchi, *Spectral/photon-counting computed tomography*, in *Emering Imaging Technologies in Medicine*, M.A. Anastasio and P.J.L. Riviere, Editors. 2012, Taylor & Francis: London.

153. Cammin, J., J. Xu, W.C. Barber, J.S. Iwanczyk, N.E. Hartsough, and K. Taguchi, *A cascaded model of spectral distortions due to spectral response effects and pulse pileup effects in a photon-counting x-ray detector for CT.* Med Phys, 2014. **41**(4): p. 041905.

154. Ohnesorge, B., T. Flohr, K. Schwarz, J.P. Heiken, and K.T. Bae, *Efficient correction for CT image artifacts caused by objects extending outside the scan field of view.* Med Phys, 2000. **27**(1): p. 39-46.

155. Zamyatin, A.A. and S. Nakanishi, *Extension of the reconstruction field of view and truncation correction using sinogram decomposition.* Med Phys, 2007. **34**(5): p. 1593-604.

156. Hsieh, J., E. Chao, J. Thibault, B. Grekowicz, A. Horst, S. McOlash, and T.J. Myers, *A novel reconstruction algorithm to extend the CT scan field-of-view.* Med Phys, 2004. **31**(9): p. 2385-91.

157. Xu, J., K. Taguchi, and B.M. Tsui, *Statistical projection completion in X-ray CT using consistency conditions.* IEEE Trans Med Imaging, 2010. **29**(8): p. 1528-40.

158. Clarkson, E., M.A. Kupinski, H.H. Barrett, and L. Furenlid, *A Task-Based Approach to Adaptive and Multimodality Imaging: Computation techniques are proposed for figures-of-merit to establish feasibility and optimize use of multiple imaging systems for disease diagnosis and treatment-monitoring.* Proc IEEE Inst Electr Electron Eng, 2008. **96**(3): p. 500-511.

159. Jiang, Y., D. Huo, and D.L. Wilson, *Methods for quantitative image quality evaluation of MRI parallel reconstructions: detection and perceptual difference model.* Magn Reson Imaging, 2007. **25**(5): p. 712-21.

160. Tisdall, M.D. and M.S. Atkins, *Using Human and Model Performance to Compare*

MRI Reconstructions. IEEE Trans Med Imaging, 2006. **25**(11): p. 1510-17.

161. Luong, H., B. Goossens, J. Aelterman, L. Platisa, and W. Philips, *Optimizing image quality in MRI: On the evaluation of k-space trajectories for under-sampled MR acquisition* in *Quality of Multimedia Experience (QoMEX), 2012 Fourth International Workshop on* 2012, IEEE: Yarra Valley, VIC p. 25-26.

162. Schaefferkoetter, J., M. Casey, D. Townsend, and G. El Fakhri, *Clinical impact of time-of-flight and point response modeling in PET reconstructions: a lesion detection study.* Phys Med Biol, 2013. **58**(5): p. 1465-78.

163. Graser, A., R. Johnson T., and M. Bader, *Dual energy CT characterization of urinary calculi: initial in vitro and clini- cal experience.* Invest Radiol, 2008. **43**: p. 112-119.

164. Johnson T., R., S. Weckbach, H. Kellner, F. Reiser M., and R. Becker C., *Clinical image: dual-energy computed tomographic molecular imaging of gout.* Arthritis Rheum, 2007. **56**: p. 2809.

165. Kim, K., J.C. Ye, W. Worstell, J. Ouyang, Y. Rakvongthai, G.E. Fakhri, and Q. Li, *Sparse-View Spectral CT Reconstruction Using Spectral Patch-Based Low-Rank Penalty.* IEEE Trans. Med. Imag., 2015. **34**(3): p. 748-760.

166. He, X. and E.C. Frey, *The validity of three-class Hotelling trace (3-HT) in describing three-class task performance: comparison of three-class volume under ROC surface (VUS) and 3-HT.* IEEE Trans Med Imaging, 2009. **28**(2): p. 185-93.

167. Marin, T., M. Kalayeh, F. Parages, and J. Brankov, *Numerical surrogates for human observers in myocardial motion evaluation from SPECT images.* IEEE Trans Med Imaging, 2013.

168. Brankov, J.G., Y. Yang, L. Wei, I. El Naqa, and M.N. Wernick, *Learning a channelized observer for image quality assessment.* IEEE Trans Med Imaging, 2009. **28**(7): p. 991-9.

169. Zhuang, X., Y. Huang, K. Palaniappan, and Y. Zhao, *Gaussian mixture density modeling, decomposition, and applications.* IEEE Trans Image Process, 1996. **5**(9): p. 1293-302.